Karlsruhe Institute of Technology

Alexander Münchinger

Liquid-Crystal-Elastomer Laser-Microprinted 3D Optomechanical Metamaterials

2022

Dissertation

Liquid-Crystal-Elastomer Laser-Microprinted 3D Optomechanical Metamaterials

Zur Erlangung des akademischen Grades eines
DOKTORS DER NATURWISSENSCHAFTEN (Dr. rer. nat.)
von der KIT-Fakultät der Physik des
Karlsruher Instituts für Technologie (KIT)

genehmigte

DISSERTATION

von

MSc. Alexander Münchinger
geboren in Mühlacker

Tag der mündlichen Prüfung: 02.12.2022
Referent: Prof. Dr. Martin Wegener
Korreferentin: Jun.-Prof. Dr. Eva Blasco

Table of Contents

Publications

Parts of this thesis have already been published …

… in scientific journals:

- A. Münchinger, V. Hahn, D. Beutel, S. Woska, J. Monti, C. Rockstuhl, E. Blasco, and M. Wegener, „ Multi-Photon 4D Printing of Complex Liquid Crystalline Microstructures by In Situ Alignment Using Electric Fields", Advanced Materials Technologies **7**, 2100944 (2021)
- A. Münchinger, L.-Y. Hsu, F. Fürniß, E. Blasco, and M. Wegener, „3D Optomechanical Metamaterials", Materials Today, https://doi.org/10.1016/j.mattod.2022.08.020 (2022)

… at scientific conferences (only own presentations):

- A. Münchinger, V. Hahn, D. Beutel, S. Woska, J. Monti, C. Rockstuhl, E. Blasco, and M. Wegener, "3D two-photon printing of hetero-microstructures by in-situ alignment of liquid-crystal elastomers", SPIE Photonics West (online), March 5, 2021
- A. Münchinger, L.-Y. Hsu, F. Fürniß, E. Blasco, and M. Wegener, "3D Optomechanical Metamaterials - Tuning the Effective Parameters of 3D Elastic Metamaterials by Light", Metamaterials (Siena, Italy), Sep. 14, 2022

Additional related work has already been published in scientific journals:

- L. Yang, A. Münchinger, M. Kadic, V. Hahn, F. Mayer, E. Blasco, C. Barner-Kowollik, and M. Wegener, „On the Schwarzschild Effect in 3D Two-Photon Laser Lithography“, Advanced Optical Materials **7**, 1901040 (2019)
- C. A. Spiegel, M. Hippler, A. Münchinger, M. Bastmeyer, C. Barner-Kowollik, M. Wegener, and E. Blasco, „4D Printing at the Microscale“, Advanced Functional Materials **30**, 1907615 (2019)
- J. Reinbold, T. Frenzel, A. Münchinger, and M. Wegener, „The Rise of (Chiral) 3D Mechanical Metamaterials“, Materials **12**, 3527 (2019)
- S. Woska, A. Münchinger, D. Beutel, E. Blasco, J. Hessenauer, O. Karayel, P. Rietz, S. Pfleging, R. Oberle, C. Rockstuhl, M. Wegener, and H. Kalt, „Tunable photonic devices by 3D laser printing of liquid crystal elastomers“, Optical Materials Express **10**, 2928-2943 (2020)
- J. Monti, A. Concellón, R. Dong, M. Simmler, A. Münchinger, C. Huck, P. Tegeder, H. Nirschl, M. Wegener, C. O. Osuji, and E. Blasco, “Two-Photon Laser Microprinting of Highly Ordered Nanoporous Materials Based on Hexagonal Columnar Liquid Crystals”, ACS Applieed Materials & Interfaces **14**, 33746-33755 (2022)
- L.-Y. Hsu, P. Mainik, A. Münchinger, S. Lindenthal, T. Spratte, A. Welle, J. Zaumseil, C. Selhuber-Unkel, M. Wegener, and E. Blasco, „ A Facile Approach for 4D Microprinting of Multi-photoresponsive Actuators”, Advanced Materials Technologies, 2200801 (2022)

1 Chapter 1
Introduction

Metamaterials are rationally designed structures often made of periodic building blocks. Ideally, such a metamaterial can be interpreted as a continuum with effective properties. This approach is along the lines of established continuum theories mapping effective properties to matter made from atoms. In metamaterials, the effective properties go qualitatively or quantitatively beyond those of the constituent materials since the effective properties arise from the structure and not from the constituent material [1].

The field of metamaterials started with electro-magnetic metamaterials showing a tailored response to electromagnetic radiation including materials that show negative refractive index as probably one of the most famous examples [2–5]. From that point on, the field quickly evolved to many disciplines including mechanical metamaterials that allow a tailored response to mechanical stimuli [1, 6]. Famous examples are auxetics that contract laterally upon a compression [7–13]. Interpreted as a continuous material, such metamaterials are said to have an effective negative Poisson's ratio. Another example are chiral metamaterials that have properties not included in classical elasticity [14], like a twisting motion upon compression [14, 15] or circular phonon eigenmodes that lead to the phenomenon of acoustical activity [16, 17].

Advances in the field of metamaterials allow to tailor metamaterials with desired properties, but once fabricated the material properties are fixed. However, sometimes it is favourable that a material changes its properties in response to an external stimulus. Nature shows us the way. For example, some plants like the Leguminosae contain cells that contract on irradiation with light and thereby move the leaves of the plant towards the sun. This allows the plant to cope with the constantly changing direction of the sunlight. [18] But also, a lot of responsive materials were discovered that can be employed for technical applications. Already in use in daily life are piezoelectric materials that

contract or expand in response to an electric field and are employed in actuators, transducers or oscillators [19]. Shape memory alloys alter their shape in response to a temperature change and are used as actuators in cars, in the wings of aircrafts, in stents, and for many more applications [20]. Another important example are liquid crystals, which consist of molecules with a long-range orientational order along a common direction called the director. This long-rang order causes the liquid crystals to be birefringent with the optic axis along the director. The orientation of the director can be manipulated via electric fields, which is widely used in displays [21].

There are also responsive materials that are currently in discussion for a lot of possible applications. Liquid-crystal elastomers [22–25] for example respond to heat or light with a large anisotropic shape change. Envisioned applications include for example actuators or microrobots [26]. Hydrogels like pNIPAAM show a large isotropic expansion in aqueous conditions for different stimuli like temperature, pH or solvents [25]. Applications are suggested for example in the biomedical area [27]. This is only a small selection and there are many more responsive materials [28, 29].

Most of the examples listed so far react with a shape transformation exposed to an external stimulus. Exploiting shape transformations, responsive metamaterials [1, 30, 31] offer a route to create materials with all kind of tuneable effective properties, since the effective properties of metamaterials arise from their structure.

Concerning responsive mechanical metamaterials there are many published examples including structures tuning stiffness [32–36], Poisson's ratio [37–41], stopbands [42–44] and shape [45, 46] using temperature [35, 39–41, 45, 46], pressure [34], electrical voltage[33, 44], static magnetic fields[32, 36–38, 42] or light[43] as a stimulus. However, all the presented examples are limited to macroscopic models [32–44, 46], 2D structures [37–42, 44, 46] or have a limited parameter tuning range [45].

In this thesis, I present an approach to design and fabricate 3D optomechanical metamaterials with feature sizes in the micrometre regime. Similar to the above example of the light induced reorientation of plants, the presented 3D metamaterials change their shape upon illumination and thereby change their effective mechanical properties. I illustrate the approach on the basis of two different metamaterials. The first metamaterial shows a tuneable effective Poisson's ratio, while the second one is a chiral metamaterial with a tuneable twist per strain. For both structures the respective effective properties can be tuned on a large scale and even be flipped in sign in response to the light of the external LED.

Both responsive metamaterials presented in this thesis are manufactured from liquid-crystal elastomers via a novel 3D laser microprinting technique I established as a part of this thesis. In contrast to other techniques [47–73] it allows for structures from liquid-crystal elastomers with feature sizes in the micrometre regime with sample sizes in the millimetre regime at the same time. The director can be freely adjusted in three dimensions at any point during manufacturing. This is a key requirement for complex 3D responsive metamaterials and is not achieved to this extent by other techniques published so far.

Outline of this Thesis

The fundamentals necessary to understand the thesis are summarized in chapter 2. First, I introduce the fundamentals concerning liquid crystals and liquid-crystal elastomers, since the printed optomechanical metamaterials are made from liquid-crystal elastomers and the employed photoresins are liquid crystals. During the 3D laser microprinting process, a laser has to be focused into the liquid-crystal resin, which is birefringent. Therefore, I introduce the concepts of birefringence and explain how to calculate the shape of a laser that is focused into such a birefringent resin. The chapter is closed with an introduction to continuum mechanics. The equations of continuum mechanics are used within this thesis to predict the effective properties of the two presented 3D optomechanical metamaterials.

In chapter 3, I present the novel 3D laser microprinting technique that I established to print the presented 3D optomechanical metamaterials. The three major challenges I had to solve are described. First, I explain how to control the director orientation within the liquid-crystal resin. This is done via strong quasi-static electric fields induced by a set of electrodes developed by myself. I describe the working principle of the electrodes, how to fabricate them and how they are used. The second challenge that is discussed concerns the focusing of the laser used for the printing. I present solutions how to achieve a tightly focused laser beam for different orientations of director within the liquid-crystal resin. The last challenge I describe is the composition of the liquid-crystal resin itself. I describe the composition of the two resins employed in this thesis and characterize the resulting liquid-crystal elastomer with regard to its thermal expansion. In the end of the chapter, I present printed structures proofing that the technique produces defined 3D structures from liquid-crystal elastomer with spatial control over the director orientation.

In chapter 4, I present two examples for 3D optomechanical metamaterials printed from liquid-crystal elastomer. In the beginning of the chapter, I provide details on the

fabrication process of the metamaterials. This is followed by a description of the setup used to characterized the metamaterials. Moreover, I present the model employed for the finite element calculations that I used to predict the effective properties of the metamaterials. Finally, I present the results of the experimental characterisation of the metamaterials and compare the experimental data to the results of the finite element calculations. In detail I show that the effective Poisson's ratio of the first metamaterial and the twist per strain of the second metamaterial can be tuned on a large range and that even the sign of the effective properties can be flipped.

In chapter 5, I summarize this thesis and set the results into the context of the literature. In the end I give an outlook on future developments.

2 Chapter 2
Fundamentals

In this chapter, I provide the fundamentals that are necessary to understand the 3D laser microprinting of liquid-crystal elastomers. First of all, I give a brief introduction to the basic concepts of liquid crystals and liquid-crystal elastomers. This is followed by an introduction to birefringence and the focussing of laser light into a liquid-crystal resin. In the end of this chapter, I give a short introduction to the equations of continuum mechanics, which I used to predict the effective properties of the 3D optomechanical metamaterials discussed in this thesis.

2.1 Liquid Crystals

A basic understanding about the physics of liquid crystals is necessary to understand the challenges in 3D laser microprinting of liquid-crystal elastomers and how to solve them. The following information is taken from [74–76].

The term liquid crystal denotes a state of matter. There are many different classes of liquid crystals but in this thesis, I will only deal with so called nematic liquid crystals. Nematic liquid crystals are formed of rod-shaped molecules pointing in a direction $\vec{n}'$. An example is 4-Cyano-4'-pentylbiphenyl also called 5CB, which is depicted in Figure 1*a*. The position of the rod-shaped molecules is random like in a liquid, however, the molecules tend to align in a common direction on a long range as depicted in Figure 1*b*. This common direction is called the director $\vec{n}$. Usually, the orientation $\vec{n}'$ of a liquid-crystal molecule is equally probable as its opposite orientation $-\vec{n}'$. This implies that the director $\vec{n}$ is equivalent to $-\vec{n}$.

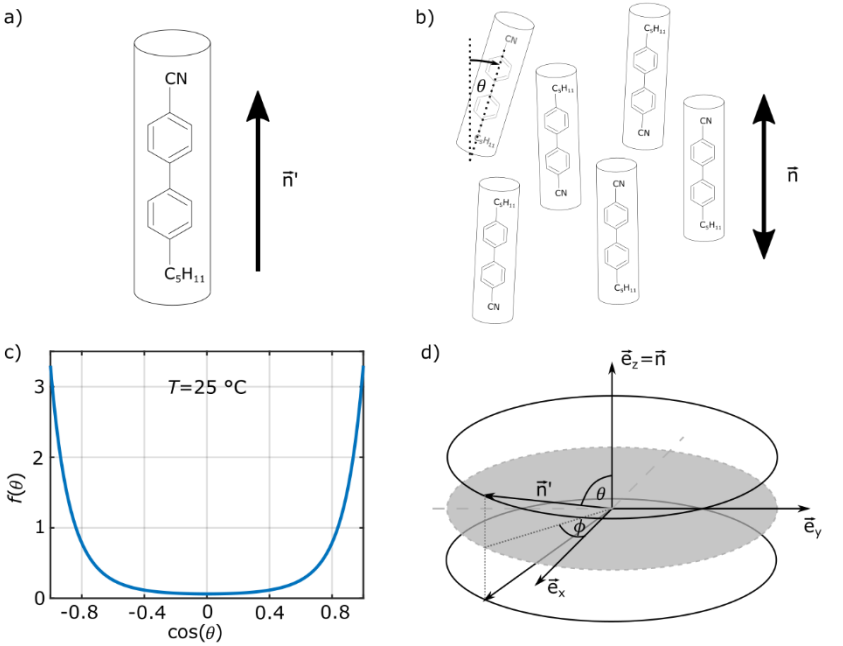

Figure 1. (a) 4-Cyano-4'-pentylbiphenyl (5CB) is an example for a rigid rod-shaped molecule that shows a nematic phase. The orientation of the molecule is denoted with the vector $\vec{n}'$. (b) In the nematic phase, the molecules align along a common direction, the director $\vec{n}$. The angle between the director and the molecule is denoted by θ. (c) $f(\theta)$ describes the probability of a certain orientation of a molecule within the nematic phase at room temperature. (d) According to experimental observations all orientations on the two black circles are equally probable for a given θ.

the director. In total, this means that all orientations on the black circles in Figure 1*d* are equally probable. The probability only depends on the polar angle θ and is described by the distribution function $f(\theta)$. Figure 1*c* shows the distribution function of 5CB at room temperature. It shows, that the probability is highest for an orientation parallel to the director and lowest for an orientation perpendicular to the director.

An important physical quantity to summarize the degree of orientational order is called the order parameter. An order parameter is usually defined such, that it is zero for no orientational order and reaches in some sense a maximum for perfect order. An intuitive approach to construct such an order parameter is to average over the orientations

of the single molecules. However, since an orientation $\vec{n}'$ is equally probable than $-\vec{n}'$, the average

$$\langle \vec{n}' \rangle = \int \vec{n}' f(\theta) \mathrm{d}\Omega = 0 \tag{1}$$

vanishes. A solution to this problem is the definition of a second order tensor $\boldsymbol{Q}$ that serves as an order parameter for a nematic liquid crystal. An easy to interpret definition is given by

$$Q_{ab} = \frac{1}{2}(3\langle n'_a n'_b \rangle - \delta_{ab}) \tag{2}$$

with

$$\langle n'_a n'_b \rangle = \int n'_a n'_b f(\theta) \mathrm{d}\Omega. \tag{3}$$

To interpret the meaning of the second order tensor $\boldsymbol{Q}$, a coordinate system must be chosen, where $\vec{e}_z$ coincides with the director $\vec{n}$. The second order tensor $\boldsymbol{Q}$ then becomes

$$\boldsymbol{Q} = S \begin{pmatrix} -\frac{1}{2} & 0 & 0 \\ 0 & -\frac{1}{2} & 0 \\ 0 & 0 & 1 \end{pmatrix} \tag{4}$$

with

$$S = \frac{1}{2}(3\langle n'_3 n'_3 \rangle - 1). \tag{5}$$

The coefficient S is called the strength of the nematic order. For perfect alignment along the director ($f(\theta) = \delta(\theta)/2\pi$), S equals one. In the isotropic case ($f(\theta) = 1/4\pi$), S equals zero.

The non-diagonal terms in the matrix representation of $\boldsymbol{Q}$ vanish, since there is an equally probable orientation $\vec{n}''$ for every orientation $\vec{n}'$ of a molecule, which fulfils the condition

$$n'_a n'_b = -n''_a n''_b \text{ for } a \neq b. \tag{6}$$

This condition can easily be validated with the help of Figure 1*d*.

For an arbitrary choice of the coordinate system $\vec{e}'_x, \vec{e}'_y, \vec{e}'_z$ the order parameter will not have a diagonal shape. However, there is always an orthogonal matrix $\boldsymbol{O}$, that diagonalizes the order parameter tensor, such that

$$\boldsymbol{Q}^{\mathrm{D}} = \boldsymbol{O}\boldsymbol{Q}\boldsymbol{O}^{\mathrm{T}} = S\begin{pmatrix} -\frac{1}{2} & 0 & 0 \\ 0 & -\frac{1}{2} & 0 \\ 0 & 0 & 1 \end{pmatrix}. \tag{7}$$

The director $\vec{n}$ is then given by the eigenvector of $\boldsymbol{Q}$ that corresponds to the third eigenvalue. This means in practice that

$$\vec{n} = \boldsymbol{O}\vec{e}_z'. \tag{8}$$

In total, the order parameter contains the information on the director orientation and the strength of the nematic order. I want to mention, that the order parameter can also be written in terms of the director instead of the average over molecule orientations

$$Q_{ij} = \frac{1}{2}S\left(3n_i n_j - \delta_{ij}\right). \tag{9}$$

Due to the strong orientational order of liquid crystals, their physical properties are often strongly anisotropic. An important example is the anisotropic permittivity at low frequencies, which can be used to align liquid crystals with an electric field. The alignment of liquid crystals via electric fields will be discussed in the sections 2.1.1 and 2.1.2.

The anisotropy of the permittivity at optical frequencies is the reason for the strong birefringence in liquid crystals. This is a challenge in 3D laser printing of liquid-crystal elastomers, since it requires to tightly focus a laser beam into a liquid-crystal resin. For that reason, I introduce the fundamentals of birefringence in section 2.2. Also, I discuss how to focus light into a liquid crystal in section 2.3.

The degree of anisotropy depends on the nematic strength. If the molecules are less well aligned, the anisotropy is less pronounced. Since the order of the molecules decreases with increasing temperature, the nematic strength decreases with increasing temperature as well. At a critical temperature, a phase transition happens to the isotropic phase. The behaviour of the nematic strength close to the phase transition is described by the Landau-deGennes theory discussed in the next section.

2.1.1 Landau-deGennes Theory

In this section, the Landau-deGennes theory describing the nematic to isotropic phase transition is introduced. The theory assumes that the order parameter is small close to the phase transition. In this case, the free energy of the liquid crystal can be expanded in powers of Q_{ij}. The expansion must contain uneven orders of $\boldsymbol{Q}$, since $\boldsymbol{Q}$ and $-\boldsymbol{Q}$

represent different physical realizations, which can easily be seen for example for $S = 0.5$ and $S = -0.5$. In the first case it is

$$\langle n_3' n_3' \rangle = \frac{2}{3}, \tag{10}$$

which represents a decent alignment of the molecules along the director, while in the second case it is

$$\langle n_3' n_3' \rangle = 0\,, \tag{11}$$

which represents an orientation of the molecules perpendicular to the director. Since the trace of the order parameter vanishes, the first order in the expansion vanishes. In total the expansion up the fourth order in $\boldsymbol{Q}$ is given by

$$\begin{aligned} F = F_0 + \frac{2}{3}A(T - T^*)Q_{ij}Q_{ji} - \frac{4}{3}BQ_{ij}Q_{jk}Q_{ki} \\ + \frac{2}{9}C\left[\left(Q_{ij}Q_{ji}\right)^2 + 2Q_{ij}Q_{jk}Q_{kl}Q_{li}\right]. \end{aligned} \tag{12}$$

In this expansion the temperature dependence of the factor in the quadratic order is approximated to be linear and completely neglected in the higher order terms. Inserting the definition of $\boldsymbol{Q}$ results in

$$F(S,T) = F_0 + A(T - T^*)S^2 - BS^3 + CS^4. \tag{13}$$

To obtain the nematic strength S for a given temperature T, the free energy must be minimal. The free energy is minimal for

$$S = \begin{cases} 0 & \text{for } T \geq T_{\mathrm{ni}} = T^* + \dfrac{B^2}{4AC} \\ \dfrac{3B + \sqrt{9B^2 - 32AC(T - T^*)}}{8C} & \text{for } T \leq T_{\mathrm{ni}} \end{cases}. \tag{14}$$

The nematic strength is plotted versus the temperature in Figure 2*a* for temperatures close to the critical temperature T_{ni}. At the critical temperature T_{ni} there is a jump in S of

$$\Delta S = \frac{B}{2C}, \tag{15}$$

indicating a first order phase transition. Due to the phenomena of supercooling and superheating, the phase transition often does not occur at the critical temperature but

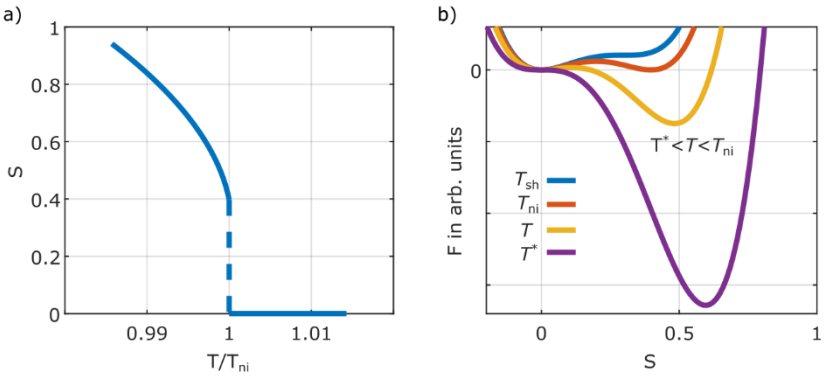

Figure 2. (a) Nematic strength versus the temperature close to the critical temperature T_{ni}. At this temperature a first order phase transition to the isotropic phase occurs. (b) The free energy is depicted for different temperatures. At T_{sh} the metastable nematic phase becomes instable. At T_{ni} the nematic and the isotropic phase have the same free energy. Between T^* and T_{ni} the isotropic phase is metastable. At T^* the metastable isotropic phase becomes instable.

slightly above or below. For example, the isotropic phase represents a metastable equilibrium for $T^* < T < T_{\mathrm{ni}}$, since

$$\frac{\partial^2 F}{\partial S^2}(S = 0, T) > 0 \text{ for } T > T^*. \tag{16}$$

This means, that on slow cooling from the isotropic phase, the isotropic to nematic transition appears at $T^* < T_{\mathrm{ni}}$. This effect is called supercooling. For

$$T_{\mathrm{ni}} < T < T_{\mathrm{sh}} = T^* + \frac{9}{8}\frac{B^2}{4AC}, \tag{17}$$

the nematic phase represents a metastable equilibrium. On slow heating from the nematic phase, the nematic to isotropic transition appears at $T_{\mathrm{sh}} > T_{\mathrm{ni}}$. This is called superheating. Figure 2*b* shows the free energy versus the nematic strength for $T^*, T_{\mathrm{ni}}, T_{\mathrm{sh}}$ and a temperature $T^* < T < T_{\mathrm{ni}}$. The metastable equilibrium states are clearly visible.

Within the presented approximation, the entropy is given by

$$s(V, T) = -\left(\frac{\partial F}{\partial T}\right)_V = -AS^2. \tag{18}$$

From this equation the latent heat at the phase transition can be calculated. It is given by

$$\Delta Q = T_{\mathrm{ni}} \Delta s = T_{\mathrm{ni}} \frac{AB^2}{4C^2}. \tag{19}$$

The constants A, B, C that appear in the expression for the free energy can be roughly estimated from simple observations. Mean field theories predict the phase transition of liquid crystals for a nematic strength of about $S \approx 0.4$ [75]. From equation (15) it follows

$$B \approx 0.8C\,. \tag{20}$$

Assuming $T_{ni} - T^* \approx 1\ \mathrm{K}$ [76] results with equation (14) in

$$B^2 = 4AC \cdot 1\ \mathrm{K}\,. \tag{21}$$

Finally, the latent heat is usually on the order of $1 - 2\ \mathrm{J \cdot g^{-1}}$ [76]. In comparison, this is three orders of magnitude lower than for water. 5CB for example shows a latent heat of about $1.6\ \mathrm{J \cdot g^{-1}}$ [77], a density of $1\ \mathrm{g \cdot cm^{-3}}$ [78] and $T_{\mathrm{ni}} \approx 308\ \mathrm{K}$ [77]. Together with equation (19), the three observations result in

$$A \approx 3.2 \cdot 10^4 \frac{\mathrm{J}}{\mathrm{m^3 K}}\,,\ B \approx 1.6 \cdot 10^5 \frac{\mathrm{J}}{\mathrm{m^3}},\ C \approx 2.0 \cdot 10^5 \frac{\mathrm{J}}{\mathrm{m^3}}. \tag{22}$$

The application of an external force, that aligns the liquid-crystal molecules to a common direction adds new phenomena to the already discussed thermal behaviour. Especially, the external force prevents the transition to the isotropic phase on heating. Instead there is a transition to a para-nematic phase that still retains a nematic strength $S > 0$. For strong forces the behaviour becomes super-critical. This behaviour can easily be studied theoretically with electric fields representing the aligning external force. In the presence of electric fields, the free energy must be corrected by the term

$$W = -\frac{\epsilon_0}{2} E_i \epsilon_{ij} E_j \tag{23}$$

with

$$\epsilon_{ij} = \frac{2}{3} \Delta\epsilon Q_{ij} + \bar{\epsilon}\delta_{ij}, \tag{24}$$

$$\Delta\epsilon = \epsilon_{\parallel} - \epsilon_{\perp}, \tag{25}$$

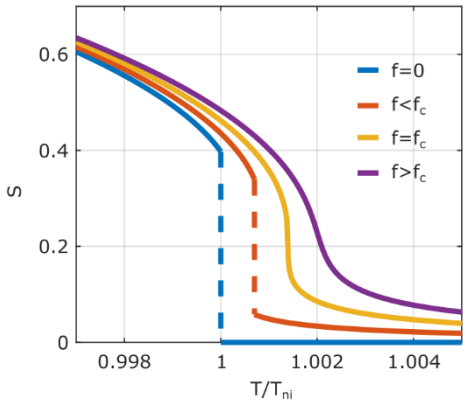

Figure 3. At the presence of an aligning force, there is no transition to the isotropic phase anymore. For small forces a phase transition to a para-nematic phase occurs. For a critical force, the jump in the nematic strength vanishes. For forces above the critical force, the behaviour is called supercritical.

$$\bar{\epsilon} = \frac{1}{3}\epsilon_{\parallel} + \frac{2}{3}\epsilon_{\perp}. \tag{26}$$

$\epsilon_{\parallel}$ represents the permittivity along the director, while $\epsilon_{\perp}$ represents the permittivity perpendicular to the director. Inserting the definition of the order parameter $\boldsymbol{Q}$ results in

$$W = -\frac{\epsilon_0}{2}\left(\frac{1}{3}\Delta\epsilon S(3(E_i n_i)^2 - E^2) + \bar{\epsilon}E^2\right). \tag{27}$$

Assuming that the liquid crystals are free to rotate, the energy becomes minimal, when the director and the field are in parallel. In total the free energy becomes

$$F(S,T) = F_0 + A(T - T^*)S^2 - BS^3 + CS^4 - fS \tag{28}$$

with

$$f = -\frac{\epsilon_0}{3}\Delta\epsilon E^2. \tag{29}$$

The terms in W that are not proportional to S are absorbed in F_0.

It turns out, that there is no easy to obtain analytical solution for $S(T)$ anymore. However, solutions for different field strengths are plotted in *Figure 3*. For a small non-vanishing electric field there is still a jump in S at the phase transition, however, the nematic strength does not drop to zero. It is a phase transition to a so-called para-nematic phase. At a critical field strength, the jump in S vanishes and above the critical field strength, the behaviour is called super-critical. The critical point is reached for

$$f_c = \frac{B^3}{16C^2} \quad [76]. \tag{30}$$

For 5CB this results in a critical field around $14\ \mathrm{V\ \mu m^{-1}}$ which represents a rather large electric field.

Such a behaviour will also be important when I talk about liquid-crystal elastomers. However, there it is not an electric field that aligns the liquid crystals but the cross-links that restrict the rotation of the rod-like constituents and therefore induce a supercritical behaviour [79].

2.1.2 Distorted Nematic Liquid Crystals

Up to now, a liquid crystal with a homogeneous spatial director profile was implicitly assumed. However, in reality the spatial director profile is distorted. This can happen due to a prescribed alignment of the molecules at the walls of a container or due to an applied electric or magnetic field. Assuming that the distortion of the director field occurs on a much larger scale than the size of the molecules allows to formulate a continuum theory.

In the continuum theory, it is assumed that there is a volume around every point $\vec{x}$ in space that is small enough to contain only molecules that in average align along a common director $\vec{n}(\vec{x})$. On the other hand, the volume is supposed to be so large, that the notion of long-range order and the definition of an order parameter Q within this volume is meaningful. Furthermore, it is assumed that the nematic strength is not affected by the distortions. These assumptions lead to a spatially varying order parameter

$$Q_{ij}(\vec{x}) = \frac{1}{2} S\left(3n_i(\vec{x})n_j(\vec{x}) - \delta_{ij}\right). \tag{31}$$

To predict the director field, the free energy arising from the distortion has to be minimized. The free energy is given by the Frank-Oseen-Zocher free energy

$$F_\mathrm{d} = \int f_\mathrm{d} \mathrm{d}^3x \tag{32}$$

with

$$f_\mathrm{d} = \frac{1}{2}K_1\left(\nabla \cdot \vec{n}(\vec{x})\right)^2 + \frac{1}{2}K_2\left(\vec{n}(\vec{x}) \cdot \nabla \times \vec{n}(\vec{x})\right)^2 + \\ + \frac{1}{2}K_3\left(\vec{n}(\vec{x}) \times \nabla \times \vec{n}(\vec{x})\right)^2. \tag{33}$$

The interpretation of the individual terms is illustrated in Figure 4. Director fields with a non-zero divergence are called splay fields. An example of a splay field is given in Figure 4*b*. On the other hand, one speaks of a twist field, when $\vec{n} \cdot \nabla \times \vec{n} \neq 0$. An

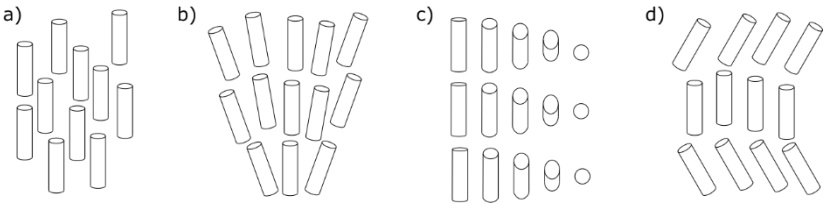

Figure 4. (a) Undisturbed equilibrium state of a nematic liquid crystal. (b) Example for a splay field that results in $\nabla \cdot \vec{n} \neq 0$. (c) Example of a twist fields that leads to $\vec{n} \cdot \nabla \times \vec{n} \neq 0$. The molecules are rotating out of the plane. (d) Example of a bending field that leads to $\vec{n} \times \nabla \times \vec{n} \neq 0$.

exemplary twist field is depicted in Figure 4*c*. For $\vec{n} \times \nabla \times \vec{n} \neq 0$ the director field shows a bending as shown in Figure 4*d*.

The constants K_i are called Frank constants. At 25 °C, the Frank constants for 5CB are approximately [80]

$$K_1 \approx 0.6 \cdot 10^{-11}\ \mathrm{N}, \tag{34}$$

$$K_2 \approx 0.3 \cdot 10^{-11}\ \mathrm{N}, \tag{35}$$

$$K_3 \approx 0.8 \cdot 10^{-11}\mathrm{N}. \tag{36}$$

As already mentioned, the director can also be manipulated by electric fields. To model the effect of electric fields, equation (27) has to be added to the Frank-Oseen-Zocher free energy. Neglecting the terms that do not depend on the director field, one obtains

$$\begin{aligned} f_\mathrm{d} = \frac{1}{2}K_1\left(\nabla \cdot \vec{n}(\vec{x})\right)^2 + \frac{1}{2}K_2\left(\vec{n}(\vec{x}) \cdot \nabla \times \vec{n}(\vec{x})\right)^2 \\ + \frac{1}{2}K_3\left(\vec{n}(\vec{x}) \times \nabla \times \vec{n}(\vec{x})\right)^2 - \frac{\epsilon_0}{2}\Delta\epsilon S\left(\vec{\mathrm{E}} \cdot \vec{\mathrm{n}}\right)^2. \end{aligned} \tag{37}$$

For 5CB the difference in the permittivity is $S\Delta\epsilon \approx 11$ at 25 °C [81].

In the following, I want to discuss an example that shows, how a prescribed alignment at a surface influences the director profile in the volume while an electric field is present at the same time. The example is illustrated in Figure 5*a*. The orientation of the director is along the z-axis at the surface going through the origin of the coordinate system.

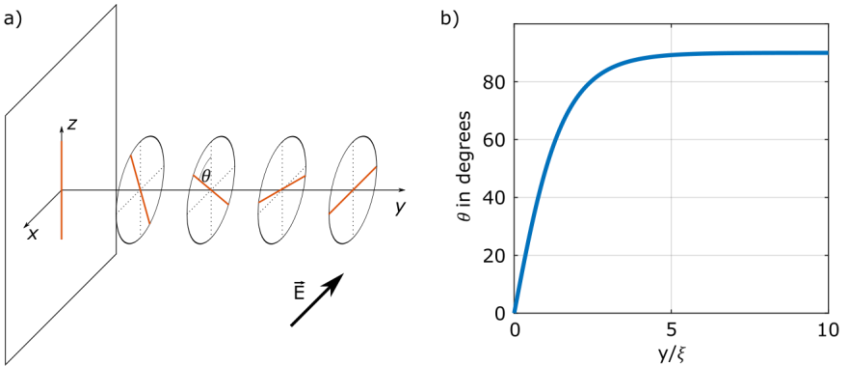

Figure 5. (a) The orientation of the director (red) is prescribed at the surface on the left. At the same time an electric field prescribes the orientation of the director far away from the surface. In between, the surface and the electric field determine the orientation of the director. (b) Orientation of the director versus the distance from the surface. At about 5ξ the director is fully aligned with the electric field.

In an experiment this could be achieved by a polymer surface that is rubbed with a cotton cloth. Additionally, a homogeneous electric field is applied in the x – direction. The electric field causes the director to be aligned along the x – direction far away from the rubbed surface. In between, a rotation of the director must occur. The orientation of the director is fully described by the angle θ defined in Figure 5a. With the ansatz

$$\vec{n} = \begin{pmatrix} \sin\theta \\ 0 \\ \cos\theta \end{pmatrix}, \tag{38}$$

the free energy density is given by

$$f_{\mathrm{d}} = \frac{K_2}{2}\left(\frac{\partial\theta}{\partial y}\right)^2 - \frac{\epsilon_0}{2}\Delta\epsilon S E^2 \sin^2\theta\,. \tag{39}$$

The application of the Euler- Lagrange Equation results in the differential equation

$$\xi^2 \frac{\mathrm{d}^2\theta}{\mathrm{d}y^2} + \sin\theta\cos\theta = 0 \tag{40}$$

with the electric coherence length

$$\xi = \sqrt{\frac{K_2}{\epsilon_0 \Delta\epsilon S}}\frac{1}{E}. \tag{41}$$

The solution to equation (40) is given by [74]

$$\theta(y) = \frac{\pi}{2} - 2\tan^{-1}\left[\exp\left(-\frac{y}{\xi}\right)\right]. \tag{42}$$

The angle $\theta(y)$ is plotted in Figure 5*b*. The figure shows, that after about 5ξ the director points along the direction of the electric field. For 5CB the electric coherence length is about $\xi \approx 0.35\ \mu\text{m}$ for an electric field strength of $E = 0.5\ \text{V} \cdot \mu\text{m}^{-1}$. That means, that for such high electric field strengths, the influence of the surface can already be neglected at a distance of $2\ \mu\text{m}$. This is a justification for the simplifying assumption in chapter 3.2 that the liquid crystals are aligned with the electric field at every point in the volume.

2.1.3 Liquid-Crystal Elastomers

Nematic liquid-crystal elastomers are elastomers formed from nematic monomers. Like ordinary nematic liquid crystals, the nematic monomers contain a rigid and rod-like core that leads to a nematic phase. On top of that, they are equipped with one or more functional groups that allow to connect and cross-link the monomers in a polymerization reaction. Due to the tendency of the rigid cores to align in parallel along the director, the resulting elastomer is anisotropic even after the polymerization reaction. An illustration of such an elastomer is given in Figure 6*a*. Such a liquid-crystal elastomer behaves anisotropic in all kind of properties. Especially, it shows uniaxial birefringence with the director representing the optic axis.

Heating the liquid-crystal elastomer leads to a reduction of the order parameter as for common liquid crystals. This means that the orientation of the rigid cores deviates more and more from the director, leading to a less anisotropic elastomer. As a consequence, the polymer backbone deforms such, that the elastomer expands perpendicular to the director and shrinks along the director. This is illustrated in Figure 6*b*.

Weakly cross-linked liquid-crystal elastomers show at some point a first order phase transition. In these elastomers, the order parameter quickly drops close to zero for a small temperature step of a few Kelvins. This leads to a sudden deformation of the liquid-crystal elastomer in a small temperature step [82, 83]. The sudden drop in the order parameter is similar as for ordinary liquid crystals.

In principle, liquid-crystal elastomers should show a first order phase transition to the isotropic phase at a certain temperature as discussed in section 2.1.1. However, in reality the composition of liquid-crystal elastomers usually slightly varies in space, which leads to different phase transition temperatures at different positions in space. This

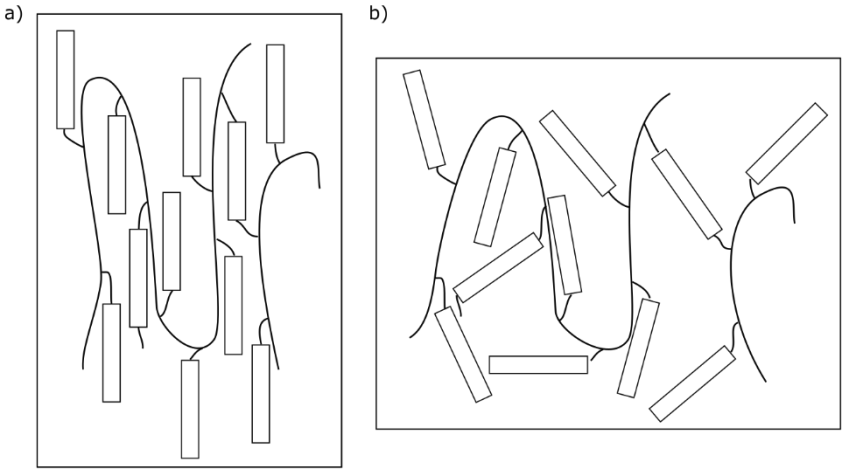

Figure 6. (a) A liquid-crystal elastomer in the nematic state with high nematic strength. The polymer backbone is highly anisotropic. (b) At elevated temperatures, the nematic strength is lower, which leads to a less anisotropic polymer backbone. On the macroscopic scale, the liquid-crystal elastomer shrinks along the director and expands perpendicular to it.

smears out the thermal response. On top of that, the cross-links restrict the motion of the rigid cores and therefore force them to align along the director even at elevated temperatures. As discussed in section 2.1.1 this prevents a phase transition to the isotropic phase and leads either to a transition to a para-nematic phase or a supercritical behaviour for a large cross-linking density. Experimental evidence suggests that in real liquid-crystal elastomers the cross-linking density varies in space and therefore also the thermal response of the liquid-crystal elastomer. It might even be that some parts of a liquid-crystal elastomer show a transition to a para-nematic phase, while others behave supercritical [79].

In the liquid-crystal elastomers discussed in this thesis, the cross-linking density seems to be sufficiently high, that I did not observe a sudden deformation for a certain temperature. Actually, I observed a continuous deformation on heating starting at room temperature up to more than 200 °C. A measurement of the anisotropic thermal expansion is shown in Figure *27* in chapter 3.5.

2.2 Birefringence

In this thesis, I present structures made of liquid-crystal elastomer which were 3D printed from a liquid-crystal resin. For this technique a laser must be tightly focused into the highly birefringent liquid-crystal resin in order to start a polymerization reaction, which I explain in further detail in chapter 3. In addition, the printed liquid-crystal elastomer structures are also birefringent and I exploit this to estimate the director orientation within the printed samples. For both cases it is important to understand the concepts of birefringence. The following introduction mainly follows the theoretical optics lecture held by Carsten Rockstuhl.

In birefringent systems, the permittivity $\boldsymbol{\epsilon}$ is a second-order tensor. In general, this means, that the direction of the electric displacement field $\vec{D}$ does not coincide with the direction of the electric field $\vec{E}$, since both are connected by the permittivity tensor as described by

$$\vec{D} = \epsilon_0 \boldsymbol{\epsilon} \vec{E}. \tag{43}$$

Only along a principal axis of the permittivity tensor the directions of both vectors coincide. In the principal system the permittivity becomes diagonal and can be expressed by

$$\boldsymbol{\epsilon} = \begin{pmatrix} \epsilon_1 & 0 & 0 \\ 0 & \epsilon_2 & 0 \\ 0 & 0 & \epsilon_3 \end{pmatrix}. \tag{44}$$

To obtain the eigenmodes inside a birefringent medium, Maxwell's equations have to be solved. After a Fourier transform, Maxwell's equations are represented by the following four equations assuming a permeability of one:

$$\vec{k} \cdot \vec{D} = 0 \tag{45}$$

$$\vec{k} \cdot \vec{H} = 0 \tag{46}$$

$$\vec{k} \times \vec{E} = \omega \mu_0 \vec{H} \tag{47}$$

$$\vec{k} \times \vec{H} = -\omega \vec{D}. \tag{48}$$

Using equation (47) and (48) the following wave equation can be extracted from Maxwell's equation

$$-\vec{k} \times \left(\vec{k} \times \vec{E}\right) = -\vec{k}\left(\vec{k} \cdot \vec{E}\right) + k^2 \vec{E} = \frac{\omega^2}{c_0^2} \frac{1}{\epsilon_0} \vec{D}. \tag{49}$$

With equation (43) the $\vec{D}$ – field in the wave equation can be eliminated to obtain

$$\left(\frac{\omega^2}{c_0^2} \epsilon_i - k^2\right) E_i + k_i \sum_{j=1}^{3} k_j E_j = 0. \tag{50}$$

Inserting the dispersion relation

$$\vec{k} = \frac{\omega}{c_0} n \vec{u} \text{ with } |\vec{u}| = 1 \tag{51}$$

into the wave equation results in the final representation of the wave equation

$$(\epsilon_i - n^2) E_i + n^2 u_i \sum_{j=1}^{3} u_j E_j = 0. \tag{52}$$

This wave equation represents a set of linear equations which only has nontrivial solutions if the determinant of the matrix of coefficients is zero leading to

$$\begin{aligned} u_1^2 (n^2 - \epsilon_2)(n^2 - \epsilon_3) n^2 + u_2^2 (n^2 - \epsilon_1)(n^2 - \epsilon_3) n^2 + \\ + u_3^2 (n^2 - \epsilon_1)(n^2 - \epsilon_2) n^2 \\ = (n^2 - \epsilon_1)(n^2 - \epsilon_2)(n^2 - \epsilon_3). \end{aligned} \tag{53}$$

Due to the rotational symmetry of liquid crystals around the director, two eigenvalues of the permittivity tensor are equal. We choose the principal system such that the permittivity is defined by

$$\epsilon_1 = \epsilon_2 = \epsilon_{\mathrm{or}} \text{ and } \epsilon_3 = \epsilon_{\mathrm{e}} . \tag{54}$$

Inserting this permittivity tensor into equation (53) leads to

$$\begin{aligned} u_2^2 (n^2 - \epsilon_e)(n^2 - \epsilon_{or}) n^2 + u_2^2 (n^2 - \epsilon_e)(n^2 - \epsilon_{or}) n^2 + u_3^2 (n^2 - \epsilon_{or})^2 \\ = (n^2 - \epsilon_{or})^2 (n^2 - \epsilon_e). \end{aligned} \tag{55}$$

This equation has two solutions. Either

$$n^2 = \epsilon_{\mathrm{or}} \tag{56}$$

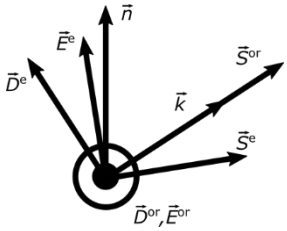

Figure 7. The director $\vec{n}$ represents the optic axis of a liquid crystal. For a given wave vector $\vec{k}$, the ordinary mode is polarized perpendicular the plane spanned by the director and the wave vector. The extraordinary mode is polarized within this plane. The $\vec{D}$ – field is perpendicular to the wave vector, the $\vec{E}$ – field is not. The Poynting vector $\vec{S}^{\mathrm{e}}$ does not coincide with the wave vector.

or

$$\frac{u_3^2}{\epsilon_{\mathrm{or}}} + \frac{u_1^2 + u_2^2}{\epsilon_{\mathrm{e}}} = \frac{1}{n^2}. \tag{57}$$

This means that there are two eigenmodes, while the refractive index of one mode is independent of the direction of the wave vector. This mode is called the ordinary mode. The refractive index of the second mode depends on the direction of the wave vector. This mode is called the extraordinary mode. For a wave travelling along the director both modes correspond to the same refractive index. This special direction is also called the optic axis. Since there is only one optic axis, such media are called uniaxial.

To obtain the polarization of the two modes, the wave equation (52) can be used. For the ordinary mode it directly results in

$$\vec{u} \cdot \vec{E}^{\mathrm{or}} = 0 \tag{58}$$

and

$$E_3^{\mathrm{or}} = 0. \tag{59}$$

Using both, one can obtain the statement

$$\frac{E_1^{\mathrm{or}}}{E_2^{\mathrm{or}}} = \frac{u_2}{u_1} \in \mathbb{R}. \tag{60}$$

This means that the ordinary mode is linearly polarized. According to equation (43) it directly follows from equation (54) and (59) that

$$\vec{D}^{\mathrm{or}} \parallel \vec{E}^{\mathrm{or}}. \tag{61}$$

For the extraordinary mode, equation (52) can be used to obtain the fraction between two arbitrary components of the electric field vector. The fraction is given by

$$\frac{E_i^{\mathrm{e}}}{E_j^{\mathrm{e}}} = \frac{n^2 - \epsilon_j}{n^2 - \epsilon_i}\frac{u_i}{u_j} \in \mathbb{R}\,. \tag{62}$$

Since the fraction is real for all components, the extraordinary eigenmode is also linearly polarized. Furthermore, it can be shown that the ordinary and extraordinary modes are perpendicular to each other. From equations (52), (54) and (59) it directly follows that

$$\vec{E}^{\mathrm{e}} \cdot \vec{E}^{\mathrm{or}} \propto \frac{n^2 u_1}{n^2 - \epsilon_{\mathrm{or}}} E_1^{\mathrm{or}} + \frac{n^2 u_2}{n^2 - \epsilon_{\mathrm{or}}} E_2^{\mathrm{or}} = \frac{n^2}{n^2 - \epsilon_{\mathrm{or}}} \vec{u} \cdot \vec{E}^{\mathrm{or}} = 0. \tag{63}$$

Similarly, it can be shown, that

$$\vec{D}^{\mathrm{e}} \cdot \vec{D}^{\mathrm{or}} = 0\,. \tag{64}$$

Figure 7 summarizes all the obtained relations for the $\vec{E}$ – and $\vec{D}$ – fields of the ordinary and the extraordinary modes for a given wave vector. It also shows the Poynting vectors of the ordinary and the extraordinary modes that are defined by

$$\vec{S} = \vec{E} \times \vec{H}. \tag{65}$$

For the extraordinary mode, the directions of the wavevector and the Poynting vector do not coincide, since the directions of the electric field $\vec{E}^{\mathrm{e}}$ and $\vec{D}^{\mathrm{e}}$ do not coincide.

2.2.1 4×4 Matrix Formalism

At an interface between two media light gets refracted. For birefringent media the refraction is not easy to predict, since the refractive index depends in general on the direction of the wave vector. A formalism that provides an easy to follow recipe to calculate the refracted fields inside birefringent media is the 4×4 matrix formalism. It even allows to propagate light through a stack of different birefringent layers. The following theory closely follows the book of Pochi Yeh [84].

Let us start with a stack of N birefringent layers with a surface normal in z – direction. The stack is embedded inside two different semi-infinitely extended media. The permittivity tensor of such a stack is given by

$$\boldsymbol{\epsilon} = \begin{cases} \boldsymbol{\epsilon}(0) & z < z_0 \\ \boldsymbol{\epsilon}(1) & z_0 < z < z_1 \\ \boldsymbol{\epsilon}(2) & z_1 < z < z_2 \\ \vdots & \\ \boldsymbol{\epsilon}(N) & z_{N-1} < z < z_N \\ \boldsymbol{\epsilon}(N+1) & z_N < z \end{cases} . \tag{66}$$

For a wave passing the stack, the components k_x and k_y of the wave vector $\vec{k}$ are the same in every layer due to translational symmetry in x – and y – direction. To obtain the possible modes within every layer for given k_x, k_y the wave equation must be solved. The wave equation was already derived in the last section and is given by

$$\vec{k} \times \left(\vec{k} \times \vec{E}\right) + k_0^2 \boldsymbol{\epsilon} \vec{E} = 0 . \tag{67}$$

This set of linear equations can be expressed as

$$\begin{pmatrix} k_0^2\epsilon_{xx} - k_y^2 - k_z^2 & k_0^2\epsilon_{xy} + k_x k_y & k_0^2\epsilon_{xz} + k_x k_z \\ k_0^2\epsilon_{yx} + k_y k_x & k_0^2\epsilon_{yy} - k_x^2 - k_z^2 & k_0^2\epsilon_{yz} + k_y k_z \\ k_0^2\epsilon_{zx} + k_z k_x & k_0^2\epsilon_{zy} + k_z k_y & k_0^2\epsilon_{zz} - k_x^2 - k_y^2 \end{pmatrix} \begin{pmatrix} E_x \\ E_y \\ E_z \end{pmatrix} = 0. \tag{68}$$

For non-trivial solutions, the determinant of the coefficient matrix must be zero. This results in an equation of fourth order in k_z with four roots and therefore four modes. Some of these modes might be evanescent if k_z is complex. Modes with $k_z < 0$ represent back reflected modes, while modes with $k_z > 0$ represent modes that travel forwards. For every root $k_z^\sigma, \sigma = 1 \dots 4$ a normalized vector $\vec{p}_\sigma$ can be found that solves the wave equation. In the case of degenerate roots, orthonormal vectors that span the solution space can be found. The roots are degenerate in isotropic media or for propagation along the optic axis in uniaxial media.

With these solutions the electric field within layer n can be written as a superposition of the estimated eigenmodes within the layer.

$$\vec{E} = \sum_{\sigma=1}^{4} A_\sigma(n) \vec{p}_\sigma(n) \exp\{i[\omega t - k_x x - k_y y - k_z^\sigma(n)(z - z_n)\} \tag{69}$$

According to Maxwell's equation (47) the $\vec{H}$ – field is then given by

$$\vec{H} = \sum_{\sigma=1}^{4} A_\sigma(n) \vec{q}_\sigma(n) \exp\{i[\omega t - k_x x - k_y y - k_z^\sigma(n)(z - z_n)]\} \tag{70}$$

with
$$\vec{q}_\sigma(n) = \frac{\vec{k}_\sigma(n) \times \vec{p}_\sigma(n)}{\omega\mu_0}. \tag{71}$$

The remaining task is to estimate the coefficients $A_\sigma(n)$ for each layer. This is done by enforcing the continuity of E_x, E_y, H_x and H_y at the interfaces, as demanded by the Maxwell's equations. Imposing continuity at the interface $z = z_{n-1}$ leads to

$$\sum_{\sigma=1}^{4} A_\sigma(n-1)\vec{p}_\sigma(n-1)\cdot\vec{x} = \sum_{\sigma=1}^{4} A_\sigma(n)\vec{p}_\sigma(n)\cdot\vec{x}\exp\{ik_z^\sigma(n)t_n\} \tag{72}$$

$$\sum_{\sigma=1}^{4} A_\sigma(n-1)\vec{p}_\sigma(n-1)\cdot\vec{y} = \sum_{\sigma=1}^{4} A_\sigma(n)\vec{p}_\sigma(n)\cdot\vec{y}\exp\{ik_z^\sigma(n)t_n\} \tag{73}$$

$$\sum_{\sigma=1}^{4} A_\sigma(n-1)\vec{q}_\sigma(n-1)\cdot\vec{x} = \sum_{\sigma=1}^{4} A_\sigma(n)\vec{q}_\sigma(n)\cdot\vec{x}\exp\{ik_z^\sigma(n)t_n\} \tag{74}$$

$$\sum_{\sigma=1}^{4} A_\sigma(n-1)\vec{q}_\sigma(n-1)\cdot\vec{y} = \sum_{\sigma=1}^{4} A_\sigma(n)\vec{q}_\sigma(n)\cdot\vec{y}\exp\{ik_z^\sigma(n)t_n\} \tag{75}$$

with $t_n = z_n - z_{n-1}$. This set of equations can be rewritten in terms of the matrix equation

$$\begin{pmatrix} A_1(n-1) \\ A_2(n-1) \\ A_3(n-1) \\ A_4(n-1) \end{pmatrix} = D^{-1}(n-1)D(n)P(n)\begin{pmatrix} A_1(n) \\ A_2(n) \\ A_3(n) \\ A_4(n) \end{pmatrix}, \tag{76}$$

where
$$D(n) = \begin{pmatrix} \vec{x}\cdot\vec{p}_1(n) & \vec{x}\cdot\vec{p}_2(n) & \vec{x}\cdot\vec{p}_3(n) & \vec{x}\cdot\vec{p}_4(n) \\ \vec{y}\cdot\vec{q}_1(n) & \vec{y}\cdot\vec{q}_2(n) & \vec{y}\cdot\vec{q}_3(n) & \vec{y}\cdot\vec{q}_4(n) \\ \vec{y}\cdot\vec{p}_1(n) & \vec{y}\cdot\vec{p}_2(n) & \vec{y}\cdot\vec{p}_3(n) & \vec{y}\cdot\vec{p}_4(n) \\ \vec{x}\cdot\vec{q}_1(n) & \vec{x}\cdot\vec{q}_2(n) & \vec{x}\cdot\vec{q}_3(n) & \vec{x}\cdot\vec{q}_4(n) \end{pmatrix}, \tag{77}$$

and
$$P(n) = \mathrm{diag}\begin{pmatrix} \exp(ik_z^1(n)t_n) \\ \exp(ik_z^2(n)t_n) \\ \exp(ik_z^3(n)t_n) \\ \exp(ik_z^4(n)t_n) \end{pmatrix}. \tag{78}$$

$D(n)$ is called dynamical matrix and $P(n)$ is called the propagation matrix. With the definition of the transfer matrix

$$T_{n-1,n} = D^{-1}(n-1)D(n)P(n), \tag{79}$$

the matrix equation (76) can be rewritten to

$$\begin{pmatrix} A_1(0) \\ A_2(0) \\ A_3(0) \\ A_4(0) \end{pmatrix} = T_{0,1}T_{1,2}T_{2,3}\cdots T_{N-1,N}T_{N,S} \begin{pmatrix} A_1(N+1) \\ A_2(N+1) \\ A_3(N+1) \\ A_4(N+1) \end{pmatrix}. \tag{80}$$

The knowledge of four coefficients A_σ within the embedding layers allows now to solve the whole system via the transfer matrices. In the next section, this will be applied to an isotropic-uniaxial interface.

2.2.2 Transmission at an Isotropic-Uniaxial Interface

The aim of this section is to give formulas for the energy transmission coefficients at the interface of an isotropic medium and a uniaxial medium. The transmission into the ordinary mode and the extraordinary mode are distinguished.

According to equation (80) the following equation holds at the interface of the isotropic medium and the uniaxial medium

$$\begin{pmatrix} A_1 \\ A_2 \\ A_3 \\ A_4 \end{pmatrix} = T \begin{pmatrix} A_\mathrm{o} \\ 0 \\ A_\mathrm{e} \\ 0 \end{pmatrix}. \tag{81}$$

The modes are ordered such, that A_1 and A_3 correspond to forward traveling waves within the isotropic medium. On the other hand, A_2 and A_4 represent modes that are reflected by the interface and travel backwards in the isotropic medium. The values A_o and A_e represent the transmitted ordinary and extraordinary modes that are travelling forwards in the uniaxial medium. In this scenario, no backwards travelling waves are excited within the uniaxial medium. The transmission matrix T can be calculated as described in the last section.

This set of equations can be solved to obtain

$$A_\mathrm{o} = \frac{T_{33}A_1 - T_{13}A_3}{T_{11}T_{33} - T_{13}T_{31}} \tag{82}$$

and

$$A_\mathrm{e} = \frac{T_{11}A_3 - T_{31}A_1}{T_{11}T_{33} - T_{13}T_{31}}. \tag{83}$$

To calculate the energy transmitted to the ordinary and extraordinary modes, the Poynting vector $\vec{S}$ within the isotropic medium and the Poynting vectors $\vec{S}_\mathrm{o}$ corresponding

to the ordinary mode and $\vec{S}_\mathrm{e}$ corresponding to the extraordinary mode must be calculated by the formulas

$$\vec{S} = \frac{|A_1|^2}{\omega\mu_0}\vec{p}_1 \times \vec{q}_1^* + \frac{|A_3|^2}{\omega\mu_0}\vec{p}_3 \times \vec{q}_3^*, \tag{84}$$

$$\vec{S}_\mathrm{o} = \frac{|A_\mathrm{o}|^2}{\omega\mu_0}\vec{p}_\mathrm{o} \times \vec{q}_\mathrm{o}^*, \tag{85}$$

and

$$\vec{S}_e = \frac{|A_e|^2}{\omega\mu_0}\vec{p}_e \times \vec{q}_e^*. \tag{86}$$

The vectors $\vec{p}$ and $\vec{q}$ have to be estimated as described in the last section. From the Poynting vectors, the energy transmission coefficients T_o and T_e are given by

$$T_\mathrm{o} = \left|\frac{\vec{S}_\mathrm{o} \cdot \vec{z}}{\vec{S} \cdot \vec{z}}\right| \tag{87}$$

and

$$T_\mathrm{e} = \left|\frac{\vec{S}_\mathrm{e} \cdot \vec{z}}{\vec{S} \cdot \vec{z}}\right|. \tag{88}$$

The first coefficient represents the fraction of energy that is transmitted to the ordinary mode, while the second coefficient represents the energy that is transmitted to the extraordinary mode. These formulas are used in the next chapter in a ray optics model for the focusing of light into a birefringent medium. A more sophisticated model used to calculate the intensity distribution within the uniaxial medium is given in the next section.

2.3 Focusing of Optical Fields

Within this section, I describe a method to calculate the intensity distribution in the focus of tightly focused light. I mainly follow the approach presented in the book of Lukas Novotny [85]. At the end of this section, I extend the approach to calculate the intensity distribution at the focus of light focused into a uniaxial medium.

2.3.1 Far-Field

The first step is to establish a link between the field far away from the focus and the field at the position of the focus at $z = 0$. This can be done starting from the angular spectrum representation of the electric field

$$\vec{E}(x,y,z) = \iint_{-\infty}^{\infty} \vec{E}(k_x, k_y; z=0)\, e^{i[k_x x + k_y y + k_z z]} dk_x dk_y. \tag{89}$$

To get an expression for the far field, one has to evaluate the integral (89) at a point $\vec{r}_\infty$ far away from the origin, i.e. $kr \gg 1$ with $r = |\vec{r}_\infty|$. The far field in the direction $\vec{s} = \vec{r}_\infty/r$ can then be written as

$$\vec{E}_\infty(s_x, s_y, s_z) = \iint\limits_{(k_x^2+k_y^2)\leq k^2} \vec{E}(k_x, k_y; z=0) e^{ikr\left[\frac{k_x}{k}s_x + \frac{k_y}{k}s_y + \frac{k_z}{k}s_z\right]} dk_x dk_y. \tag{90}$$

The boundaries of the integral are restricted since, evanescent fields do not contribute to the far field. In the limit of $kr \to \infty$, the method of stationary phase can be used to approximate the integral. According to [85] the far field can be approximated by the equation

$$\vec{E}_\infty(s_x, s_y, s_z) \approx -2\pi i k_z \vec{E}(ks_x, ks_y; z=0) \frac{e^{ikr}}{r}. \tag{91}$$

This means that on one hand that the far field in the direction $\vec{s}$ is fully described by the Fourier coefficient $\vec{E}(ks_x, ks_y; z=0)$ corresponding to the wave vector $\vec{k} = k\vec{s}$. On the other hand, one can calculate the Fourier coefficients of the field in the focus from the far field

$$\vec{E}(k_x, k_y; z=0) = \frac{ire^{-ikr}}{2\pi k_z} \vec{E}_\infty\left(\frac{k_x}{k}, \frac{k_y}{k}, \frac{k_z}{k}\right). \tag{92}$$

With these Fourier coefficients the field can be calculated at every position in space only from the far-field with

$$\vec{E}(x, y, z) = \frac{ire^{-ikr}}{2\pi} \iint\limits_{(k_x^2+k_y^2)\leq k^2} \vec{E}_\infty\left(\frac{k_x}{k}, \frac{k_y}{k}, \frac{k_z}{k}\right) e^{i[k_x x + k_y y + k_z z]} \frac{1}{k_z} dk_x dk_y. \tag{93}$$

In the next section, I use the Richards-Wolf method to obtain an expression for the far field that is created by an aplanatic lens focusing a collimated beam.

2.3.2 Richards-Wolf Method

The Richards-Wolf method is a geometrical optics approach to estimate the field close to the reference sphere of an aplanatic lens used to focus a collimated beam. It is assumed that each ray emerging from the focus gets refracted at a reference sphere with radius f. After this refraction, the ray is assumed to be parallel to the optical axis with a distance

$$h = f \sin\theta, \tag{94}$$

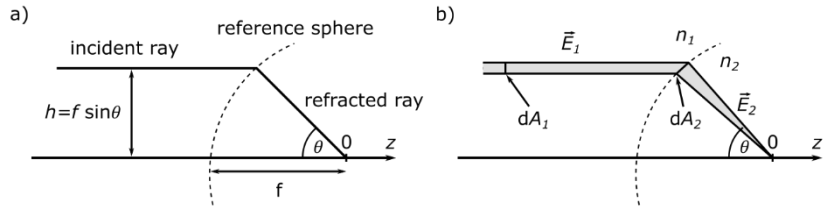

Figure 8. (a) The incident ray parallel to the optical axis is refracted at the reference sphere towards the focal point at $z = 0$. The distance between the focal point and the reference sphere is the focal width f. (b) illustrates the intensity law. For the refracted ray the surface perpendicular to the wave vector is larger at the reference sphere than for the incident ray. Therefore, the intensity of the refracted ray must be lower to fulfil energy conservation.

while θ denotes the orientation of the ray emerging from the focus in spherical coordinates. This situation is depicted in Figure 8a. For the energy conservation to hold, the electric field $\vec{E}_1$ on the left-hand side of the lens and the electric field $\vec{E}_2$ on the right-hand side must be connected by the intensity law

$$E_2 = E_1 \sqrt{\frac{n1}{n2}} \cos^{1/2}\theta, \tag{95}$$

as motivated in Figure 8*b*.

The electric field $\vec{E}_1$ of an incident collimated beam is best described in cylindrical coordinates

$$\vec{E}_1 = [\vec{E}_1 \cdot \vec{n}_\phi]\vec{n}_\phi + [\vec{E}_1 \cdot \vec{n}_\rho]\vec{n}_\rho. \tag{96}$$

In contrast, the refracted field $\vec{E}_\infty$ is best described in spherical coordinates. During the refraction, the s – polarized fields in $\vec{n}_\phi$ – direction stay unaffected. However, the p – polarized fields in $\vec{n}_\rho$ – direction get mapped to the $\vec{n}_\theta$ – direction by the refraction. This is illustrated in Figure *9*. Together with the intensity law (95), the refracted field is given by

$$\vec{E}_\infty = \left([\vec{E}_1 \cdot \vec{n}_\phi]\vec{n}_\phi + [\vec{E}_1 \cdot \vec{n}_\rho]\vec{n}_\theta\right) \sqrt{\frac{n1}{n2}} \cos^{\frac{1}{2}}\theta\,. \tag{97}$$

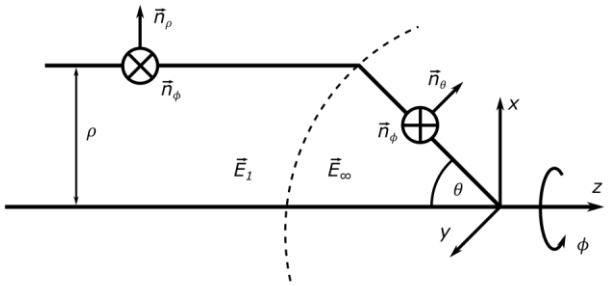

Figure 9. *The incident field $\vec{E}_1$ is described in cylindrical coordinates with the base vectors $\vec{n}_\rho$ and $\vec{n}_\phi$. The refracted field $\vec{E}_\infty$ is described in spherical coordinates with the base vectors $\vec{n}_\theta$ and $\vec{n}_\phi$.*

The subscript ∞ indicates the identification of this refracted field with the far field of the field at the position of the focus. Expressed with cartesian base vectors, the far field is given by

$$\vec{E}_\infty = \left[\vec{E}_{\text{inc}} \cdot \begin{pmatrix} -\sin\phi \\ \cos\phi \\ 0 \end{pmatrix}\right] \begin{pmatrix} -\sin\phi \\ \cos\phi \\ 0 \end{pmatrix} \sqrt{\frac{n1}{n2}} \cos^{\frac{1}{2}}\theta + \\ + \left[\vec{E}_{\text{inc}} \cdot \begin{pmatrix} \cos\phi \\ \sin\phi \\ 0 \end{pmatrix}\right] \begin{pmatrix} \cos\phi\cos\theta \\ \sin\phi\cos\theta \\ -\sin\theta \end{pmatrix} \sqrt{\frac{n1}{n2}} \cos^{\frac{1}{2}}\theta \tag{98}$$

To obtain an expression depending on k_x, k_y and k_z one can use the relations

$$\sin\phi = \frac{k_y}{\sqrt{k_x^2 + k_y^2}}, \tag{99}$$

$$\cos\phi = \frac{k_x}{\sqrt{k_x^2 + k_y^2}}, \tag{100}$$

$$\sin\theta = \frac{\sqrt{k_x^2 + k_y^2}}{k}, \tag{101}$$

and

$$\cos\theta = \frac{k_z}{k}. \tag{102}$$

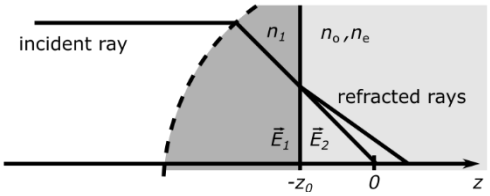

Figure 10. The incident ray is refracted twice. First, at the reference sphere and subsequently at the interface between the isotropic medium and the uniaxial medium. The refractive index in the isotropic medium is n_1. The uniaxial medium is characterized by the ordinary refractive index n_o and the extraordinary refractive index n_e. Within the uniaxial medium an ordinary and an extraordinary mode are excited.

Using the resulting expression $\vec{E}_\infty\left(\frac{k_x}{k},\frac{k_y}{k},\frac{k_z}{k}\right)$, and using formula (93) the focal field is given by

$$\vec{E}(x,y,z) = \frac{ife^{-ikf}}{2\pi} \iint\limits_{(k_x^2+k_y^2)\leq k^2} \vec{E}_\infty\left(\frac{k_x}{k},\frac{k_y}{k},\frac{k_z}{k}\right) e^{i[k_x x+k_y y+k_z z]} \frac{1}{k_z} dk_x dk_y. \quad (103)$$

In this equation the distance r was replaced by the focal width f.

In the following section, this approach is extended to describe the focusing of light into a uniaxial medium.

2.3.3 Focusing into Uniaxial Media

In the 3D printing approach described in this thesis it is important to tightly focus light into a liquid-crystal resin, which is a highly birefringent uniaxial medium. The problem can be modelled as depicted in Figure 10. An aplanatic lens is immersed in an isotropic medium with refractive index n_1. Between the aplanatic lens and the focal plane of the lens, there is an interface at the position $z = -z_0$ separating the isotropic medium and a uniaxial medium. The focal plane of the lens located at $z = 0$ lies within the uniaxial medium.

According to formula (92) and (89) the Fourier coefficients of the field at the interface at $z = -z_0$ within the isotropic medium are given by

$$\vec{E}_1(k_x,k_y;-z_0) = \frac{ire^{-ikr}}{2\pi(k_1)_z}\vec{E}_\infty(k_x,k_y)e^{-i(k_1)_z z_0}. \quad (104)$$

The field within the uniaxial medium at the interface is found by the 4×4 matrix method presented in section 2.2. First, one has to split the field $\vec{E}_1$ into the two forwards propagating eigenmodes $\vec{p}_1, \vec{p}_3$ within the isotropic medium. This results in

$$\vec{E}_1 = A_1\vec{p}_1 + A_3\vec{p}_3 \tag{105}$$

with

$$A_1 = \vec{E}_1(k_x, k_y; -z_0) \cdot \vec{p}_1 \tag{106}$$

and

$$A_3 = \vec{E}_1(k_x, k_y; -z_0) \cdot \vec{p}_3. \tag{107}$$

Then, the coefficients A_o and A_e corresponding to the ordinary and the extraordinary mode in the uniaxial medium can be directly calculated from A_1 and A_3 via the transfer matrix formalism described in section 2.2. With these coefficients, the field $\vec{E}_2$ in the uniaxial medium can be expressed by

$$\vec{E}_2(k_x, k_y; -z_0) = A_\mathrm{o}\vec{p}_\mathrm{o} + A_e\vec{p}_e \tag{108}$$

with the eigenmodes $\vec{p}_\mathrm{o}$ and $\vec{p}_\mathrm{e}$ within the uniaxial medium. Multiplying the respective propagators, the Fourier coefficients at the position $z = 0$ are given by

$$\vec{E}_2(k_x, k_y; 0) = A_\mathrm{o}\vec{p}_\mathrm{o}e^{i(k_\mathrm{o})_z z_0} + A_e\vec{p}_e e^{i(k_\mathrm{e})_z z_0}. \tag{109}$$

From that, the fields close to the focal plane can be expressed in the angular spectrum representation

$$\vec{E}(x, y, z) = \iint_{-\infty}^{\infty} \left[A_\mathrm{o}\vec{p}_\mathrm{o}e^{i(k_\mathrm{o})_z[z_0+z]} + A_e\vec{p}_e e^{i(k_\mathrm{e})_z[z_0+z]}\right] e^{i[k_x x + k_y y]} dk_x dk_y. \tag{110}$$

Results for different orientations of the optic axis and different incident polarizations are presented in the next chapter.

2.4 Continuum Mechanics

In this section, I give a short introduction to continuum mechanics, that mainly follows the book of W.S. Slaughter [86]. The theory of continuum mechanics is important to predict the properties of mechanical metamaterials.

In reality, matter consists of atoms and is therefore discrete. However, if the characteristic length scale of a deformation is much larger than an atom, then the assumption of

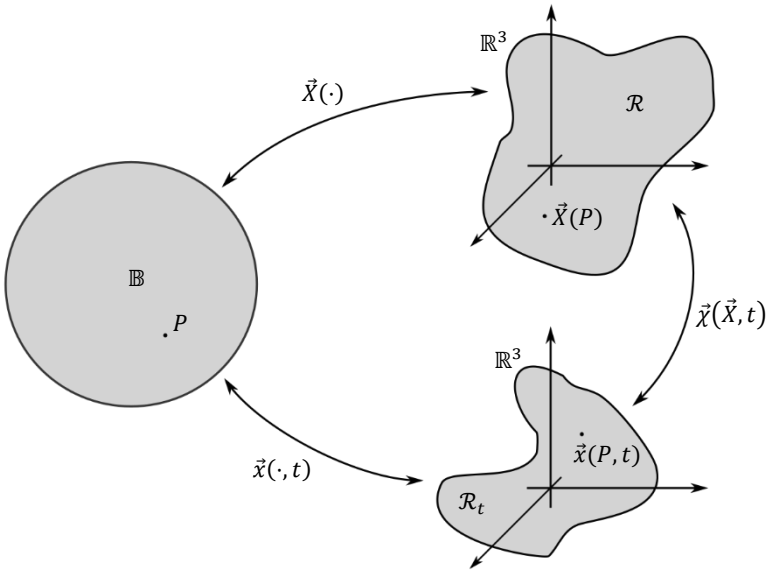

Figure 11. A body $\mathbb{B}$ consists of material points P. In the reference configuration $\mathcal{R}$, representing the undeformed body in space, the material point P is located at the position $\vec{X}(P)$. In the current configuration $\mathcal{R}_t$, representing the deformed configuration at time t, the material point is located at the position $\vec{x}(P,t)$. The current configuration and the reference configuration are linked by the motion $\vec{\chi}$.

a continuous material is justified. This is the basic assumption of continuum mechanics. In continuum mechanics, a body $\mathbb{B}$ is thought to be an infinite set of material points, while a material point is an infinitesimally small amount of matter. A set that consists of coordinates in space, where each coordinate corresponds to a material point in the

body, is called a configuration of the body. The configuration corresponding to the time t is called the current configuration $\mathcal{R}_t$ with

$$\mathcal{R}_t = \{\vec{x}(P,t), P \in \mathbb{B}\}. \tag{111}$$

The configuration of the undeformed body at a time t_0 is called the reference configuration $\mathcal{R}$ with

$$\mathcal{R} = \{\vec{X}(P), P \in \mathbb{B}\}. \tag{112}$$

Every configuration is compared to this reference configuration. The motion χ of the body is a one to one map

$$\chi: (\vec{X}(P), t) \mapsto \vec{x}(P, t), \tag{113}$$

assigning the position of a material point in the reference configuration to the position of the same material point in the current configuration at a time t. It connects the reference configuration with the current configuration. This concept is illustrated in *Figure* 11.

The physical properties of the body are represented by continuous tensor fields $\boldsymbol{T}(P, t)$. These tensor fields can be either expressed in the coordinates of the reference configuration or in coordinates of the current configuration. In the first case, one calls $\boldsymbol{T}(\vec{X}, t)$ the material description and in the second case one calls $\boldsymbol{T}(\vec{x}, t)$ the spatial description of the tensor field. Whenever I address the components of a tensor, I use small letters when I reference a quantity that is described in terms of a base in the current configuration and I use capitalized letters, when the corresponding quantity is described in terms of a base in the reference configuration.

A material path $\mathbb{G}$ is defined as a path inside the body following a line of material points. The shape of the path in space depends on the configuration of the body. The terms material surface and material volume are defined similarly.

In the next subsection, the notions necessary to describe the deformation of a body are explained. This is followed by a description of the stresses inside a body and the equations of motion governing the kinetics of a body. To connect the terms of deformation and stresses a constitutive model is described. Finally, the thermal expansion of bodies is studied including geometrical nonlinearities.

2.4.1 Kinematics

The most obvious way to describe the kinematics of a body is the displacement of the material points relative to the reference configuration. In the material description the displacement field $\vec{u}$ is given by

$$\vec{u}(\vec{X}, t) = \vec{\chi}(\vec{X}, t) - \vec{X}. \tag{114}$$

The displacement field describes the translation, the rotation and the deformation of a body. However, it is also necessary to develop measures for the deformation of a body only.

A possibility to neglect the translation of a body is to describe the positions of each material point in space relative to an arbitrary material point $P \in \mathbb{B}$. To describe the position of a material point $Q \in \mathbb{B}$ relative to P, a material path $\mathbb{G}$ connecting P and Q can be defined. The vector $\vec{r}_{PQ}$ connecting both points in the current configuration is then given by

$$\vec{r}_{PQ} = \int_{\gamma_t} \mathrm{d}\vec{x} = \int_{\gamma} \boldsymbol{F} \cdot \mathrm{d}\vec{X} \tag{115}$$

with

$$F_{iJ}(\vec{X}, t) = \frac{\partial \chi_i(\vec{X}, t)}{\partial X_J}. \tag{116}$$

In this formula, γ_t is the spatial description of the material path $\mathbb{G}$, while γ represents the material description. The tensor $\boldsymbol{F}$ is called the deformation gradient tensor and is defined by equation (116). It allows to calculate the vector connecting two points in the current configuration in coordinates of the reference configuration as described by equation (115). It therefore contains the information about the rotation and the deformation of the body but it excludes the information about the translation of a body.

Calculating only the length s_{PQ} of the path between the two points P and Q leads to a description that only contains the information about the deformation of the body. The length of this path is given by

$$s_{PQ} = \int_{\gamma_t} \mathrm{d}s = \int_{\gamma} \left(\vec{\Upsilon}^{\mathrm{T}} \cdot \boldsymbol{C} \cdot \vec{\Upsilon}\right)^{1/2} \mathrm{d}S \tag{117}$$

with

$$\boldsymbol{C} = \boldsymbol{F}^{\mathrm{T}} \boldsymbol{F}. \tag{118}$$

In this formula, $\vec{\Upsilon}$ is the normal vector tangential to the path γ, while $\boldsymbol{C}$ is called the Right Cauchy Green deformation tensor. With the tensor $\boldsymbol{C}$, the length in the current configuration of a path connecting two material points can be calculated in coordinates of the reference configuration. The integral in equation (117) also gives a local interpretation of $\boldsymbol{C}$. The integrand is the factor, by which the material is locally stretched in the direction of $\vec{\Upsilon}$. This factor is also called the stretch $\Lambda(\vec{\Upsilon})$ and is defined by

$$\Lambda(\vec{\Upsilon}) = \left(\vec{\Upsilon}^{\mathrm{T}} \cdot \boldsymbol{C} \cdot \vec{\Upsilon}\right)^{\frac{1}{2}}. \tag{119}$$

The square roots of the eigenvalues of $C(\vec{X}, t)$ are called the principal stretches. Two of them comprise the smallest and the largest stretch applied to the material at the point $\vec{X}$ at the time t. The corresponding eigenvectors represent the direction of these extremal stretches.

Another quantity that is commonly used to measure deformations of a body is the Lagrange Strain tensor $\boldsymbol{E}$ defined by

$$\boldsymbol{E} = \frac{1}{2}(\boldsymbol{C} - \boldsymbol{I}). \tag{120}$$

It is closely related to the Right Cauchy Green deformation tensor. The Lagrange Strain tensor can be expressed by the displacement field via

$$E_{IJ} = \frac{1}{2}\left(\frac{\partial u_I}{\partial X_J} + \frac{\partial u_J}{\partial X_I} + \frac{\partial u_K}{\partial X_I}\frac{\partial u_K}{\partial X_J}\right). \tag{121}$$

2.4.2 Kinetics

In this section I introduce stress tensors that describe the forces acting within a body. With these stress tensors it is possible to generalize the equations of motion known from mechanics to describe continuous bodies.

External forces are forces acting on a body $\mathbb{B}$ from the outside. They are separated in surface forces acting on $\partial\mathbb{B}$ and body forces acting on $\mathbb{B}$. Internal forces are forces arising from interactions of the body with itself. To study the internal forces, one has to cut out in mind a free body $\mathbb{B}'$ from the body $\mathbb{B}$. Then, the internal forces can be categorized into external forces with respect to the free body and internal forces with respect to the free body. This means that the external forces that act on the free body also include the forces arising from the interactions of the free body with the rest of the body.

To describe the external forces acting on the surface of the free body $\mathbb{B}'$, a material point $P \in \partial\mathbb{B}'$ and a material surface $\Delta\mathbb{S} \subset \partial\mathbb{B}'$ with $P \in \Delta\mathbb{S}$ can be chosen. The total external force on $\Delta\mathbb{S}$ is called $\vec{F}_S$, while the total external torque on $\Delta\mathbb{S}$ with respect to P is called $\vec{M}_S$. Within the theory of continuum mechanics, it is postulated that

a)
$$\lim_{\Delta\mathbb{S}\to P} \frac{\vec{M}_S}{\Delta S} = 0, \tag{122}$$

b)
$$\lim_{\Delta\mathbb{S}\to P} \frac{\vec{F}_S}{\Delta S} = \vec{t}(\vec{X}, \vec{N}, t). \tag{123}$$

Here, ΔS is the spatial description of $\Delta\mathbb{S}$ and $\vec{t}$ is called the traction vector. The traction vector represents the force per unit area acting from the outside of the free body on the surface of the free body at the point P. If P is located within the body $\mathbb{B}$ and not on the surface of the body, then the traction arises from internal forces within the body. This is how the principle of the free body allows to quantify the internal forces within a body. The vector $\vec{N}$ is the normal vector on $\Delta\mathbb{S}$ at the point P in the reference configuration. The dependence of the traction vector on $\vec{N}$ implies that it is postulated that the traction vector does not depend on the choice of the surface but only on the normal vector of the surface at the point P.

It can be shown [86] that there is a second order tensor $\boldsymbol{S}$ that fulfils

$$t_i(\vec{X},\vec{N},t) = N_J S_{Ji}(\vec{X},t) \tag{124}$$

and thus, fully describes all the internal forces acting within a body. For every choice of the free body, the traction is fully described by $\boldsymbol{S}$.

The same procedure can be repeated for the external body forces acting on the free body. To do so, choose a point $Q \in \mathbb{B}'$ and a material volume $\Delta\mathbb{B}'$ that contains the point Q and lies within the free body. The total external force on $\Delta\mathbb{B}'$ is called $\vec{F}_B$ while the total external torque on $\Delta\mathbb{B}'$ with respect to Q is called $\vec{M}_B$. It is postulated that

c) $$\lim_{\Delta\mathbb{B}\to Q} \frac{\vec{M}_B}{\Delta B} = 0, \tag{125}$$

d) $$\lim_{\Delta\mathbb{B}\to Q} \frac{\vec{F}_B}{\Delta B} = \rho_0 \vec{b}. \tag{126}$$

In this definition, ρ_0 is the mass density and $\rho_0\vec{b}$ is the body force per unit volume acting on Q.

Using the first Piola-Kirchhoff stress tensor $\boldsymbol{S}$ and the body force vector $\vec{b}$, the force acting on the free body is given by

$$F_i = \int_{\partial\mathbb{B}'} t_i(\vec{X},\vec{N},t)\,\mathrm{d}A + \int_{\mathbb{B}'} \rho_0(\vec{X}) b_i(\vec{X},t)\,\mathrm{d}V \tag{127}$$

$$= \int_{\partial\mathbb{B}'} N_J \cdot S_{Ji}(\vec{X},t)\,\mathrm{d}A + \int_{\mathbb{B}'} \rho_0(\vec{X}) b_i(\vec{X},t)\,\mathrm{d}V \tag{128}$$

$$= \int_{\mathbb{B}'} \left(\frac{\partial S_{Ji}}{\partial X_J} + \rho_0(\vec{X}) b_i(\vec{X}, t) \right) \mathrm{d}V. \tag{129}$$

With equation (129) Newton's second law can be generalized resulting in

$$\frac{\mathrm{d}}{\mathrm{d}t} \int_{\mathbb{B}'} \rho_0(\vec{X}) v_i \mathrm{d}V = \int_{\mathbb{B}'} \rho_0(\vec{X}) a_i \mathrm{d}V = \int_{\mathbb{B}'} \left(\frac{\partial S_{Ji}}{\partial X_J} + \rho_0(\vec{X}) b_i(\vec{X}, t) \right) \mathrm{d}V. \tag{130}$$

Since the choice of the free body $\mathbb{B}'$ was arbitrary, the local formulation also holds. The local formulation is given by

$$\frac{\partial S_{Ji}}{\partial X_J} + \rho_0(\vec{X}) b_i(\vec{X}, t) = \rho_0(\vec{X}) a_i. \tag{131}$$

Similarly, the total torque on the free body can be calculated. It is given by

$$M_i = \int_{\partial \mathbb{B}'} \epsilon_{ijk} x_j t_k(\vec{X}, \vec{N}, t) \mathrm{d}A + \int_{\mathbb{B}'} \epsilon_{ijk} x_j \rho_0(\vec{X}) b_k(\vec{X}, t) \mathrm{d}V \tag{132}$$

$$= \int_{\partial \mathbb{B}'} \epsilon_{ijk} x_j N_M S_{Mk}(\vec{X}, \vec{N}, t) \mathrm{d}A + \int_{\mathbb{B}'} \epsilon_{ijk} x_j \rho_0(\vec{X}) b_k(\vec{X}, t) \mathrm{d}V \tag{133}$$

$$= \int_{\mathbb{B}'} \frac{\partial}{\partial X_M} \left(\epsilon_{ijk} x_j S_{Mk}(\vec{X}, \vec{N}, t) \right) + \epsilon_{ijk} x_j \rho_0(\vec{X}) b_k(\vec{X}, t) \mathrm{d}V \tag{134}$$

$$= \int_{\mathbb{B}'} \epsilon_{ijk} \left[F_{jM} S_{Mk}(\vec{X}, \vec{N}, t) + x_j \left(\frac{\partial S_{Mk}}{\partial X_M} + \rho_0(\vec{X}) b_k(\vec{X}, t) \right) \right] \mathrm{d}V. \tag{135}$$

Equation (135) can now be used to generalize the angular equation of motion described by

$$\begin{aligned} \frac{\mathrm{d}}{\mathrm{d}t} \int_{\mathbb{B}'} \rho_0(\vec{X}) \epsilon_{ijk} x_j v_k \mathrm{d}V &= \int_{\mathbb{B}'} \rho_0(\vec{X}) \epsilon_{ijk} x_j a_k \mathrm{d}V \\ &= \int_{\mathbb{B}'} \epsilon_{ijk} \left[F_{jM} S_{Mk}(\vec{X}, \vec{N}, t) \right. \\ &\quad \left. + x_j \left(\frac{\partial S_{Mk}}{\partial X_M} + \rho_0(\vec{X}) b_k(\vec{X}, t) \right) \right] \mathrm{d}V. \end{aligned} \tag{136}$$

Together with equation (131) and (136), one obtains

$$\int_{\mathbb{B}'} \epsilon_{ijk} F_{jM} S_{Mk}(\vec{X}, \vec{N}, t) \mathrm{d}V = 0. \tag{137}$$

Since the choice of the free body was arbitrary, also the local angular equation of motion holds, which is given by

$$F_{jM}S_{Mk} = F_{kM}S_{Mj}. \tag{138}$$

The angular equation of motion (138) implies that the first Piola-Kirchhoff stress tensor is not symmetric. A symmetric tensor describing the stresses within a body is given by the second Piola-Kirchhoff stress tensor $\tilde{\boldsymbol{S}}$. It is defined by

$$\tilde{S}_{JM} = S_{Jk}F_{kM}^{-1}. \tag{139}$$

2.4.3 Linear Elastic Model

I introduced the notions to describe the strains and stresses inside a body in the upper two sections. However, to link stress and strain, assumptions about the material of the body must be made. For a linear elastic material, the generalization of Hook's law holds, which is given by [86]

$$\tilde{S}_{IJ} = C_{IJKL}E_{KL} \tag{140}$$

with

$$C_{IJKL} = \lambda\delta_{IJ}\delta_{KL} + \mu\left(\delta_{IK}\delta_{JL} + \delta_{IL}\delta_{JK}\right). \tag{141}$$

The constants μ and λ are called the Lamé parameters. In the following subsection, I will discuss two material parameters that are equivalent to the Lamé parameters, namely the Young's Modulus and the Poisson's Ratio.

Young's Modulus and Poisson's Ratio

Imagine a cuboid compressed by a load σ applied along the vertical direction (see *Figure* 12). According to equation (131) the first Piola-Kirchhoff stress tensor $\boldsymbol{S}$ must be of the form

$$S_{Ij} = \delta_{I3}\delta_{j3}\sigma, \tag{142}$$

According to equation (139) the second Piola-Kirchhoff stress tensor $\tilde{\boldsymbol{S}}$ is then given by

$$\tilde{S}_{IJ} = \delta_{I3}\delta_{J3}F_{33}^{-1}\sigma =: \delta_{I3}\delta_{J3}\tilde{S}. \tag{143}$$

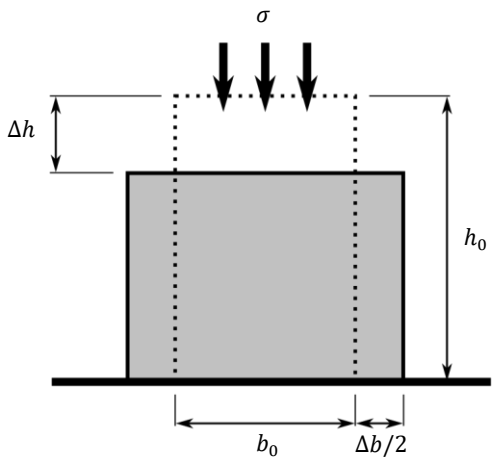

Figure 12. A cuboid with height h_0 and width b_0 is compressed by a vertical load σ by Δh and expands in the horizontal direction by Δb.

With the constitutive equation (141) the Lagrange strain tensor $\boldsymbol{E}$ can be calculated from the second Piola-Kirchhoff stress tensor. It is given by

$$E_{IJ} = E_I \delta_{IJ} \tag{144}$$

with

$$E_1 = E_2 = -\nu E_3, \tag{145}$$

$$E_3 = Y^{-1}\tilde{S}, \tag{146}$$

$$Y = \frac{\mu(3\lambda + 2\mu)}{\lambda + \mu}, \tag{147}$$

and

$$\nu = \frac{\lambda}{2(\lambda + \mu)}. \tag{148}$$

The resulting constant Y is called the Young's Modulus and the constant ν is called the Poisson's ratio ν. The Young's Modulus directly links the vertically applied stress with the resulting vertical component of the strain. The Poisson's ratio on the other hand links the resulting horizontal and vertical strain. A cuboid with a positive Poisson's ratio expands horizontally as a response to a vertical push. This is the behaviour common

materials show in our everyday life. However, also materials with a negative Poisson's ratio exist. There, the cuboid contracts horizontally as a response to a vertical push.

With formula (121) the displacement field $\vec{u}$ within the cube is given by

$$\vec{u} = \begin{pmatrix} \left(\sqrt{1+2E_3\nu}-1\right)X_1 \\ \left(\sqrt{1+2E_3\nu}-1\right)X_2 \\ \left(\sqrt{1+2E_3}-1\right)X_3 \end{pmatrix} \approx E_3 \begin{pmatrix} \nu X_1 \\ \nu X_2 \\ X_3 \end{pmatrix}. \tag{149}$$

For small strains E_3, the formula can be approximated as shown on the right-hand side of the equation.

From the displacement field of the cube, simple equations can be derived that allow to calculate the strain component E_3 and the Poisson's Ratio ν from the shape change of the cube after the compression in an experiment. According to equation (149) the displacement in the vertical direction can be expressed by

$$u_3(X_1, X_2, h_0) = \Delta h \approx h_0 E_3. \tag{150}$$

The value Δh is the change in height of the cube and h_0 is the initial height of the cube. It follows that the strain in the vertical direction is given by

$$E_3 \approx \frac{\Delta h}{h_0}. \tag{151}$$

In the horizontal direction, the displacement can be expressed equivalently by

$$u_2\left(X_1, \frac{b_0}{2}, X_3\right) = \frac{\Delta b}{2} \approx \nu \frac{b_0}{2} E_3. \tag{152}$$

The value Δb is the change in width of the cube and b_0 is the initial width of the cube. In total, it follows that the Poisson's ratio is given by

$$\nu \approx \frac{\Delta b}{b_0} \cdot \frac{h_0}{\Delta h}. \tag{153}$$

With this approximate formula, the Poisson's ratio can be calculated for small strains E_3.

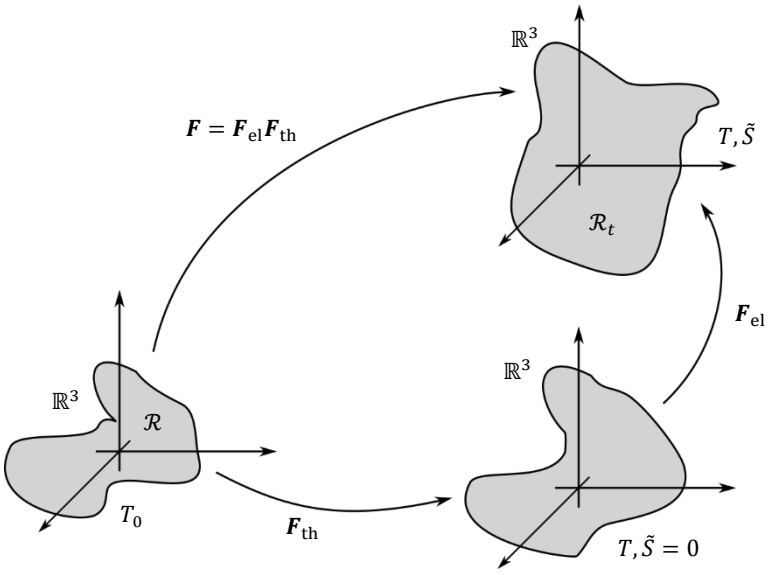

Figure 13. A body is at the temperature T_0 in the reference configuration $\mathcal{R}$. In the current configuration $\mathcal{R}_t$ at temperature T the body is deformed due to thermal expansion. This thermal expansion in combination with certain boundary conditions might induce stresses $\tilde{S} \neq 0$ inside the body. A third fictitious destressed configuration (bottom right) is used to decompose the deformation gradient in a pure thermal expansion and an elastic deformation.

2.4.4 Thermal Expansion

The liquid-crystal elastomers used in this thesis exhibit a large uniaxial thermal expansion. Large thermal expansions can be described via a multiplicative decomposition of the deformation gradient tensor [87]. The idea is that additionally to the reference configuration $\mathcal{R}$ at the temperature T_0 and the current configuration $\mathcal{R}_t$ at temperature T a third intermediate configuration at temperature T is added that is stress free. This intermediate configuration does in general not suffice the boundary conditions, however, it is helpful to solve the problem. The deformation gradient tensor $\boldsymbol{F}_{\mathrm{el}}$ connects the intermediate configuration with the current configuration, while the deformation gradient tensor $\boldsymbol{F}_{\mathrm{th}}$ connects the reference configuration with the intermediate configuration. Finally, the deformation gradient tensor $\boldsymbol{F}$ connecting the reference configuration with the current configuration is then given by the product of both tensors

$$\boldsymbol{F} = \boldsymbol{F}_{\mathrm{el}}\boldsymbol{F}_{\mathrm{th}}. \tag{154}$$

The tensor $\boldsymbol{F}_{\mathrm{th}}$ describes the thermal expansion free of any restrictions and can therefore be expressed by the equation for a uniaxial thermal expansion

$$\boldsymbol{F}_{\mathrm{th}} = (\Lambda_{\parallel} - \Lambda_{\perp})\vec{n}\vec{n}^{\mathrm{T}} + \Lambda_{\perp}\boldsymbol{I}. \tag{155}$$

The value $\Lambda_{\parallel}$ is the thermal stretch along the axis $\vec{n}$ and $\Lambda_{\perp}$ is the thermal stretch perpendicular to it. This concept is illustrated in *Figure* 13.

For every deformation gradient tensor, a corresponding Lagrange strain tensor can be defined by

$$\boldsymbol{E}_{\mathrm{th}} = \frac{1}{2}\left[\boldsymbol{F}_{\mathrm{th}}^{\mathrm{T}}\boldsymbol{F}_{\mathrm{th}} - \boldsymbol{I}\right], \tag{156}$$

$$\boldsymbol{E}_{\mathrm{el}} = \frac{1}{2}\left[\boldsymbol{F}_{\mathrm{el}}^{\mathrm{T}}\boldsymbol{F}_{\mathrm{el}} - \boldsymbol{I}\right] \tag{157}$$

and

$$\boldsymbol{E} = \frac{1}{2}[\boldsymbol{F}^{\mathrm{T}}\boldsymbol{F} - \boldsymbol{I}]. \tag{158}$$

Using equation (154), the Lagrange strain tensor $\boldsymbol{E}_{\mathrm{el}}$ can be expressed by the other two Lagrange strain tensors

$$\boldsymbol{E}_{\mathrm{el}} = \boldsymbol{F}_{\mathrm{th}}^{-\mathrm{T}}[\boldsymbol{E} - \boldsymbol{E}_{\mathrm{th}}]\boldsymbol{F}_{\mathrm{th}}. \tag{159}$$

In the following, I deduce a constitutive equation that connects the second Piola stress tensor $\widetilde{\boldsymbol{S}}$ with the Lagrange strain tensor $\boldsymbol{E}_{\mathrm{el}}$. For this, the temporal derivation of $\boldsymbol{E}_{\mathrm{el}}$ can be used. It is given by

$$\dot{\boldsymbol{E}}_{\mathrm{el}} = \boldsymbol{F}_{\mathrm{el}}^{\mathrm{T}}\dot{\boldsymbol{E}}\,\boldsymbol{F}_{\mathrm{el}}^{-1} - [(\alpha_{\parallel} - \alpha_{\perp})\vec{n}\vec{n}^{\mathrm{T}} + \alpha_{\perp}\boldsymbol{I}\,](1 + 2\boldsymbol{E}_{\mathrm{el}})\dot{T}. \tag{160}$$

The coefficients $\alpha = \frac{1}{\Lambda}\frac{\partial\Lambda}{\partial T}$ are the linear thermal expansion coefficients.

Due to the introduction of the intermediate configuration, it is possible to write the specific Helmholtz free energy f as a sum of an energy function $f_e(\boldsymbol{E}_{\mathrm{el}}, T)$ describing an isothermal linear elastic process at temperature T and an energy function $f_{\mathrm{T}}(T)$ describing a heating process that contains no elastic contributions [87]. In total the free energy is given by [87]

$$f = f_e(\boldsymbol{E}_{\mathrm{el}}, T) + f_{\mathrm{T}}(T) \tag{161}$$

with $$\rho_{\mathrm{T}} f_{\mathrm{e}}(\boldsymbol{E}_{\mathrm{el}}, T) = C_{ijkl}(E_{\mathrm{th}})_{ij}(E_{\mathrm{th}})_{kl}. \tag{162}$$

The value ρ_T is the density of the material in the intermediate configuration and $\boldsymbol{C}$ is the stiffness tensor. Now, the temporal derivation of the specific Helmholtz free energy is given by

$$\dot{f} = \frac{\partial f_{\mathrm{e}}}{\partial \boldsymbol{E}_{\mathrm{th}}} : \dot{\boldsymbol{E}}_{\mathrm{th}} + \frac{\partial f_{\mathrm{e}}}{\partial T}\dot{T} + \frac{df_{\mathrm{T}}}{dT}\dot{T}. \tag{163}$$

Inserting equation (160) leads to

$$\dot{f} = \boldsymbol{F}_{\mathrm{el}}^{-1}\frac{\partial f_{\mathrm{e}}}{\partial \boldsymbol{E}_{\mathrm{el}}}\boldsymbol{F}_{\mathrm{el}}^{-\mathrm{T}} : \dot{\boldsymbol{E}} - \frac{\partial f_{\mathrm{e}}}{\partial \boldsymbol{E}_{\mathrm{el}}} : [(\alpha_{\parallel} - \alpha_{\perp})\vec{n}\vec{n}^{\mathrm{T}} + \alpha_{\perp}\boldsymbol{I}](1 + 2\boldsymbol{E}_{\mathrm{el}})\dot{T} + \\ + \frac{\partial f_{\mathrm{e}}}{\partial T}\dot{T} + \frac{df_{\mathrm{T}}}{dT}\dot{T}. \tag{164}$$

At the same time $\dot{f}$ is given by [87]

$$\dot{f} = \frac{1}{\rho_0}\widetilde{\boldsymbol{S}} : \dot{\boldsymbol{E}} - s\dot{T}. \tag{165}$$

A comparison of coefficients leads to the final constitutive equation including thermal expansion

$$\widetilde{\boldsymbol{S}} = \det(\boldsymbol{F}_{\mathrm{th}})\,\boldsymbol{F}_{\mathrm{th}}^{-1}(\boldsymbol{C} : \boldsymbol{E}_{\mathrm{el}})\boldsymbol{F}_{\mathrm{th}}^{-\mathrm{T}}. \tag{166}$$

I use this equation in chapter 4 to model the thermal expansion of liquid-crystal elastomers.

3 Chapter 3
3D Printing of Liquid-Crystal Elastomers

3D printing of liquid-crystal elastomers allows to create 3D structures with a spatially varying director field. An example of a printed 3D structure with an inhomogeneous director field is shown in *Figure 14*. The scanning electron micrograph shown in *Figure 14c* depicts the 3D geometry of the structure, which consists of a central post with eight arms attached to it. Each arm is built from two connected layers with different director orientations. The director within the arms is indicated in the top view drawing presented in *Figure 14a*. One layer of each arm has a director tangential to the arm and the other layer has a director pointing out of the plane. Due to the anisotropic thermal expansion of the liquid-crystal elastomer, the arms bend significantly on heating. This bending motion is depicted in *Figure 14b* for different temperatures of the structure. The bi-layered beam bending motion is the fundamental mechanism that is exploited in this work to design 3D structures that change their shape on an external stimulus such as heat or light.

This chapter describes the 3D laser microprinting technique I developed to print 3D microstructures with nearly arbitrary orientation of the director at every point in space. First, the general printing principle is outlined followed by all crucial parts such as the employed liquid-crystal resins, the director alignment mechanism and how to focus the printing laser within the birefringent resin. At the end of the chapter, I present printed test structures that proof the control over the director during printing of the samples.

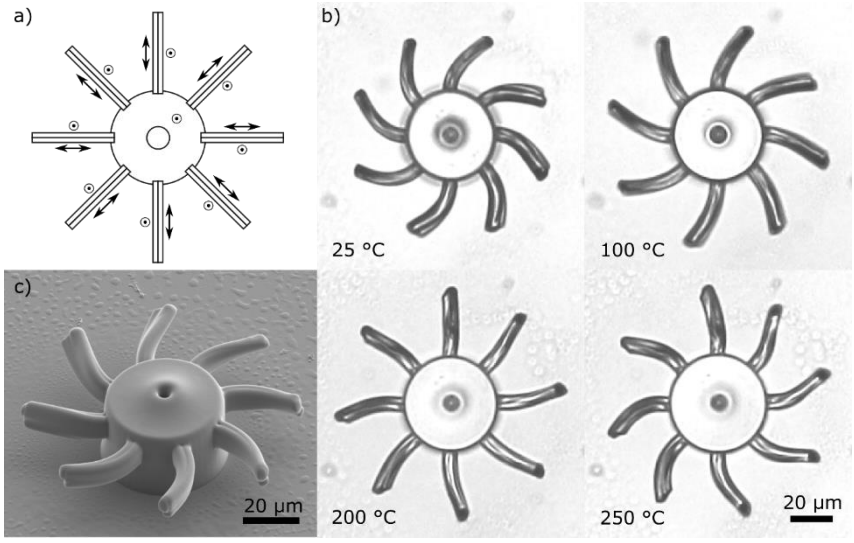

Figure 14. Liquid-crystal elastomer 3D structure with an inhomogeneous director profile. (a) The arrows in the drawing of the printed geometry indicate the intended director profile. (b) The optical microscope images show a large bending motion of the eight arms in the counter-clockwise direction for increasing temperatures. (c) Scanning electron micrograph of the structure. Figure taken from [88] (CC BY 4.0).

3.1 Printing principle

The 3D printing technique described here is based on common 3D laser microprinting. In 3D laser microprinting, a femto-second pulsed laser is focused into a liquid photo-resin. In the laser focus, a two-photon-absorption induced polymerization reaction starts that locally solidifies a volume called 'voxel'. By scanning the laser focus in the photoresin, nearly arbitrary 3D structures can be formed out of the resin. In the end, the remaining liquid resin is washed away by a suitable solvent and one ends up with a 3D printed microstructure.

Figure 15a shows a sketch of common 3D laser microprinting. An objective lens focusses a femto-second pulsed laser into a droplet of a photo-resin located on a glass substrate where the microstructure is printed on. By scanning the laser with galvanometric mirrors, a slice of a structure can be polymerized on top of the substrate as depicted in *Figure 15b*. After this slice, the substrate is moved one step away from the objective lens, allowing to print another slice on top of the existing slice by scanning the laser, as

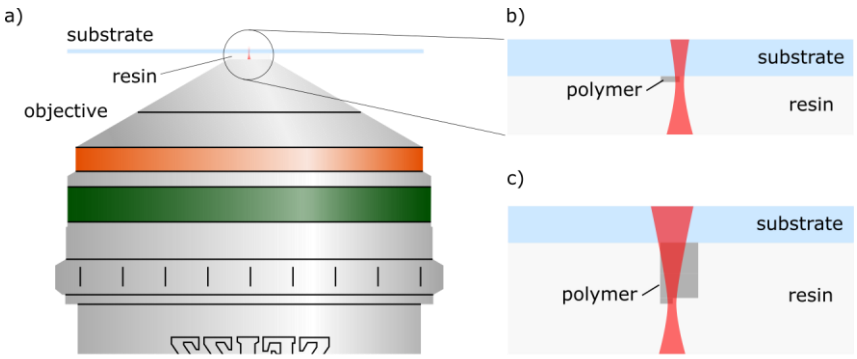

Figure 15. Illustration of common 3D laser microprinting. (a) An objective lens focusses a femto-second pulsed laser beam into a resin located on a glass substrate. (b) A zoom-in at the position of the laser focus shows, that a polymerization reaction occurs at the laser focus (red, numerical aperture not to scale). By scanning the laser focus via galvanometric mirrors, a slice can be polymerized on top of the glass substrate. (c) Retracting the substrate from the objective lens, further slices can be polymerized on top of the existing slices. With that strategy structures of nearly arbitrary size and shape can be printed.

shown in *Figure 15c*. This strategy allows in principle to print structures of arbitrary height.

To print liquid-crystal elastomers, an additional mechanism to control the director during printing is required. In this work, the director is aligned by a variable electric field, which in turn is induced by a custom-made electrode. The two-sided indium tin oxide (ITO) electrode is placed between the objective lens and the substrate as illustrated in *Figure 16*. The substrate itself is now covered with ITO on the backside and acts as a counter electrode. In combination, the electrode and the substrate allow to induce arbitrarily oriented electric fields within a liquid-crystal resin located in between the electrode and the substrate.

As described in the fundamentals chapter, the liquid-crystal director aligns parallel to the induced electric fields. The following polymerization of the liquid-crystal resin fixes the liquid-crystal elastomers director to the orientation of the electric field [58]. In a further step, the electric field can be oriented in another direction allowing to print liquid-crystal elastomer with another director orientation, while the already printed liquid-crystal elastomer keeps its director orientation.

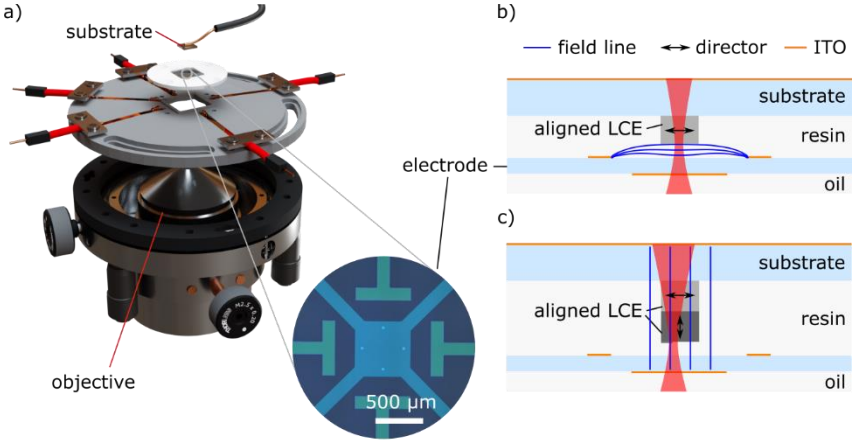

Figure 16. Illustration of the technique established to 3D print liquid-crystal elastomers with control over the spatial director field. (a) The objective lens is enclosed by a mount that positions a transparent electrode closely above the front lens of the objective. (see Figure 23 for a detailed description). The inset depicts a top-view optical microscope image of the electrode. It shows patterns of indium tin oxide (ITO) on the front- and backside of the electrode. The patterns appearing in green are on the front of the electrode, while the pattern that appears light-blue points towards the objective lens. (b) A zoom-in drawing at the position of the laser focus (red, numerical aperture not to scale). The gap between the objective lens and the electrode is filled with immersion oil, while the gap between the electrode and the substrate is filled with a liquid-crystal resin. The substrate itself is coated with indium tin oxide on its backside. In the depicted configuration, a horizontal electric field is applied via the electrode, aligning the director of the resin in the focal plane along the horizontal direction. In the focus of the laser, the polymerization reaction forms a liquid-crystal elastomer with a permanently fixed horizontal director orientation. (c) Changing to a vertical electric field reorients the director within the resin but not within the polymerized material. Thereafter, another part of the structure can be printed with a vertical director orientation, leaving the director of the already printed structure unaffected. During printing, the electrode position is fixed, whereas the substrate is moves freely. This allows for structures of nearly arbitrary height. Figure adapted from [88] (CC BY 4.0).

One could, for example, apply a horizontal electric field to print a block of liquid-crystal elastomer with a horizontal director orientation as depicted in *Figure 16b*. In a second step, one could apply a vertical electric field to print another block of liquid-crystal elastomer on top with a vertical director orientation, as shown in *Figure 16c*. After development of the structure, one ends up with a block of liquid-crystal elastomer with a

director horizontal to the substrate on the bottom and a director vertical to the substrate on top.

Since the electrode is fixed at a certain distance to the objective lens and since the substrate is free to move, one can in principle print structures of arbitrary footprint and height. The limitations in height are governed by the range of the stage and the maximum available voltage.

Three aspects are crucial for this printing technique to work. First, it is required to induce sufficiently homogeneous and sufficiently strong electric fields within the resin. Second, the femto-second laser beam must be properly focused into the highly birefringent liquid-crystal resin. Third, the liquid-crystal resin has to be nematic and liquid at room temperature. These three aspects are discussed in the following.

3.2 Inducing Electric Fields in the Liquid-Crystal Resin

In this section, the electrode design I developed is presented in detail, along with finite element calculations I performed to verify that the electrode can induce sufficiently homogeneous electric fields within the liquid-crystal resin. Furthermore, the electrode fabrication is discussed followed by a discussion of the electrode driver and a discussion about the alignment of the electrode in the actual setup.

3.2.1 Electrode Design

The electrode is fabricated on a $13\ \mathrm{mm} \times 13\ \mathrm{mm} \times 0.17\ \mathrm{mm}$ glass (D263M) coverslip by coating a layer of patterned indium tin oxide on the front- and the backside. A light microscope image of an electrode is shown in the inset of *Figure 16a*. The front pattern, which appears green, consists of four separate pads. The back pattern, which appears blue, consists of one larger pad.

A 3D sketch of the electrode together with the substrate is displayed in *Figure 17a*. There, the substrate is located at a variable distance h above the electrode. To prevent a large voltage drop over the substrate, it is made of c-plane sapphire for its high permittivity. The substrate has a thickness of $430\ \mu\mathrm{m}$. The printing area, *i.e.* the area where the focus of the printing laser is scanned is marked in red. It is located $100\ \mu\mathrm{m}$ above the surface of the electrode and has a square shape with a width of $150\ \mu\mathrm{m}$. The electrode is designed to assert sufficiently homogenous electric fields within in the printing area.

To verify the homogeneity of the electric field within the printing area, one first needs to calculate the electric field distribution, for which the Poisson's equation must be

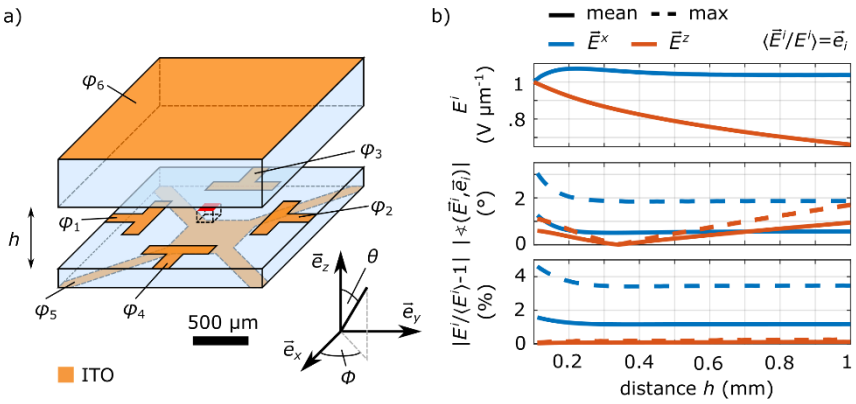

Figure 17. (a) 3D schematic of the electrode geometry used for the finite element calculations. The sketch shows the patterned electrode and the sapphire substrate located at a distance h above the electrode. The electrostatic potential applied to pad i is labelled φ_i with $i = 1 \ldots 6$. The printing area is located $100\ \mu m$ above the electrode and is marked in red. (b) Results of finite element calculations characterizing the electric fields $\vec{E}^x, \vec{E}^y$ in the printing are for two different sets of potentials φ_i^x, φ_i^z. The superscripts denote the average direction of the resulting electric fields. The top panel shows the average magnitude of the respective electric fields for different h. The central panel depicts the maximum and the mean angular electric-field deviation with respect to its mean direction within the printing area. The bottom panel shows the mean and maximum magnitude electric-field deviation with respect to the mean electric-field magnitude within the printing area. Figure adapted from [88] (CC BY 4.0).

solved for the geometry depicted in ***Figure 17a***. The potential at the electrode pad i is given by φ_i with $i = 1 \ldots 6$ as depicted in ***Figure 17a***. As a simplification of the problem, I assumed that the director of the liquid-crystal resin always aligns parallel to the electric field. The assumption of parallel electric field and director is justified in section 2.1.2. To obtain a solution to the described problem, I employed a finite element approach using COMSOL Multiphysics.

Choosing two different sets φ_i^x and φ_i^z, I solved the problem for different distances h between the substrate and the electrode ranging from $100\ \mu\mathrm{m}$ to $1\ \mathrm{mm}$. Here, the superscript denotes the mean direction of the electric field in the printing area.

$$\varphi_1^x = \varphi_2^x = \varphi_5^x = \varphi_6^x = U^x, \varphi_3^x = 0\ \mathrm{V}, \varphi_4^x = 2U^x, \qquad U^x = 1428.6\ \mathrm{V} \tag{167}$$

$$\varphi_1^z = \varphi_2^z = \varphi_3^z = \varphi_4^z = U^z, \varphi_5^z = 0\ \mathrm{V}, \varphi_6^z = 3U^z, \qquad U^z = 504.4\ \mathrm{V} \tag{168}$$

Assuming permittivities of $\epsilon^{\mathrm{LC}} = 19$ for the liquid-crystal resin, $\epsilon_{\parallel}^{\mathrm{S}} = 11.54$, $\epsilon_{\perp}^{\mathrm{S}} = 9.34$ for the sapphire substrate and $\epsilon^{\mathrm{E}} = 4.6$ for the electrode, I obtained a solution for the electric field-distribution, which is plotted in *Figure 17b* and *Figure 18*.

In the top panel of *Figure 17b* the average field strength is displayed for distances h ranging from $100\ \mu\mathrm{m}$ to $1\ \mathrm{mm}$. The field strength for fields in the x – direction depends only weakly on h. This is intuitively clear, since the relevant distance between pads 3 and 4 is independent of h. On the other hand, the field strength for fields in the z – direction decrease monotonously with growing h. This is also intuitive, since the relevant distance between the pads 5 and 6 directly depends on h.

The modulus of the deviation of the field strength to the mean field strength within the printing area is plotted in *Figure 18b*, while the mean value and the maximum value of this quantity within the printing area are plotted in the bottom panel of *Figure 17b*. For the fields in the x – direction, the field strength increases towards the electrode pads 3 and 4, which is characteristic for a stray field. The maximum deviation from the mean field strength is below $4.6\ \%$ and the mean deviation below $2\ \%$ for all distances h below $1\ \mathrm{mm}$. For the fields in the z – direction, the maximum and mean deviations are well below $0.5\ \%$ and result from the finite size of pad 5.

The mean direction of the electric field is as desired for both sets of potentials and all distances h. The deviation to the desired direction within the printing area is plotted in *Figure 18a* for different distances h. The mean and the maximum deviation within the printing area are plotted in the central panel of *Figure 17b*.

For fields in the x – direction, the angular deviation is zero along the y – axis starting from the centre of the printing area, which results from the mirror symmetry of the electrode. The deviations get stronger following the x – axis starting from the centre of the printing area. This is also expected, since it is a stray field and the field vectors start to tilt towards the substrate leaving the centre of the electrode. The deviation is strongest in the corners of the printing area due to the finite size of the electrode pads 3 and 4. The maximum angular deviations are below $3°$ and the mean deviations are below $1.5°$ for all considered distances h. For small separation distances h, the substrate has an adverse influence on the homogeneity of the field direction. However, the angular deviations decrease quickly for larger separation distances. Alternatively, the deviations

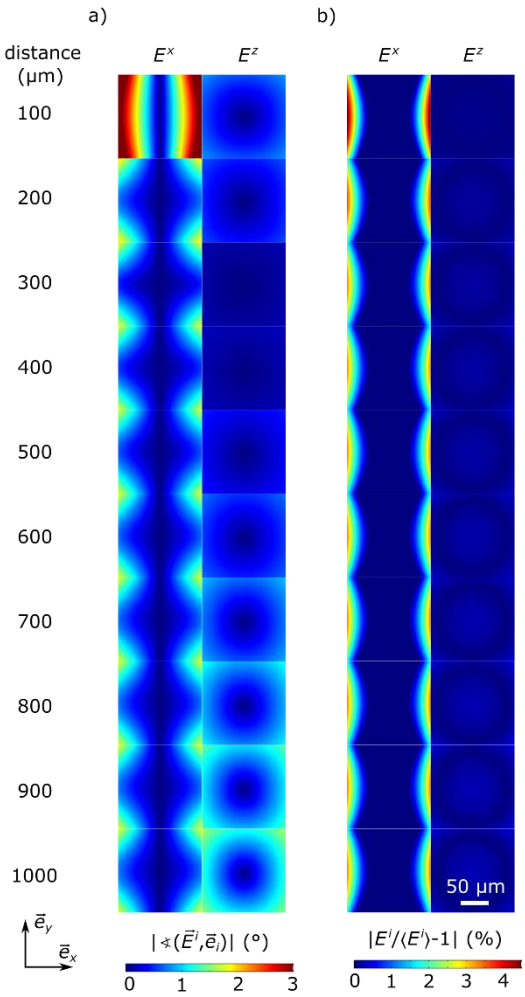

Figure 18. Homogeneity of the electric field within the printing area for different distances between the electrode and the substrate resulting from finite element calculations. (a) Angle between the electric field vector and the average field direction within the printing area. (b) Deviation in magnitude of the electric field compared to the average magnitude of the electric field within the printing area. Figure taken from [88] (CC BY 4.0).

would also decrease for a larger distance between the electrode pads 3 and 4. However, then, the field strength would decrease for a fixed set of potentials. For fields in the z – direction, the angular deviation in angle is zero in the centre of the printing area, which is due to the fourfold rotational symmetry of the electrode. Due to the finite size of pad 5, the deviations increase towards the boundaries of the printing area. This could in principle be compensated with a suitable set of potentials φ_1 - φ_4 for every distance h. However, I fixed the potentials for simplicity. For my choice of potentials, there is no deviation at a distance of about $340\ \mu\mathrm{m}$. The maximum deviation is below $2°$ and the mean deviation is below $1°$ for all distances h below $1\ \mathrm{mm}$.

Overall, I consider the fields to be sufficiently homogeneous for both configurations. Since the electrode has a four-fold rotational symmetry, the same considerations hold for fields in the y – direction that are obtained by a set of potentials φ_i^y.

$$\varphi_3^y = \varphi_4^y = \varphi_5^y = \varphi_6^y = U^x, \varphi_1^y = 0\ \mathrm{V}, \varphi_2^y = 2U^x \tag{169}$$

Due to the principle of superposition, it is not only possible to apply fields along the principal axes, but in all other directions. The potentials to apply for a desired field with field strength E in the direction (ϕ, θ) for a certain distance h are given by

$$\begin{aligned}\varphi_i(E, \phi, \theta, h) = \frac{E}{E^x(h)}\left[\cos\phi \sin\theta\, \varphi_i^x + \sin\phi \sin\theta\, \varphi_i^y\right] \\ + \frac{E}{E^z(h)} \cos\theta\, \varphi_i^z + \varphi_0, \qquad i = 1 \ldots 6.\end{aligned} \tag{170}$$

Here, φ_0 is a constant potential that can be added to shift the resulting potentials to reasonable values.

To validate the performance of the electrode experimentally, I assembled an electrode and a substrate spaced by $h = 100\ \mu\mathrm{m}$ with two layers of scotch tape and infiltrated the assembly with E7 liquid-crystal mixture. I observed the assembly in between two crossed polarizers in an optical bright-field microscope. The motivation for this configuration is that the E7 mixture is birefringent with an optic axis coinciding with the director. This means that the resulting images are black whenever the director is perpendicular or parallel to one of the polarizers. This means, that the observed dark areas are an indicator, whether the electrode aligns the liquid crystal in the desired direction or not.

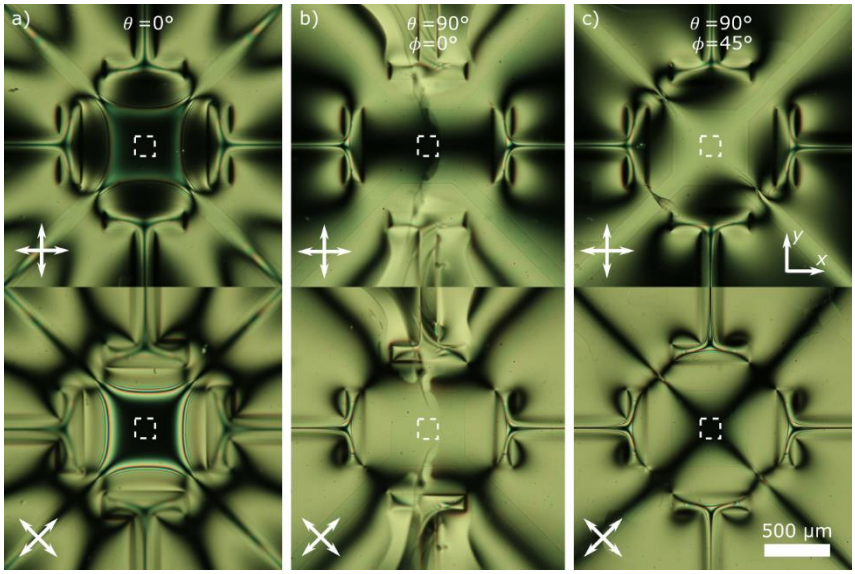

Figure 19. Optical microscope image of an electrode and a substrate at a distance of $h = 100\ \mu m$ infiltrated with E7 liquid-crystal mixture. The assembly is placed in between crossed polarizers (indicated by the crossed arrows at the bottom left) and illuminated in transmission. The image appears black, whenever the director of the E7 mixture is perpendicular or parallel to one of the polarizers. The orientation of the polarizers is indicated by the white arrows. The printing area is marked with a dotted square in the centre of the electrode. Three different field configurations are observed. (a) Field is applied perpendicular to xy – plane. (b) Field is applied in x – direction. (c) Field is applied in the xy – plane rotated by 45° with respect to the x – axis.

In the experiment, I examined three different configurations of the electric field, as displayed in *Figure 19*, comprising a field perpendicular to the substrate and two fields parallel to the substrate being rotated by $45°$ with respect to each other. For the first configuration, the printing area appears black for both configurations of the polarizers. This proves, that the director is perpendicular to the substrate as desired. For the other two configurations, the printing area appears black, whenever one of the polarizers is parallel to the desired direction of the director. On the other hand, the printing area appears bright if the desired director is not parallel or perpendicular to one of the polarizers. These observations agree with the desired director orientation. In conclusion, these observations are first indications that the electrode works as desired. A more

rigorous proof that the director of printed objects coincides with the desired direction is given in section 3.6.1.

Besides a homogenous field distribution, the electrode must also have a sufficiently low capacity C_{ij} between two pads i and j, as I will point out in the next section. Using the above presented finite-element method, I compute the following capacitances:

$$C_{ij} \approx \begin{pmatrix} - & 0 & 0 & 0 & 0 & 0.5 \\ 0 & - & 0 & 0 & 0 & 0.5 \\ 0 & 0 & - & 0 & 0 & 0.5 \\ 0 & 0 & 0 & - & 0 & 0.5 \\ 0 & 0 & 0 & 0 & - & 1.5 \\ 0.5 & 0.5 & 0.5 & 0.5 & 1.5 & - \end{pmatrix} \text{pF}. \tag{171}$$

3.2.2 Driving the Electrode

In order to prevent breakdowns and deteriorations of the resin and the electrodes, it is important to drive the electrode with an AC voltage instead of an DC voltage [89]. Within this work, I chose a frequency of $800\ \text{Hz}$, which proved to be sufficient to prevent breakdowns and deteriorations even during printing jobs taking more than 15 hours. To obtain electric fields with a strength on the order of $1\ \text{V}\ \mu\text{m}^{-1}$, it is necessary to provide six potentials φ_i with independent amplitude up to $3\ \text{kV}$ at the same phase. Conceptually, it would be the easiest to use six high voltage amplifiers with six synchronized function generators. However, amplifiers that provide voltages of about $3\ \text{kV}$ at frequencies of $800\ \text{Hz}$ are expensive. Therefore, I decided to use a system consisting of one amplifier, one computer-controlled function generator and a set of six computer-controlled variable voltage dividers that are connected in parallel to the amplifier.

A circuit diagram of such a voltage divider is shown in *Figure 20a*. The voltage divider consists of a fixed capacitor $\tilde{C}_i$ and a variable capacitor C_i. The voltage divider is built from capacitors instead of resistors, since it is complicated to obtain variable resistors with a sufficiently long lifetime. The output signal φ_i of a single voltage divider is related to the input signal φ by the equation (1) and can therefore be adjusted by the variable capacitor C_i.

$$\varphi_i = \frac{\tilde{C}_i}{C_i + \tilde{C}_i}\varphi \tag{172}$$

A reed relay is employed to set the output potential φ_i to GND if necessary. Additionally, a second voltage divider is connected in parallel and provides a probe signal

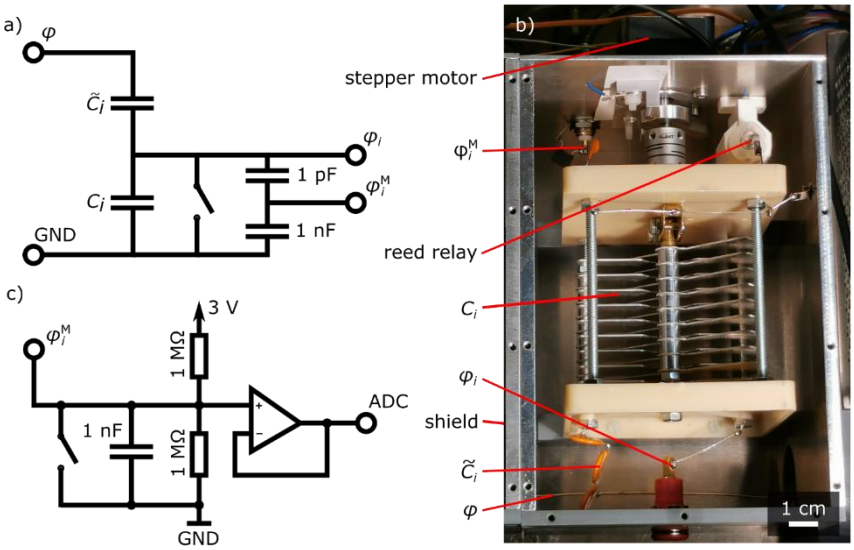

Figure 20. (a) Circuit diagram of a voltage divider used to drive the electrode. Here, φ labels the output of the amplifier, while φ_i labels the output of the voltage divider. The voltage divider consists of a tuneable capacitor C_i and a fixed capacitor $\tilde{C}_i$. A second voltage divider is used to supply a signal φ_i^M that is proportional to φ_i and can be measured easily. A switch is used to put the output of the voltage divider to ground (GND) if necessary. (b) A photograph of a voltage divider used in the actual setup. The rotary plate capacitor C_i is clearly visible. Shields are necessary to prevent electromagnetic coupling of the voltage dividers. (c) Diagram of the circuit used to measure the signal φ_i^M supplied by the voltage dividers. It is important to measure one voltage divider after the other and put the remaining measurement outputs to GND to not introduce couplings between the voltage dividers. Figure adapted from [88] (CC BY 4.0).

$\varphi_i^M = m\varphi_i$ that is in the range of ± 3 V and proportional to φ_i. I used the circuit shown in *Figure 20c* to automatically measure the probe signal. To obtain the proportionality factor m, I connected the output φ_i of each voltage divider directly with the input φ and measured $\varphi_i^{\mathrm{M}} = m\varphi$ for different φ. From the resulting data, I extracted m by a linear fit (not shown) and thereby calibrated the measurement.

The voltage dividers are connected to a HiVolt HA51U-3B2 amplifier which is specified to a maximum load of $166\ \mathrm{pF}$ at a frequency of $800\ \mathrm{Hz}$ and an output amplitude of $3\ \mathrm{kV}$. Therefore, the capacitors used in the voltage dividers must be in the range of several tens of pico-farads. For the fixed capacitors I chose $\tilde{C}_{i\neq 6} = 33.3\ \mathrm{pF}$ and $\tilde{C}_6 =$

$50\ \mathrm{pF}$ with $i = 1 \dots 6$ and for the variable capacitor I chose an Amidon rotary plate capacitor with a specified range of $C_i(\alpha) = 6 - 130\ \mathrm{pF}$. The position α of the plate capacitor is controlled by a stepper motor and ranges from $0°$ to $180°$. The arrangement of the components is depicted in *Figure 20b*.

The components of each voltage divider are located in a separate shielded container, which is important since the coupling capacity C_{ij} between two voltage dividers i and j can easily reach several picofarads. This has to be avoided, since high coupling capacities limit the system. The higher the coupling, the less independent is the choice of output signals. In the extreme case of an infinite coupling capacity, all output signals are the same. For the same reason, the electrode is connected to the voltage divider via shielded cables. Since commercially available shielded cables typically have a too large capacity for the system to work, I custom built coaxially-shielded cables with an outer diameter of $2\ \mathrm{cm}$ and a length of $40\ \mathrm{cm}$. However, due to the coupling capacities C_{ij} of the electrode itself on the order of $1\ \mathrm{pF}$, the voltage dividers must still be treated as a coupled system.

Due to the coupling of the voltage dividers by the electrode itself, it is not possible to estimate the required configurations of the variable capacitors for a desired set of output potentials φ_i by equation (172). Actually, the more complicated equation

$$r_i = \frac{\varphi - \varphi_i}{\varphi_i} + \sum_{j=1}^{6} \frac{\varphi_j - \varphi_i}{\varphi_i} r_{ij} \tag{173}$$

has to be used. Here, r_i and r_{ij} denote ratios of the capacities C_i and C_{ij} relative to the fixed capacitors $\tilde{C}_i$ defined by

$$r_i(\alpha) \coloneqq \frac{C_i(\alpha)}{\tilde{C}_i}, r_{ij} \coloneqq \frac{C_{ij}}{\tilde{C}_i}, \qquad i, j = 1 \dots 6. \tag{174}$$

In general, equation (173) will not lead to values r_i that can be reached by the rotary plate capacitor. However, it is possible to shift all potentials φ_i by a common value φ_0 and scale the potentials by a common factor n to obtain an electric field with at least the desired direction but possibly a smaller magnitude. The problem is to find a potential φ_0 such that n and therefore the magnitude if the resulting electric field is as large as possible. I start by replacing φ_i with $n(\varphi_i - \varphi_0)$ in equation (173) to obtain

$$\frac{\varphi' + \varphi_0 + a_i}{\varphi_i - \varphi_0} = r_i \tag{175}$$

with $$\varphi' \coloneqq \frac{\varphi}{n}, \tag{176}$$

$$a_i \coloneqq \sum_j (\varphi_j - \varphi_i) r_{ij} - \varphi_i. \tag{177}$$

Since r_i is restricted by $r_i^{\min} \leq r_i \leq r_i^{\max}$, it follows from equation (175) and the assumption $\varphi_i \geq \varphi_0$ that:

$$r_i^{\min}(\varphi_i - \varphi_0) - a_i - \varphi_0 \leq \varphi' \leq r_i^{\max}(\varphi_i - \varphi_0) - a_i - \varphi_0, \quad i = 1 \dots 6 \tag{178}$$

$$\Rightarrow \quad r_i^{\min}(\varphi_i - \varphi_0) - a_i - \varphi_0 \leq r_j^{\max}(\varphi_j - \varphi_0) - a_j - \varphi_0, \quad i,j = 1 \dots 6 \tag{179}$$

$$\Rightarrow \quad A_{ij} \leq B_{ij}\varphi_0 \tag{180}$$

with $$A_{ij} = r_i^{\min}\varphi_i - r_j^{\max}\varphi_j - a_i + a_j \tag{181}$$

$$B_{ij} = r_i^{\min} - r_j^{\max}. \tag{182}$$

In the setup described above, it is $B_{ij} < 0$ for $i,j = 1 \dots 6$, and therefore $\varphi_0 \leq A_{ij}/B_{ij}$ for $i,j = 1 \dots 6$. To maximize n, I choose

$$\varphi_0 = \min_{i,j} \frac{A_{ij}}{B_{ij}}. \tag{183}$$

The smallest possible value for φ' is then according to equation (178) given by

$$\varphi' = \max_i \left(r_i^{\min}(\varphi_i - \varphi_0) - a_i - \varphi_0 \right), \tag{184}$$

which results in the maximum value $n_{\max}$

$$n_{\max} = \frac{\varphi}{\max_i \left(r_i^{\min}(\varphi_i - \varphi_0) - a_i - \varphi_0 \right)}. \tag{185}$$

Plugging the results of equation (183) and (184) in equation (175) results in the configurations of the variable capacitors necessary to obtain an electric field pointing in the direction of the field described by the set of potentials φ_i. The largest possible field strength for each direction is displayed in the false-colour plot in *Figure 21*. The connection between the centre of the coordinate system and a point on the shown sphere

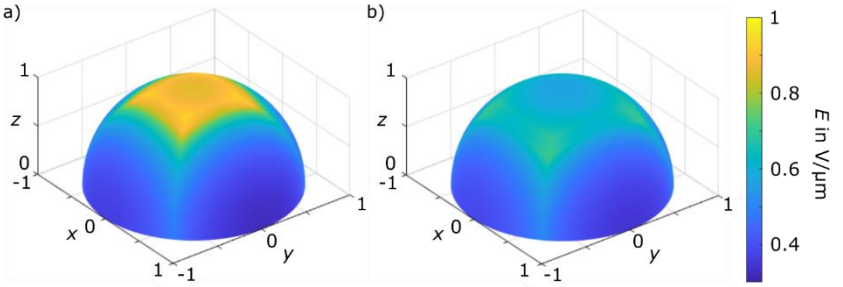

Figure 21. Available electric field strengths in the presented setup. The connection between the centre of the normalized coordinate system and a point on the sphere encodes the direction of the electric field and the colour of the sphere at that point encodes the larges possible field strength. The calculation is based on equation (185) and the results of the finite element calculations presented in the top panel of Figure 17b. (a) $h = 100\ \mu m$. (b) $h = 1\ mm$.

encodes the direction of the electric field and the colour of the sphere at that point encodes the larges possible field strength. *Figure 21a* assumes a distance $h = 100\ \mu\text{m}$ between the electrode and the substrate and *Figure 21b* assumes a distance of $h = 1\ \text{mm}$. The available fields strengths are always above $0.3\ \text{V}\ \mu\text{m}^{-1}$ for all configurations and separation distances $h \leq 1\ \text{mm}$.

Using equation (175) to calculate the configuration of the rotary plate capacitors requires knowledge about the boundaries $r_i^{\min}$ and $r_i^{\max}$ and the coupling capacities r_{ij}. Additionally, the relation $r_i(\alpha)$ is needed to set the estimated configuration with the stepper motor connected to the rotary plate capacitor. With the electronics presented here, it is possible to measure these quantities in the assembled setup without large effort. It is only necessary to measure the output potential φ_i in different configurations. For these measurements, it is important to only measure at one measurement port at a time and set the other measurement ports to ground (GND) to suppress further couplings of the voltage dividers. A detailed description of the algorithm is provided in the following.

The measurement of the capacities in the setup is a two-step process. In a first step, set $\varphi_j = 0$ for $j \neq i$ and measure $\tilde{r}_i(\alpha_i) = (\varphi - \varphi_i)/\varphi_i$ for different configurations α_i of the rotary plate capacitor C_i. In a second step, set $\varphi_j = \varphi$ for $j \neq i$ and $\varphi_k = 0$ for $k \neq i, j$ and measure $\tilde{r}_{ij}(\alpha_i) = (\varphi - \varphi_i)/\varphi_i$ for the same configurations α_i of the rotary plate capacitor i. The idea behind this measurement is that in the first step all coupling capacities lie in parallel to the rotary plate capacitor C_i. In the second step, C_{ij} is parallel

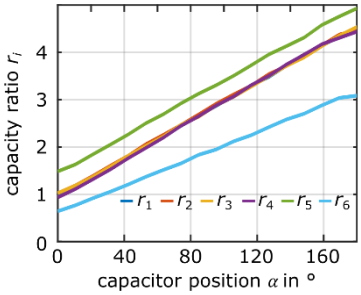

Figure 22. Capacity ratio r_i versus the capacitor position α for the six voltage dividers connected to an assembled electrode and a substrate with a liquid-crystal resin applied in between.

to $\tilde{C}_i$ and the remaining coupling capacities remain parallel to C_i. This leads to the following set of equations:

$$\tilde{r}_i(\alpha_i) = \frac{C_i(\alpha_i) + \sum_{j\neq i} C_{ij}}{\tilde{C}_i} \tag{186}$$

and

$$\tilde{r}_{ij}(\alpha_i) = \frac{C_i(\alpha_i) + \sum_{k\neq i,j} C_{ik}}{\tilde{C}_i + C_{ij}}. \tag{187}$$

This set of equations can be solved for the desired quantities $r_i(\alpha_i)$ and r_{ij}:

$$r_{ij} = \frac{C_{ij}}{\tilde{C}_i} = \frac{\tilde{r}_i - \tilde{r}_{ij}}{1 + \tilde{r}_{ij}} \tag{188}$$

and

$$r_i(\alpha_i) = \frac{C_i(\alpha_i)}{\tilde{C}_i} = \tilde{r}_i(\alpha_i) - \sum_{j\neq i} r_{ij}. \tag{189}$$

The boundaries $r_i^{\min}$ and $r_i^{\max}$ can be directly derived as the minimum and maximum of $r_i(\alpha_i)$.The following values represent a typical measurement for a distance of $h = 100\ \mu\text{m}$ between the electrode and the substrate:

$$r_i^{\min} = \begin{pmatrix} 1.01 \\ 1.02 \\ 1.03 \\ 0.93 \\ 1.48 \\ 0.64 \end{pmatrix}, r_i^{\max} = \begin{pmatrix} 4.52 \\ 4.47 \\ 4.54 \\ 4.44 \\ 4.93 \\ 3.09 \end{pmatrix}, r_{ij} = \begin{pmatrix} - & 0 & 0.01 & 0.01 & 0.03 & 0.03 \\ 0.01 & - & 0.01 & 0.01 & 0.04 & 0.02 \\ 0.01 & 0 & - & 0.01 & 0.03 & 0.01 \\ 0.01 & 0 & 0.01 & - & 0.03 & 0.02 \\ 0.03 & 0.03 & 0.03 & 0.03 & - & 0.05 \\ 0.02 & 0.01 & 0.01 & 0.01 & 0.03 & - \end{pmatrix}$$

The corresponding relations $r_i(\alpha_i)$ are depicted in *Figure 22* for all six voltage dividers. The slope of the curves r_i for $i = 1 \dots 5$ is the same due to the same fixed capacitor $\tilde{C}_i$. Since the capacitor $\tilde{C}_6$ is intentionally larger than the others, the slope of r_6 is smaller than the others. The curve r_5 is shifted to larger values due to the coupling of the objective lens, which is electrically connected to pad 5, to the grounded holder of the electrode. This effectively increases C_5 with respect to C_i for $i = 1 \dots 4$.

In principle the coupling capacities r_{ij} depend on the distance h between the electrode and the substrate. However, I neglected this dependency for the sake of simplicity. Even with this simplification I observed an accuracy in the electric potentials of about $2\ \%$.

Large changes of the orientation of the electric field vector within the liquid-crystal resin, lead to strong orientational defects in the resin. The relaxation time to the ordered ground state appears to be irreproducible and varies from seconds to minutes. Hence, it is better to divide large changes in the orientation of an electric field in smaller steps. If one wants to change the orientation of the electric field from $(\phi_\mathrm{s}, \theta_\mathrm{s})$ to $(\phi_\mathrm{e}, \theta_\mathrm{e})$, then one can add intermediate states along the great circle connecting both configurations. Starting from the coordinates of the start and end configurations given by

$$\vec{v}_\mathrm{s} = \begin{pmatrix} \cos\phi_\mathrm{s} \sin\theta_\mathrm{s} \\ \sin\phi_\mathrm{s} \sin\theta_\mathrm{s} \\ \cos\theta_\mathrm{s} \end{pmatrix}, \vec{v}_\mathrm{e} = \begin{pmatrix} \cos\phi_\mathrm{e} \sin\theta_\mathrm{e} \\ \sin\phi_\mathrm{e} \sin\theta_\mathrm{e} \\ \cos\theta_\mathrm{e} \end{pmatrix}, \tag{190}$$

the intermediate points $\vec{v}_n$ can be calculated by

$$\vec{v}_n = \vec{v}_s \cos n\Delta\alpha + \frac{(\vec{v}_s \times \vec{v}_e) \times \vec{v}_s}{|(\vec{v}_s \times \vec{v}_e) \times \vec{v}_s|} \sin n\Delta\alpha \tag{191}$$

with

$$n \leq \frac{\cos^{-1} \vec{v}_s \cdot \vec{v}_e}{\Delta\alpha}. \tag{192}$$

Here, I chose $\Delta\alpha = 15°$ for the setup. With this strategy the orientational defects within the resin vanish reproducibly after a few seconds when changing the orientation of the electric field within the liquid-crystal resin.

3.2.3 Mounting and Electrical Connection

For an easy handling of the fragile electrode, it is glued to a chip made from polyoxymethylene, as depicted in *Figure 23a* and *Figure 23b*. The pads of the electrode are connected to copper stripes on the chip via a conducting silver epoxy glue (Polytec EC244). In between the copper stripes, a non-conducting epoxy glue (UHU Plus Endfest 300) is employed to fix the electrode from the bottom to the chip and to prevent

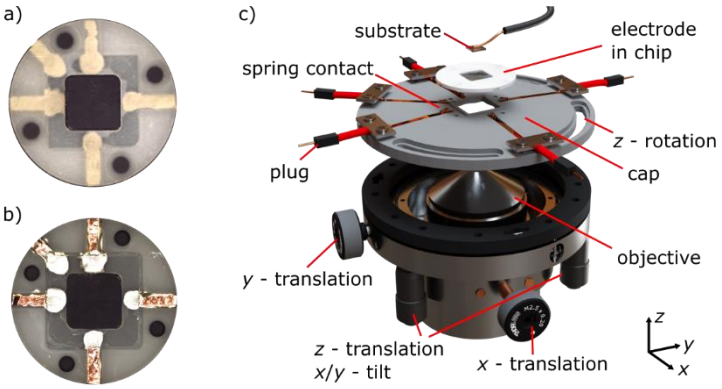

Figure 23. (a) Top view of an electrode mounted in a chip. (b) Bottom view of an electrode mounted in a chip. Copper stripes are used to contact the electrode via spring contacts located on the electrode holder. (c) The electrode holder surrounds the objective lens. The position and orientation of the electrode can be adjusted via fine-adjustment screws, micrometre screws and slotted holes on the cap of the holder.

leakage of liquid-crystal resin applied to the top of the electrode. For a good adhesion of the glue to the polyoxymethylene, it is important to treat the chip with an air plasma for about 45 minutes.

To position the electrode above the objective lens, the chip is screwed onto a holder surrounding the objective lens as shown in *Figure 23c*. With this holder it is possible to translate the electrode in the x – and y – direction with two fine-adjustment screws. Translation in the z – direction is possible with three micrometer screws that also allow to tilt the electrode around the x – and y – axis. The slotted holes in the cap of the holder allow a rotation around the z – axis.

The chip is electrically connected via spring contacts located on the cap of the holder. They press onto the copper stripes on the chip that hold the electrode. The spring contacts are connected via copper stripes to plugs that are fixed to the cap of the holder. Via these plugs, the electrode is connected to the voltage dividers that are described in section 3.2.2.

To prevent electrical breakdowns between pad 5 of the electrode and the objective lens, which are separated by $100\ \mu\mathrm{m}$, the objective lens and pad 5 are electrically connected. This connection is realized with a wire pushing onto the objective lens. The wire is fixed to the cap of the holder and connected to pad 5 of the electrode. To electrically

isolate the objective lens from the environment, its threaded mount is made from polyvinylchloride.

To prevent accidents and user injuries, all accessible conductive parts of the holder are set to ground and the high-voltage copper stripes on the cap are isolated with a polyimide tape.

A drawback of the described strategy to mount the electrode within a chip is that the electrode is not the topmost part. The boundaries of the electrode are covered with $400\ \mu\mathrm{m}$ of polyoxymethylene of the chip. Since the distance between the electrode and the substrate starts from $h = 100\ \mu\mathrm{m}$, the substrates must fit into the opening of the chip which is $8\ \mathrm{mm} \times 8\ \mathrm{mm}$. I chose a size of $3\ \mathrm{mm} \times 3\ \mathrm{mm} \times 0.47\ \mathrm{mm}$ for the substrates. These dimensions allow the substrates to dip into the chip's opening and also allows for a horizontal translation of the substrate during the printing. This is important to print structures larger than the printing area.

As described in section 3.2.1, it is necessary that the substrates are electrically conducting on their backside. For simplicity, the substrates were not coated with indium tin oxide but mounted on the counter-electrode, a glass substrate that is coated with indium tin oxide. This conducting layer is connected to a voltage divider described in section 3.2.2. The substrate is fixed to this counter-electrode with fix-o-gum (Marabu) applied to the side walls of the substrate. This allows the substrate to move very close to the electrode, since no glue is on top of the substrate.

3.2.4 Alignment of the Electrode

At the beginning of the printing process the electrode and the substrate are at a distance of $h = 100\ \mu\mathrm{m}$. Due to the large extent of the electrode ($13\ \mathrm{mm} \times 13\ \mathrm{mm}$) only a small tilt between electrode and substrate is allowed. This requires a parallel alignment of the electrode and the substrate.

To observe the tilt of the electrode and the substrate with respect to the front lens of the objective lens, a Helium-Neon laser beam is employed. The laser is reflected off the surface to be aligned and the reflex is observed at a $60\ \mathrm{cm}$ distant screen. As reference, the position of the reflex from the objective lens' front lens is marked on the screen before applying immersion oil. Then the electrode and the substrate are aligned such, that the corresponding reflexes impinge at the reference mark on the screen. Following this method, an accuracy in parallelism of about $0.4\ \mathrm{mrad}$ is achievable. This value translates to a separation height difference of $5\ \mu\mathrm{m}$ across the electrode.

To set the correct height of the electrode with respect to the objective lens, an additional lens in a removable mount is placed in front of the camera (see section 3.4) to image the plane $100\ \mu\mathrm{m}$ below the nominal focal plane of the objective lens. The electrode is in the correct position, when the top pattern of the electrode is sharp in the camera image.

To centre the electrode with respect to the printing field, four alignment markers in the top pattern of the electrode are employed. Those are visible as small squares in the inset of *Figure 16a*.

3.2.5 Cleaning of the Electrode

To clean the electrode, the chip with the electrode is removed from the holder. The chip is then placed in acetone and ultrasonicated for 10 minutes. Afterwards, it is placed in deionized water and ultrasonicated again for 10 minutes. Then, the electrode is dried in a stream of nitrogen. It is important to perform this procedure after and directly before using the electrode. Otherwise, I observed that the director of the liquid-crystal resin is aligned in random patterns at the surface of the electrode.

3.2.6 Fabrication of the Electrode

The electrodes were fabricated in a cleanroom to prevent contamination with dust during the fabrication. Dust on the substrates prior to the indium tin oxide (ITO) evaporation can lead to spikes in the ITO layer. These spikes can lead to electrical breakdowns due to field concentration. Furthermore, dust on the substrate or in the resin during spin-coating can lead to defects in the pattern of the electrode.

As substrates for the electrodes, D263M coverslips with a size of $13\ \mathrm{mm} \times 13\ \mathrm{mm} \times 0.17\ \mathrm{mm}$ were used. The coverslips were cleaned in a multi-step procedure adapted from a procedure provided by Schott AG. In this procedure, the substrates were ultrasonicated alternatingly in $60\ °\mathrm{C}$ hot detergent baths and baths of pure deionized $60\ °\mathrm{C}$ hot water. In the first step, Deconex OP 146 (Borer Chemie AG, $4\ \mathrm{vol}\%$) was used as a detergent. In the second step, Deconex OP 12PA-x (Borer Chemie AG, $2\ \mathrm{vol}\%$) was used and in the third step, Deconex OP 171 (Borer Chemie AG, $2\ \mathrm{vol}\%$) was employed. Afterwards, the substrates were dried in a stream of nitrogen.

The clean substrates were then coated with $100\ \mathrm{nm}$ ITO on both sides by electron beam deposition at a deposition rate $0.5\ \mathrm{Å\ s^{-1}}$ with a distance of $39\ \mathrm{cm}$ between the crucible and the substrates. During the deposition, the oxygen partial pressure in the evaporation chamber was set to $5 \cdot 10^{-5}\ \mathrm{torr}$. The coated substrates were then heated to

$550\ °C$ for $1\ h$ to oxidize the ITO layers in a tube furnace. Afterwards, the oven was switched off and the samples cooled down slowly to room temperature.

To structure the ITO, a $3\ \mu m$ thick layer of AZ10XT (Microchemicals) was spin-coated onto the substrate at $4000\ U\ min^{-1}$ followed by pre-bake at $110\ °C$ for 2 minutes in an oven. Then, a flood-illumination with the front-side pattern for was performed 29 seconds at $13\ mJ\ cm^{-2}$ using a mask aligner (Karl Suess MA/BA 6). The back side of the substrates was then spin-coated and pre-baked to protect the second ITO layer. Afterwards, the substrates were development in AZ400K (Microchemicals) and deionized water $(1{:}\ 4)$ for 8 minutes followed by an etching step with aqua regia consisting of HCl $(20\ vol\%)$ and HNO3 $(5\ vol\%)$ for 30 minutes. After etching, the substrates were washed with acetone in an ultrasonic bath. The same procedure was repeated to structure the back side of the substrate.

At the end, both sides were coated with $100\ nm\ SiO_2$ for electrical insulation via electron beam deposition at a rate of $1\ Å\ s^{-1}$ in the presence of oxygen at a partial pressure of 10^{-5} torr.

3.3 Laser Focussing into Birefringent Media

For 3D laser microprinting, it is necessary to obtain a single confined laser focus within the resin used for printing. Obtaining a single confined laser focus is a difficult task, since the resins employed in this thesis are birefringent. In general, when a wave hits the interface between the electrode and the birefringent resin, an ordinary and an extraordinary wave are induced as illustrated in *Figure 24a.* It is intuitive, that this will not lead to a good focus quality. Moreover, for a director perpendicular to the interface even two separate foci can appear.

In the following I present a strategy that allows for a single confined laser focus within the birefringent resin for a large set of different director orientations. The strategy assumes that the refractive index of the immersion oil and the electrode coincide with the ordinary refractive index of the liquid-crystal resin. If it is possible to suppress the transmission of the printing laser into extraordinary modes a laser focus of good quality must be the result. Then the situation is equivalent to a homogeneous isotropic medium with a refractive index for which the objective lens is optimized.

In the rest of this section I show that the suppression of the extraordinary modes is possible with the proper polarization of the printing laser. In detail, for a director perpendicular to the substrate an azimuthal polarization is sufficient, while for a

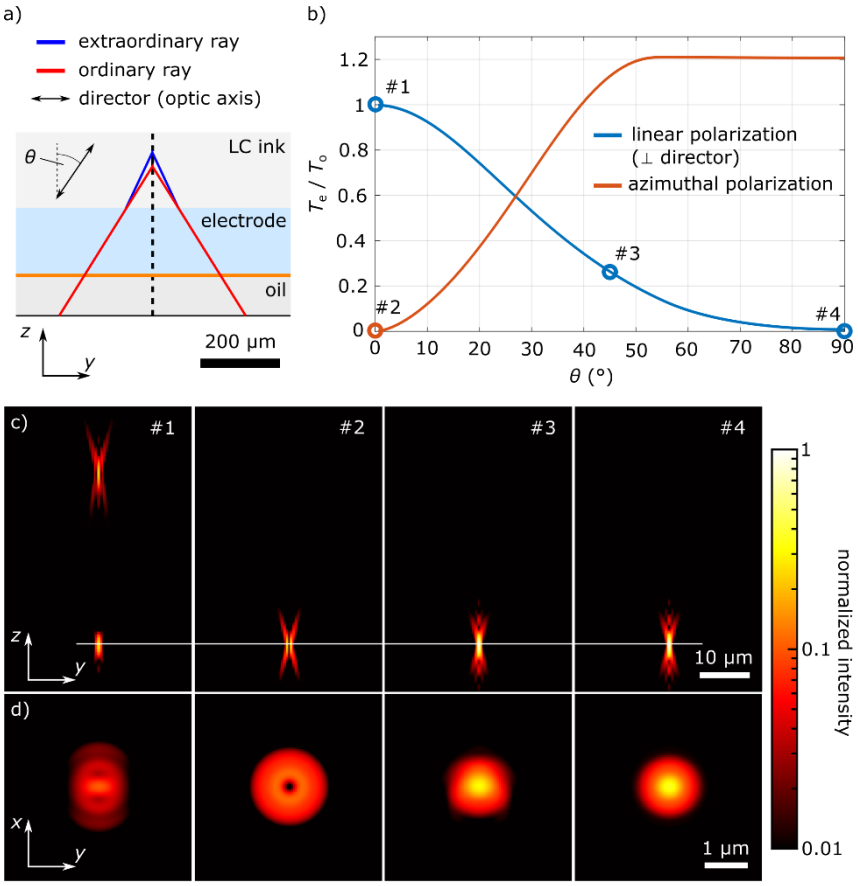

Figure 24. (a) Schematic cut close to the laser focus. Rays of the focused laser beam excite an ordinary and an extraordinary ray at the interface between electrode and resin. (b) Power that is transmitted to extraordinary modes divided by the power transmitted to ordinary modes depending on the director orientation for two different polarizations of the printing laser. Four special cases are highlighted. (c) Normalized spatial intensity profile in a plane containing the optical axis. Each panel corresponds to one of the highlighted cases. Case #1 shows two foci, while the cases #2 - #4 show a single focus. (d) Normalized spatial intensity profile in the focal plane indicated by the white line in panel (c). Figure taken from [88] (CC BY 4.0).

director parallel to the substrate a linear polarization perpendicular to the director is sufficient.

Moreover, it turns out that printing is possible for a large set of director orientations using an azimuthal or a linear polarization of the printing laser.

To get an overview I employ a ray optics model to calculate the fraction of the power that is transmitted into extraordinary modes divided by the power transmitted into ordinary modes. As discussed above, a low fraction indicates a good focus quality.

The calculation starts from the Fourier spectrum of the field refracted by the objective lens, delivered by the Richards-Wolf method, described in section 2.3.2. Each wave in the refracted spectrum originates from a ray of the laser beam that can be labelled in cylindrical coordinates by ρ and φ (see *Figure 10*). For every plane wave (ρ, φ) in the spectrum I calculated the transmittance $T_\mathrm{o}(\rho, \varphi)$ with respect to the ordinary mode and $T_\mathrm{e}(\rho, \varphi)$ with respect to the extraordinary mode according to formulas (87) and (88) described in section 2.2.2. To obtain the overall transmittance to the ordinary and extraordinary modes, I integrated the transmitted energy of all rays in the laser beam normalized to the overall energy as described by formulas (193) and (194). For the beam profile I assumed a gaussian profile as described by Formula (195).

$$T_\mathrm{o} = \frac{\int_0^{\rho_\mathrm{max}} \int_0^{2\pi} I_\sigma(\rho) T_\mathrm{o}(\rho, \varphi) \rho d\rho d\varphi}{\int_0^{\rho_\mathrm{max}} \int_0^{2\pi} I_\sigma(\rho) \rho d\rho d\varphi} \tag{193}$$

$$T_\mathrm{e} = \frac{\int_0^{\rho_\mathrm{max}} \int_0^{2\pi} I_\sigma(\rho) T_\mathrm{e}(\rho, \varphi) \rho d\rho d\varphi}{\int_0^{\rho_\mathrm{max}} \int_0^{2\pi} I_\sigma(\rho) \rho d\rho d\varphi} \tag{194}$$

$$I_\sigma(\rho) = I_0 e^{-\frac{\rho^2}{2\sigma^2}} \tag{195}$$

Figure 24b shows the ratio $T_\mathrm{e}/T_\mathrm{o}$ for linear polarization perpendicular to the optic axis (blue) and azimuthal polarization (red) versus the orientation of the optic axis represented by $0 < \theta < \frac{\pi}{2}$. These θ represent all possible orientations of the optic axis. The ratio is zero for an azimuthal polarization and $\theta = 0$ indicating that all transmitted energy is transmitted to the ordinary modes. In contrast, it is unity for a linear polarization indicating that half of the transmitted energy goes to extraordinary modes. In contrast, for $\theta = \pi/2$ the ratio is zero for linear polarization and larger than one for azimuthal polarization. In between the ratio is below 0.5 for angles $\theta > 35°$ for linear polarization and below 0.5 for angles $\theta < 25°$ for azimuthal polarization.

I conclude that the laser focus quality is good for a director perpendicular to the substrate using an azimuthal polarization of the printing laser. In contrast, for a director parallel to the substrate, a linear polarization perpendicular to the director is sufficient for a good focus quality. The calculations also raise the hope that for the director configurations in between one of the two polarizations of the laser beam are sufficient for printing.

To assess the focus quality, Dominik Beutel calculated spatial intensity profiles within the liquid-crystal resin for different director orientations using the formalism described in section 2.3. The resulting spatial intensity profiles are depicted in the four panels in *Figure 24c* and *Figure 24d*. Each panel corresponds to one of the highlighted cases in *Figure 24b. Figure 24c* shows a cut containing the optical axis, while *Figure 24d* shows a cut through the focal plane. In the first panel, the director is oriented perpendicularly to the interface, while the printing laser is linearly polarized. A well confined laser focus is visible in the focal plane of the objective lens, which is indicated by a white line. However, a second laser focus exists separated from the first one on the optical axis, which is clearly unwanted for printing. Changing the polarization of the printing laser to an azimuthal polarization results in a single confined laser focus in the focal plane as depicted in the second panel. In the focal plane the focus shows the expected toroidal shape. The third and the fourth panel show the spatial intensity distribution for $\theta = 45°$ and $\theta = 90°$ while the printing laser is polarized linearly and perpendicularly to the director. For both configurations a single well confined laser focus is visible. These results support the conclusion that the printing laser can be focused into the liquid-crystal resin for a large set of different director orientations.

For all calculations shown, a refractive index of 1.5 was assumed for the immersion oil and the electrode. The ITO on the surface of the electrode was neglected. The ordinary index of the resin was assumed to be 1.5 while the extraordinary index was assumed to be 1.7. For the objective lens a magnification of 25 and a numerical aperture of 0.8 were assumed resulting in $\rho_{\max} = 5.3\ \mathrm{mm}$ and $f = 6.6\ \mathrm{mm}$. For the laser beam $\sigma = 4.75\ \mathrm{mm}$ and $\lambda = 790\ \mathrm{nm}$ were assumed. The distance between the surface of the electrode and the focal plane was $100\ \mu\mathrm{m}$.

3.4 Optical Setup

The optical setup of the printer presented in *Figure 25* is a modified version of the setup described in [90] and was mainly built by Vincent Hahn and Pascal Kiefer. The automated polarization control was added to the setup by me.

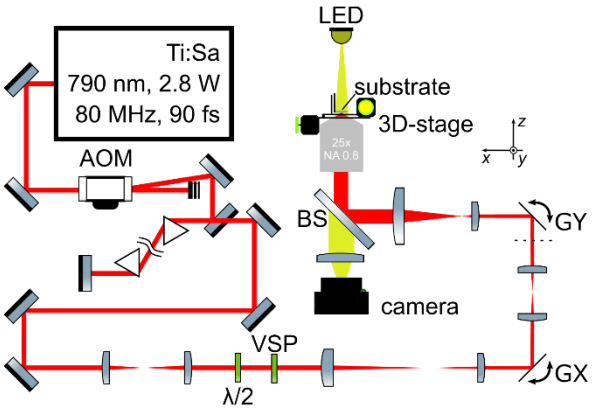

Figure 25. Optical setup of the used 3D laser printer. The green components represent the polarization control. The polarization control consists of a broadband half-wave plate ($\lambda/2$) in a rotation mount that rotates the linear polarization of the laser and a variable spiral plate (VSP) that can convert linear polarization to an azimuthal polarization. Figure taken from [88] (CC BY 4.0).

For the experiments presented in section 3.6 a titanium sapphire laser (Spectra Physics MaiTai) was employed with a wavelength of $790\ \mathrm{nm}$, a repetition rate of $80\ \mathrm{MHz}$ and a pulse duration of $90\ \mathrm{fs}$. For the experiments presented in Chapter 4 the laser was replaced by a Coherent Chameleon Ultra II with a wavelength of 790 nm, a repetition rate of $80\ \mathrm{MHz}$ and a pulse length of $140\ \mathrm{fs}$. At the entrance pupil of the objective lens a pulse length of $166\ \mathrm{fs}$ was measured. The laser is modulated by an acousto-optical modulator (AOM, AA MT80-A1.5-IR). To automatically rotate the linear polarization a broadband half-wave plate was employed in a motorized rotation mount. To switch between linear polarization and azimuthal polarization a variable spiral plate from Arcoptix was used. Both were positioned in a conjugate plane of the entrance pupil of the objective lens. Two separate galvanometric mirrors (GX, GY, Cambridge Technology 6215H) were employed to scan the laser focus within the printing area. The dashed line between the two galvanometric mirrors indicates a flip in the coordinate system, necessary to image the setup in a plane. Passing the galvanometric mirrors, the laser is focused by an objective lens (Zeiss LCI Plan-Neofluar 25×/0.8) into the liquid-crystal resin located between the electrode and a substrate. The substrate is mounted to a 3D translation stage (Märzhäuser-Wetzlar Scan IM 120 × 100, PI Q-545.140). A light-emitting diode (LED) and a camera are used to observe the printing process.

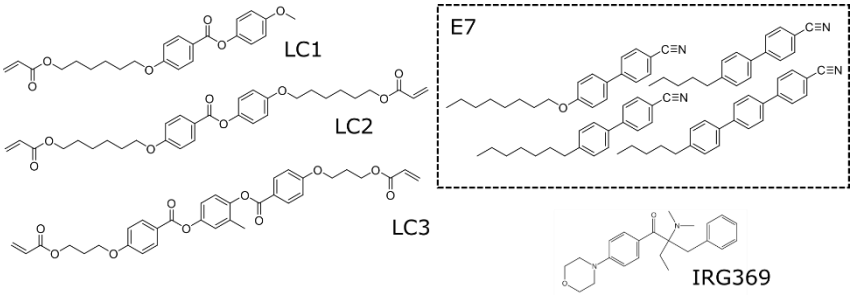

Figure 26. *Molecules employed in the two resins used in this thesis. LC1 – LC3 are nematic mesogens with an acrylate group. The E7 mixture consists of four different nematic mesogens. It is used to dissolve the reactive mesogens LC1 – LC3. Irgacure 369 (IRG369) is a photo-initiator used to start a photopolymerization.*

3.5 Liquid-Crystal Resins

In this section I describe the composition of two liquid-crystal resins employed in this thesis and compare the resulting liquid-crystal elastomers with regard to thermal expansion and thermal stability.

The presented 3D laser microprinting approach requires a liquid resin, since the distance h between the electrode and the substrate varies in height during printing. This requires the resin to flow. Furthermore, the resin must be in a nematic state during the printing, in order to be aligned by the electric fields. Within this work, two different liquid-crystal resin compositions were employed that satisfy both requirements. The second resin is an improved version of the first one.

Both employed resins are composed of the molecules depicted in *Figure 26*. Irgacure 369 (IRG369) is a photoinitiator used to start a two-photon induced polymerization reaction. The molecules LC1 – LC3 are reactive nematic mesogens that form a liquid-crystal elastomer upon polymerization. All three mesogens are solid at room temperature. Therefore, I dissolved them in E7 mixture, whose composition is also depicted in *Figure 26*. However, this comes at the cost of a large shrinkage after development, since the E7 mixture is not part of the network after polymerization. It is therefore necessary to use as less E7 mixture as possible.

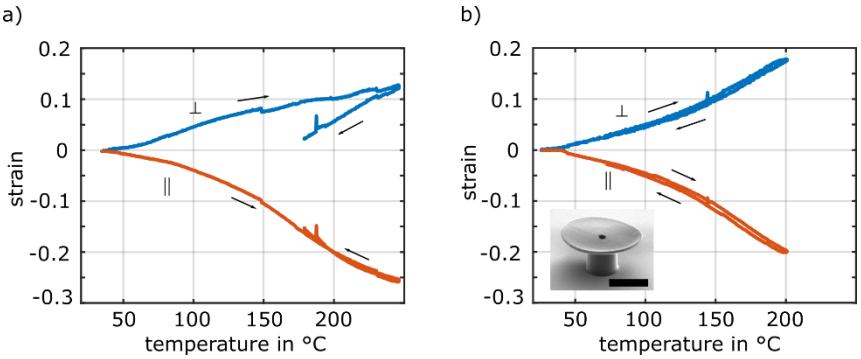

Figure 27. *Strain parallel and perpendicular to the director versus temperature for a heating and a cooling cycle. (a) Data for a liquid-crystal elastomer printed from Resin 1. The strain perpendicular to the director is not identical for the heating and the cooling cycle. The deformation is not reversible. (b) Data for a liquid-crystal elastomer printed from Resin 2. The strain perpendicular to the director is nearly identical for the heating and the cooling cycle. The deformation is reversible. The inset shows a membrane supported by a cylindrical post that was used to measure the data. The scale bar is 30 µm. The figure is taken from [93] (CC BY 4.0).*

Table 1. Composition of the resins used in this thesis. The labels correspond to the molecules depicted in Figure 26.

	Resin 1	**Resin 2**
LC1	33.1 wt%	50 wt%
LC2	-	12 wt%
LC3	16.5 wt%	12 wt%
E7	49.7 wt%	25 wt%
IRG396	0.7 wt%	1 wt%

The composition of both resins is given in *Table 1*. Resin 1 consists of the monomers LC1 and LC3. To form a stable resin which stays liquid at room temperature it is necessary to add the same amount of E7 than monomers. The resin composition is inspired by [58, 91].

Resin 2 contains LC2 in addition. This drastically increases the solubility of the monomers in the E7 mixture. In Resin 2 only 25 wt% of E7 is required to form a stable resin which stays liquid at room temperature. Adding LC2 to the resin was inspired by

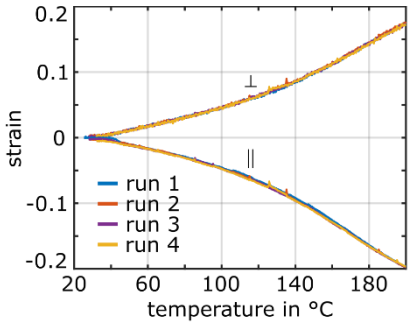

Figure 28. Strain parallel and perpendicular to the director versus temperature for four consecutive heating cycles. The strain is referenced to the initial extent of the membrane in the first run at room temperature. The strain is fully reversible and repeatable. The figure is adapted from [93] (CC BY 4.0).

McCracken *et al.* They found that the crystalline to nematic transition temperature drastically dropped by adding LC2 to their resin [92].

To prepare the resins, all components were added to a vial and heated to 80 °C under constant stirring. Subsequently, to remove insoluble remains, the resin was filtered with a $0.45\ \mu m$ PTFE syringe filter with a diameter of $13\ mm$. Prior to printing, the resin was heated to $80\ °C$ to ensure a homogeneous solution. All mesogens were bought from SYNTHON Chemicals GmbH & Co. KG and used without further purification.

To measure the thermal expansion of the resulting liquid-crystal elastomers, I printed small disk-like membranes supported by a cylindrical post from both resins with a homogeneous director in the plane of the membrane. A scanning electron micrograph of

such a structure is depicted in the inset of *Figure 27b*. The structures printed from resin 1 were developed in isopropanol at $40\ °C$ for $90\ s$ to prevent heavy shrinkage. The structures printed from resin 2 were developed for 15 minutes in ethanol and were dried in a critical-point dryer.

I observed the membranes in an optical light microscope equipped with an Instec mk2000 heating stage. With the heating stage, I performed a heating and a cooling cycle with a heating rate of $10\ °C\ min^{-1}$ and took images at different temperatures reaching up $250\ °C$. In each picture I fitted ellipses to the shape of the membranes to obtain the extent parallel and perpendicular to the director. Referencing the extent at a certain temperature to the extent at room temperature resulted in a strain of the membrane at that temperature. The resulting strain versus temperature behaviour along and

perpendicular to the director is displayed in *Figure 27a* for resin 1 and in *Figure 27b* for resin 2.

It is clearly visible that the liquid-crystal elastomer formed from resin 1 does not behave the same in the heating cycle compared to the cooling cycle. In contrast, the liquid-crystal elastomer formed from resin 2 behaves fully reversible in the presented experiment. I assume that not all E7 mixture was removed in the development of the membranes from resin 1 due to the short development time. Therefore, E7 mixture could evaporate at elevated temperatures.

To test the repeatability of the thermal actuation of the liquid-crystal elastomer formed from resin 2, I cycled the temperature from room temperature to 200 °C for four times and observed the shape of the membrane. For the calculation of the strain, I referenced to the extent within the first cycle at room temperature. The resulting strain versus temperature behaviour for the five cycles is given in *Figure 28*. The thermal expansion is fully repeatable.

For all membranes no shrinkage was observed along the director. For the membranes printed with resin 1 a shrinkage of about 13 % perpendicular to the director was observed. For longer development times, the shrinkage was significantly larger. For the membranes printed with resin 2 a shrinkage of about 14 % was observed perpendicular to the director. Using the development strategy employed for resin 1, only a shrinkage of 6 % was observed perpendicular to the director for resin 2. However, the thermal expansion was irreversible again, similar to the structures made from Resin 1. This observation supports the hypothesis that remaining E7 evaporates during heating when it is not fully removed during development.

3.6 3D Printed Test Structures

In this section, three different kinds of 3D printed samples are discussed. The first set of samples proves that structures with a homogeneous director field for several director orientations can be printed. The second example proves the ability to print structures with an inhomogeneous director field. Finally, the third example shows that even structures exhibiting complex motions like a buckling instability can be fabricated with the presented 3D printing technique.

All structures presented in this section are printed with the first resin composition described in section 3.5. The used substrates were functionalized with 3-(trimethoxysilyl)propyl methacrylate to promote adhesion of the samples to the substrate. For doing that, the substrates were activated with an air plasma for 5 minutes and afterwards

placed inside a desiccator with a droplet of about $10\ \mu L$ of silane for 1 hour. All samples were developed in isopropanol at $40\ °C$ for 90 seconds. The electric field strength during printing nominally was $0.3\ V\ \mu m^{-1}$ for all director orientations. After every stage movement in z – direction of $0.5\ \mu m$ during printing, a pause of $20\ ms$ was implemented and a pause of 2 seconds was implemented for larger stage movements to settle motions in the resin that disturb the director field.

3.6.1 Homogeneous Alignment

To proof that the presented 3D printing technique allows to control the director, I printed several test structures with different director orientations. The structures consist of disc-like thin membranes oriented parallel or perpendicular to the substrate and are supported by cylindrical posts. For both orientations of the membranes, I printed five samples. Four with a director in the plane of the membrane, each rotated by 45° respectively and one with a director perpendicular to the plane for both orientations of the membrane. The designed orientation of the director is indicated in the top panel of *Figure 29* together with bright field microscope images of the structures. In the bright field images, the structures show an ellipsoidal shape already indicating the director orientation. The director is oriented along the semi-major axis since there is only shrinkage perpendicular to the director orientation as described in section 3.5. This coincides with the designed director orientations.

Scanning electron micrographs are depicted in the bottom panel of *Figure 29*. I want to emphasize the defined shape of the structures that indicate a good focus quality for all director orientations.

Since the director coincides with the optic axis of the liquid-crystal elastomer, it is also possible to verify the director orientation with a polarizing optical microscope. In a polarizing optical microscope, the sample is located between two crossed linear polarizers. Due to the crossed polarizers, light can only pass if its polarization is rotated by the sample. This means, that no light is transmitted, whenever the optic axis of the sample is parallel or perpendicular to one of the polarizers. Polarizing optical microscope images of the structures are depicted in the third panel of *Figure 29* for two different orientations of the polarizers as indicated by the arrows in the panel. It is clearly visible, that the structure appears dark, whenever the designed director orientation is perpendicular or parallel to one of the polarizers. The small director rotations in the vicinity of the supporting post for $\theta = \pm 45°$ may be due to semi-soft deformations [76]. These semi-soft deformations may be caused by shrinkage during development inducing strains in the vicinity of the supporting cylindrical post.

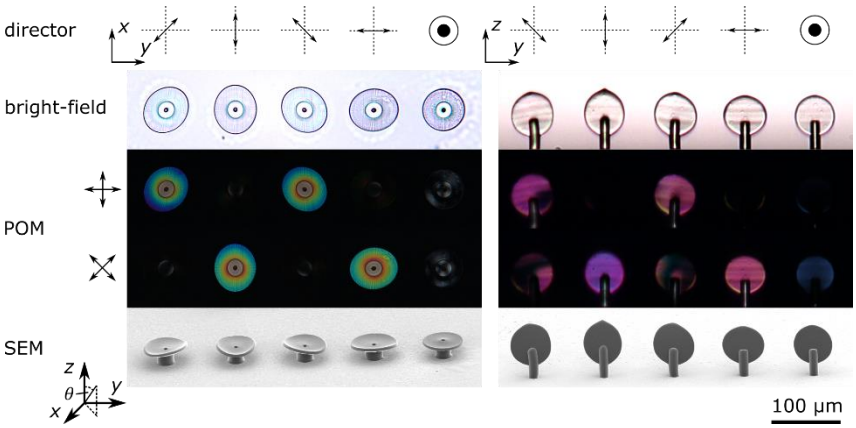

Figure 29. Circular membranes in the xy – plane and in the yz – plane supported by cylindrical posts. The director orientation is displayed by the arrows in the top panel. Bright-field light microscope images are shown in the second panel. The membranes appear elliptically deformed due to shrinkage after development, while the semi-major axis points in the direction of the director. The third panel shows polarizing optical microscope (POM) images, where the membranes are located between two crossed polarizers. The orientation of the polarizers is indicated by black arrows. The membranes appear dark whenever the designed director is parallel or perpendicular to one of the polarizers. Scanning electron micrographs (SEM) are shown in the bottom panel. The printed structures appear defined indicating a good focus quality of the printing laser. Figure taken from [88] (CC BY 4.0).

I conclude, that it is possible to print structures with a defined director orientation in the case of a homogeneous director field. In the next section I present structures that successfully implement an inhomogeneous director field.

Printing Parameters

The structures on the left-hand side of *Figure 29* are printed in a spiral with a hatching of $0.08\ \mu\text{m}$ and a slicing distance of $0.5\ \mu\text{m}$ at a speed of $5\ \text{mm}\ \text{s}^{-1}$. The laser power was $28\ \text{mW}$ for $\theta = 0°$ and $32\ \text{mW}$ for $\theta = 90°$.

The structures on right hand side of *Figure 29* are printed using straight hatching lines with a distance of $0.05\ \mu\text{m}$. The slicing distance was $0.5\ \mu\text{m}$ and the scan speed was $5\ \text{mm}\ \text{s}^{-1}$. The laser power was $36\ \text{mW}$ for $\theta < 90°$ and $24\ \text{mW}$ for $\theta = 90°$.

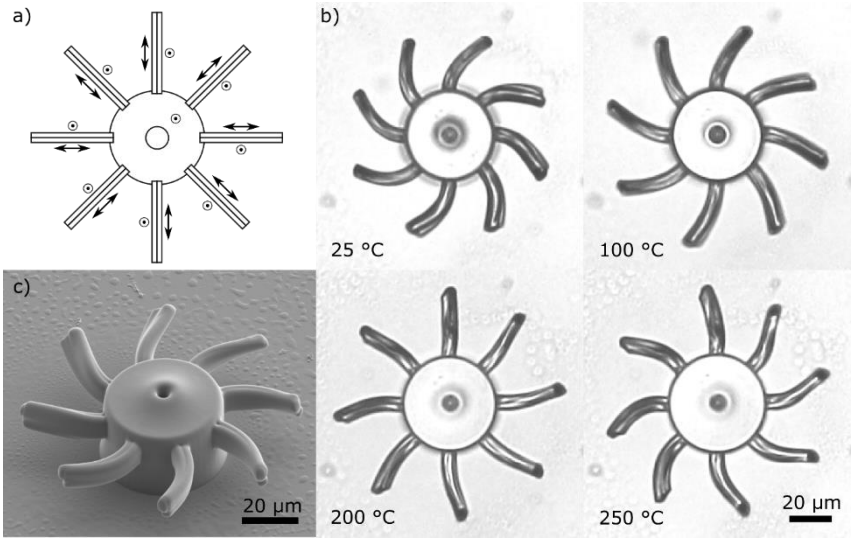

Figure 30. A 3D structure printed from liquid-crystal elastomer with an inhomogeneous director profile that performs a large bending motion on heating. (a) Printed geometry with arrows that indicate the designed director profile. It shows a central post with eight arms attached to it. Each arm consists of two layers, while the director in one layer is tangential to the beam and in the other layers the director points out of the plane. (b) Optical light microscope images of a printed structure at different temperatures. A large bending motion of the eight arms in the counter-clockwise direction is visible. (c) Scanning electron micrograph of the structure. Figure taken from [88] (CC BY 4.0).

3.6.2 Bi-Layered Beams

With the structure presented in this section I prove that the presented printing technique also allows to print structures with inhomogeneous director fields. The structure presented in this section consists of a cylindrical post with eight arms attached to it. Each arm consists of two layers with different director orientations as depicted in *Figure 30a*. The director is tangential to an arm in one layer and perpendicular to the substrate in the other layer. A scanning electron microscope image of the printed structure is shown in *Figure 30c*. In the scanning electron microscope image, a bending of the arms in a clockwise direction is visible. This is expected, since the constituent liquid-crystal elastomer shrinks only perpendicular to the director during development as discussed in section 3.5. Therefore, the layer on the right-hand side, viewing from the centre of the structure, reduces its length, while the length of the left-hand side layer remains

the same resulting in a bending in a clockwise direction. This is a first indicator that the director profile is as designed.

A second indicator that the director profile is as designed is the thermally induced motion of the structure. To study the thermally induced motion, the sample was placed in a heating stage connected to an optical light microscope that allowed to observe the structure during heating (see section 3.5). *Figure 30b* shows the structure at different temperatures. It is clearly visible that the arms bend in the counter-clockwise direction on heating. This behaviour is expected, since the left layer of each arm, viewing from centre of the structure, reduces its length on heating, while the right layer expands in length. This leads to the observed counter-clockwise bending of the arms.

Due to the expected deformation on shrinkage during development and the expected motion on heating, I conclude that the director profile of the printed structure is as designed. With the presented printing technique, it is also possible to print structures from liquid-crystal elastomer with an inhomogeneous director profile. These results made me confident to implement structures with yet more complex motions as discussed in the next section.

Printing Parameters

The supporting post of the structure was printed in a spiral with a hatching of $0.08\ \mu\mathrm{m}$ and a slicing distance of $0.5\ \mu\mathrm{m}$ at a scan speed of $5\ \mathrm{mm\ s^{-1}}$ and a laser power of $46\ \mathrm{mW}$. The arms were printed with straight hatching lines along the arm with a distance of $0.2\ \mu\mathrm{m}$ and a slicing distance of $0.5\ \mu\mathrm{m}$. The scan speed was $100\ \mathrm{mm\ s^{-1}}$ with a laser power of $101\ \mathrm{mW}$ for $\theta = 0°$ and $61\ \mathrm{mW}$ for $\theta = 90°$ and $\varphi = 0°$, $62\ \mathrm{mW}$ for $\varphi = \pm 45°$ and $63\ \mathrm{mW}$ for $\varphi = 90°$.

3.6.3 Towards Complex Motions

In this chapter, I want to show that even complex thermally induced motions like a mechanical buckling instability can be implemented with the presented 3D laser microprinting approach. A thermally induced mechanical buckling instability is a discontinuous mechanical motion at a critical temperature, which results from the geometry of the structure and not from any discontinuity in the thermal expansion of the constituent material. Close to the critical temperature, such an instability allows for large deformations by a small increase in temperature.

The structure to be discussed consists of cosine-shaped bars supported by rectangular shaped posts and is inspired by [94]. The printed geometry is depicted in *Figure 31a* together with the designed director profile. A scanning electron micrograph of the printed sample after development is shown in *Figure 31d*. The cosine shaped bars are

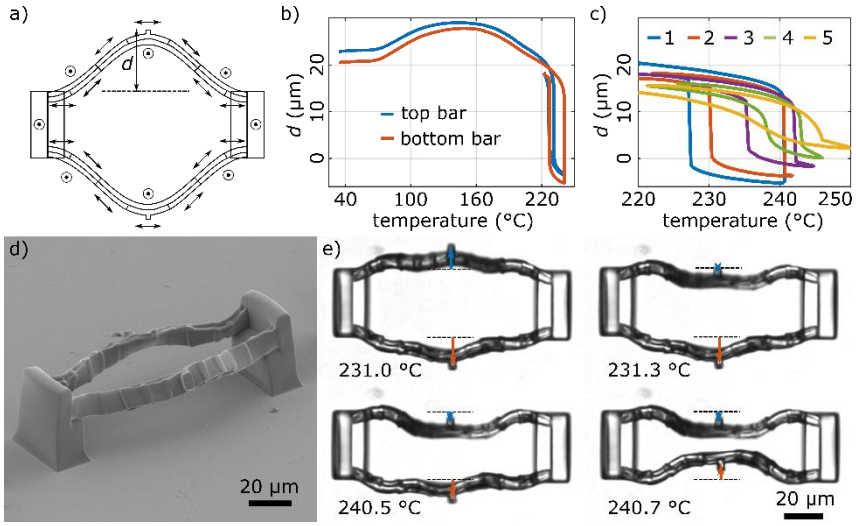

Figure 31. (a) Top view of the printed structure with arrows indicating the desired director field. It consists of two cosine-shaped bars supported by rectangular posts. The distance d between the tip at the middle of a bar and the supporting posts is defined. (b) The distance d is plotted versus the sample temperature for the top and bottom bar. The temperature is cycled from room temperature to $240\,°C$ and back again to $220\,°C$. There is a discontinuity in d for both bars in the heating and the cooling cycle. A hysteresis behaviour is visible. (c) The distance d is plotted versus the temperature. The temperature is cycled five times around the critical temperature of the top bar. The amplitude of the discontinuous jump in d decreases with every cycle. Cycle 5 does not show any discontinuity in d anymore. (d) Scanning electron micrograph of the printed structure. (e) Optical microscope images of the sample at the critical temperatures and slightly above. The large extent of the discontinuous motion is clearly visible. Figure taken from [88] (CC BY 4.0).

designed such, that the bars straighten on heating and thereby get compressed between the supporting posts. At some point the configuration gets unstable and the beams suddenly relax to the opposite direction.

To observe the motion of the beams, the sample is located in an optical microscope equipped with a heating stage (see section 3.5). To quantify the motion, the tip located at the middle of each beam is tracked via image cross-correlation [95]. From that, the distance d between the supporting post and the tip is calculated (see *Figure 31a*).

The quantity d is plotted versus the temperature of the sample in *Figure 31b* for both bars. It is clearly visible, that for the top bar there is a continuous change in d until a critical temperature of 230 °C. At the critical temperature a large discontinuous jump in d appears within a temperature step of less than 0.3 °C. In the cooling cycle, there

appears a discontinuous recovery in d at a temperature of 226 °C and therefore a hysteresis behaviour is observed. A similar behaviour can be observed for the bottom bar but with slightly different critical temperatures and a larger hysteresis. I attribute this difference to sample imperfections.

Light microscope images of the structure at the critical temperatures for the top bar and the bottom bar are depicted in *Figure 31e* together with images of the structure at temperatures slightly above the critical temperatures. The large and sudden deformation is clearly visible.

To investigate the repeatability of the mechanical buckling motion, the temperature was cycled five times around the critical temperature of the top bar, while tracking the tip of the top bar. In *Figure 31c* the resulting values of d are plotted versus the sample temperature. It becomes clear that the amplitude of the jump in d decreases with every cycle, while there is no discontinuity anymore in cycle 5. I assume that this degradation is due to a mixture of plastic or viscoelastic deformations caused by large strains in the top bar and the degradation of the constituent material that appears for the first resin mixture as discussed in section 3.5. As shown in section 3.5, the degradation of the constituent material can be resolved, however, plastic or viscoelastic deformation will remain a problem in terms of repeatability.

In conclusion, I presented a structure that successfully implemented a complex thermally induced mechanical buckling instability.

Printing Parameters

The rectangular posts were printed with straight hatching lines spaced by 0.2 µm and a slicing distance of 0.5 µm at a scan speed of 100 mm s^{-1} with a laser power of 108 mW. The bars attached to the posts were printed with cosine-shaped hatching lines along the bar with a distance of 0.2 µm and a slicing distance of 0.5 µm. The scan speed was 100 mm s^{-1} with a laser power of 108 mW for $\theta = 0°$ and 67 mW for $\theta = 90°$ and $\varphi = 0°$, 68 mW for $\varphi = \pm 45°$ and 69 mW for $\varphi = 90°$.

3.7 Discussion

In conclusion, I have presented a 3D laser microprinting method that allows to print complex 3D architectures from liquid-crystal elastomer with feature sizes in the range

of a few micrometres, while the overall sample size can be in the millimetre range. Many orientations of the director are possible, while the director can in principle be chosen independently at every point in space. The resulting liquid-crystal elastomers printed from resin 2 also show a fully reversible and repeatable thermal expansion.

Other 3D laser microprinting approaches published so far are based on sandwich cells where the director is aligned via specially prepared surfaces [47–55, 55–57] or a combination of surface alignment and vertical electric fields [58–60]. In contrast to the technique presented in this thesis, these approaches are all limited to sample heights in the range of about $100\ \mu\mathrm{m}$ due to the fixed height of the sandwich cell. The approaches based on surface alignment can achieve complex two-dimensional director patterns but only very simple 3D patterns like twists of the director field [54–56]. One approach to achieve more complex 3D director patterns was to print cubes with a homogeneous director field in a sandwich cell and manually assemble them in arbitrary orientations [57]. By this, also structures with more complex director fields can be achieved, however, the process appears time consuming and error-prone. In the approaches employing an additional vertical electric field one can choose between two director orientations at every point in space. The director is either aligned by the surface or by the electric field [58–60]. This allows for more complex director orientations. However, the choice of the director orientation is still limited to two different orientations in contrast to the approach presented in this thesis.

There is also a published approach combining digital light processor printing with magnetic fields to print liquid-crystal elastomers [61]. Compared to the approach introduced in this thesis, the director can only be adjusted in the horizontal plane, however, the orientation can be freely chosen within this plane at every point in space. The voxel size is about a factor of 50 larger and the presented sample sizes are up to $1\ \mathrm{cm}$.

Several groups have published direct ink writing approaches to print liquid-crystal elastomers [62–73]. There, the liquid-crystal elastomer is pushed through a nozzle and thereby mechanically aligned along the printing direction. This usually limits the director orientation to the horizontal plane. The printed structures published so far are either two dimensional or very simple 3D structures. The voxel is usually two orders of magnitude larger than what is presented here, while the size of the samples published so far is usually on the centimetre scale. However, the resulting liquid-crystal elastomers show similar actuations reported here for a much lower increase in temperature. Such resins are not yet available for 3D laser microprinting approaches.

Overall, I conclude that to my knowledge the technique described in this thesis is the only technique published so far that allows to print complex 3D architectures with the

free choice of the director orientation at any point in space. This is crucial for the fabrication of the 3D optomechanical metamaterials I present in the next chapter. Up to now, these metamaterials represent to my knowledge the most complex 3D structures fabricated from liquid-crystal elastomer presented in the literature.

4 Chapter 4
3D Optomechanical Metamaterials

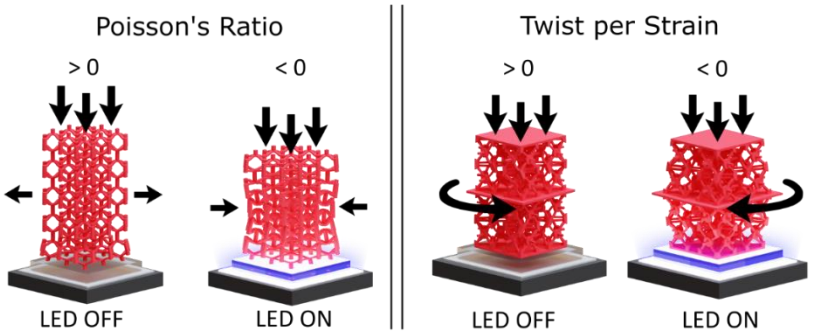

Figure 32. Illustration of two different 3D optomechanical metamaterials illuminated by a blue LED. (a) The Poisson's ratio of the metamaterial is positive for no illumination and monotonously decreases with increasing intensity of the LED. In the figure, the Poisson's ratio is negative for the illuminated case. (b) The twist per strain is positive for no illumination and continuously depends on the intensity of the LED. In the illustration, the twist per strain is negative for the illuminated case. Figure taken from [93] (CC BY 4.0).

In this chapter I demonstrate metamaterials that drastically change a mechanical property upon optical irradiation. I call this type of materials 3D optomechanical metamaterials. In a first example, I present a metamaterial whose Poisson's ratio continuously depends on the intensity of a blue LED irradiating the sample. Without any irradiation, the Poisson's ratio is positive, while it decreases monotonously with increasing intensity. For large enough intensities, even negative Poisson's ratios are possible. *Figure 32a* illustrates the metamaterial without illumination, where the Poisson's ratio is positive, and in an illuminated state exhibiting negative Poisson's ratio. This auxetic metamaterial is discussed in section 4.4.

As a second example, I present a chiral metamaterial that shows a twisting motion on compression, while the magnitude and the sign of the twist depend on the intensity of the blue LED present during application of a strain. *Figure 32b* shows a sketch of the metamaterial exhibiting a positive twist per strain on compression for no light present and a negative twist per strain for an illuminated state. This chiral metamaterial is presented in section 4.5.

Both metamaterials shown in this chapter are fabricated via the 3D laser printing technique introduced in chapter 3. After printing, the samples were dyed with disperse red 1 methacrylate to introduce a mechanism to absorb the light of the blue LED. The absorbed light is converted to heat [96] and thereby causes a thermal expansion that alters the geometry of the metamaterial. Section 4.1 covers the methods I employed for fabrication in detail.

In section 4.2, I discuss the methods used for characterisation of the metamaterials. In Section 4.3, I introduce a computer model employed to understand the behaviour of both metamaterials.

4.1 Sample Fabrication

To print both metamaterials shown in this chapter, I employed the 3D laser printing technique presented in chapter 3 using resin 2 presented in section 3.5. During printing, I manually added additional resin after each increase in distance of $200\ \mu\mathrm{m}$ between the electrode and the substrate.

For both metamaterials the hatching distance was $0.2\ \mu\mathrm{m}$ while the slicing distance was $0.5\ \mu\mathrm{m}$. The scan speed of the laser focus was $50\ \mathrm{mm\,s^{-1}}$. The laser power was $116\ \mathrm{mW}$ for a vertical director orientation, $104\ \mathrm{mW}$ for a diagonal director orientation and $78\ \mathrm{mW}$ for a horizontal director orientation. The laser powers were measured at the entrance pupil of the objective lens. The electric field strength was set to the maximum possible value for a given director orientation (see *Figure 21*).

After printing, I developed each sample for 15 minutes in ethanol followed by critical-point drying using ethanol as a solvent. It was necessary to be very careful during the sample transfer to the critical point dryer to ensure that the sample never falls dry.

To introduce a light absorber to the printed metamaterials, I dyed them after development with disperse red 1 methacrylate according to a recipe provided by Li-Yun Hsu (see also [97]). I prepared a solution of $1\ \mathrm{mg}$ of disperse red 1 methacrylate and $0.1\ \mathrm{mg}$ Irgacure 819 in $0.1\ \mathrm{ml}$ of a $10:1$ mixture of isopropanol and dichloromethane. Then, I clamped a developed sample in a PTFE holder that allows to entirely cover the

structure with $0.05\ \mathrm{ml}$ of dye solution. To prevent evaporation of the dye solution, I covered the holder with a coverslip. To fix the dye to the polymer matrix of the sample, I illuminated it with an UV LED (VL-4.LC @ $254\ \mathrm{nm}$) for 1 hour at a distance of $2\ \mathrm{cm}$. After the illumination, I washed the sample in ethanol and removed the solvent in a critical-point dryer.

4.2 Characterisation Setup

In this section, I present the setup used to characterize the printed 3D optomechanical metamaterials. To characterize a 3D optomechanical metamaterial according to its Poisson's ratio or twist per strain depending on the LED intensity, it is necessary to apply a strain during illumination of the sample. The employed setup is presented in *Figure 33a*. There, a sample is mounted upside down with glue (Marabu Fixogum) to an LED (Osram LE B P1W FY-W) which is screwed to a motorized and computer-controlled translation stage. The stage pushes the sample onto a glass sheet and thereby allows to apply a strain to the sample while the LED illuminates it. The glass sheet is covered with immersion oil (Zeiss Immersol 518F) to prevent that the sample sticks to the glass sheet. During the experiment, the sample is observed via two optical microscopes from the side and from the bottom through the glass sheet. The microscopes allow to record images of the samples before and after application of a strain. From these images the deformation of a sample is quantified via image cross-correlation. The details on the image cross-correlation depend on the studied metamaterial and are given in the sections 4.4 and 4.5.

To get a rough estimate of the light intensity at a distance d from the LED, I assume that the LED is a Lambertian emitter. A Lambertian emitter emits a power

$$\mathrm{d}^2P = \frac{P_{\mathrm{tot}}(I)}{A_1\pi}\cos\theta\,\mathrm{d}\Omega\,\mathrm{d}A_1 \tag{196}$$

from an infinitesimal area $\mathrm{d}A_1$ located at a point (x_1, y_1) on the emitters surface into the spherical angle $\mathrm{d}\Omega$. Here, $P_{\mathrm{tot}}(I)$ is the total power emitted by the LED with the emitting surface A_1 for a current I. If one is interested in the power that is transmitted to an infinitesimal surface $\mathrm{d}A_2$ at the point (x_2, y_2) on a plane at a distance d, the spherical angle can be replaced by

$$\mathrm{d}\Omega = \frac{\mathrm{d}A_2\cos\theta}{(x_2-x_1)^2+(y_2-y_1)^2+d^2} \tag{197}$$

and the angle θ can be estimated by

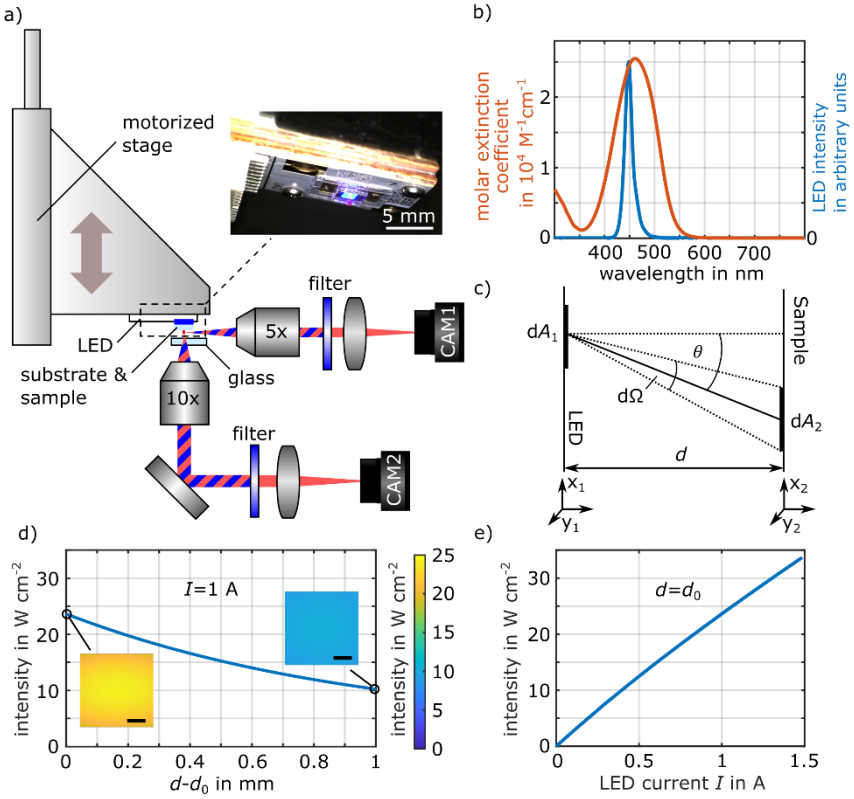

Figure 33. (a) The metamaterial samples are mounted upside down to an LED that is fixed to a motorized translation stage. The stage pushes the sample onto a glass sheet opposing the sample. The sample is observed with two optical microscopes from the side and from the bottom. The inset shows an optical photograph of a sample mounted onto the LED. The LED is emitting blue light. (b) Molar extinction coefficient of disperse red 1 in toluene and the LED intensity versus the optical wavelength. The LED emits at a wavelength that is close to the maximum in the molar extinction coefficient of the employed dye. (c) An infinitesimal area dA_1 on the LED emits light towards the infinitesimal area dA_2 on the sample. (d) Average Intensity in a plane at a distance d from the LED for an LED current of $1\ A$. d_0 is the distance from the bottom of a sample to the LED. The insets show the intensity in the plane. The scalebar is $250\ \mu m$. (e) Intensity of the LED versus the LED current at $d = d_0$. Figure is partially adapted from [93] (CC BY 4.0)

$$\cos\theta = \frac{d}{\sqrt{(x_2 - x_1)^2 + (y_2 - y_1)^2 + d^2}}. \tag{198}$$

The situation is depicted in Figure 33*c*.

The intensity $I(x_2, y_2)$ results from integration of d^2P over the emitting surface A_1 of the LED

$$I(x_2, y_2) = \frac{P_{\mathrm{tot}}(I)}{A_1\pi} d^2 \iint_{A_1} \frac{1}{((x_2 - x_1)^2 + (y_2 - y_1)^2 + d^2)^2} \mathrm{d}A_1. \tag{199}$$

Figure 33*d* shows the intensity averaged over a surface of $600\ \mu\mathrm{m} \times 600\ \mu\mathrm{m}$ at different distances d from the emitting surface of the LED for an LED current of $I = 1\ \mathrm{A}$. There, the distance between the bottom of a sample and the emitting surface of the LED is called $d_0 = 0.91\ \mathrm{mm}$. As expected, the intensity decreases with the distance d. The insets show the intensity in the plane at the specified distance d. Due to the large size of the emitting surface of the LED compared to the sample size, the homogeneity is acceptable. Figure 33*d* illustrates the averaged intensity versus the LED current at the distance d_0.

I obtained the necessary values for the overall emitted power of the LED by a simple measurement. First, I brought the LED in contact with a power sensor (Thorlabs S170C) to ensure that all emitted light is collected. In this step the LED current was low enough to not saturate the sensor. Then, I increased the distance between the sensor and the LED and measured the power falling on the sensor versus the LED current up to $1.5\ \mathrm{A}$. Referencing to the value measured in the first step, I obtained the full power $P_{\mathrm{tot}}(I)$ emitted by the LED for currents up to $1.5\ \mathrm{A}$ (not shown).

The emission spectrum of the LED is plotted in blue in Figure 33*b* together with the molar extinction coefficient of disperse red 1 methacrylate. The molar extinction coefficient of the dye was measured by Li-Yun Hsu in toluene with a concentration of $95.0\ \mu\mathrm{mol\ L^{-1}}$. The emission spectrum was measured by me with a spectrometer. The LED was chosen such that its peak in emission is close to the peak in the molar extinction coefficient of the employed dye.

4.3 Finite-Element Modelling

In this section, I present the model used to calculate the effective mechanical properties of the two metamaterials investigated in this thesis in response to the light of the blue LED. The model assumes that the metamaterials consist of a linear elastic material with an isotropic and homogenous Young's modulus of $Y = 20\ \mathrm{MPa}$ and a Poisson's ratio of $\nu = 0.45$. This is a major simplification, since in liquid-crystal elastomers usually both

quantities are inhomogeneous and anisotropic [54, 98, 99] and heavily depend on the temperature [100]. However, the simplification is justified by the good agreement of the model with the measured data. The thermal expansion of the constituent material is assumed to be anisotropic and the model takes the measured values shown in Figure 28 as input. An initial anisotropic shrinkage of $-14.2\ \%$ perpendicular to the director is assumed to model the shrinkage of the samples during development. This value agrees with the measured shrinkage as presented in section 3.5.

For the conversion of the LED light to heat, I employed a simplified model assuming a spatial heat source Q

$$Q(z) = Q_0 e^{-\alpha z}. \tag{200}$$

Here, z measures the distance to the active surface of the LED, while Q_0 is proportional to the intensity of the LED. The exponential decay is justified by the decrease of the LED light with increasing distance to the LED surface as shown in Figure 33*d* and due to the absorption of the light by the material itself (Beer's law). With this assumption the temperature within an illuminated metamaterial is governed by the heat equation

$$\lambda \frac{\partial^2 T}{\partial z^2} = Q_0 e^{-\alpha z}. \tag{201}$$

For a homogeneous cuboid with a height h whose temperature is fixed to room temperature T_R at the bottom and the top, the resulting temperature profile is given by

$$T(z) = \frac{T_\mathrm{p} - T_\mathrm{R}}{f_1} \times \left(e^{-\alpha z} - 1 - (e^{-\alpha h} - 1) \times \frac{z}{h} \right) + T_\mathrm{R} \tag{202}$$

with

$$f_1 = e^{-\alpha z_\mathrm{p}} - 1 - (e^{-\alpha h} - 1) \times \frac{z_\mathrm{p}}{h} \tag{203}$$

and

$$z_\mathrm{p} = -\frac{1}{\alpha} \ln\left(\frac{1 - e^{-\alpha h}}{\alpha h} \right). \tag{204}$$

Here, T_p is the peak temperature depending linearly on Q_0 that is reached at position z_p within the sample.

For the metamaterials, I assumed the same temperature profile with an effective parameter α that also accounts for the geometry of the sample. I obtained good agreement with the experiments assuming $\alpha = 2/845\ \mu\mathrm{m}^{-1}$.

Since T_p depends linearly on Q_0 it also depends linearly on the intensity of the LED light. On the other hand, the intensity of the LED depends roughly linearly on the LED current according to Figure 33*e*. Therefore, I assumed a linear relationship between the peak temperature T_p within the sample and the electrical current I applied to the LED. The factor relating both quantities depends on the geometry of the sample and the concentration of dye within the polymer and is therefore different for the metamaterials discussed in this chapter. I chose the factors such, that the computed results of the Poisson's ratio or the twist per strain of the metamaterials fitted best to the experimentally obtained values. For the metamaterial discussed in section 4.4 the peak temperature is given by

$$T_\mathrm{p} = 135\frac{\mathrm{K}}{\mathrm{A}} \times I + T_\mathrm{R} \tag{205}$$

while it is given by

$$T_\mathrm{p} = 175\frac{\mathrm{K}}{\mathrm{A}} \times I + T_\mathrm{R} \tag{206}$$

for the metamaterial discussed in section 4.5.

To obtain the deformed geometry of a metamaterial that results from the shrinkage, the thermal expansion and certain boundary conditions like an applied displacement, I employed the structural mechanics module in COMSOL Multiphysics. The software uses a finite-element algorithm to solve the equations of motion of continuum mechanics. Due to the large strains appearing during the thermal expansion, I took account of geometrical non-linearities by solving the general form of the equations of motion of continuum mechanics and not the linearized equations. I repeat the relevant set of equations (207)-(213) here. See section 2.4 for further information.

$$\nabla \cdot \left(\boldsymbol{F}\tilde{\boldsymbol{S}}\right)^\mathrm{T} = 0 \tag{207}$$

$$\boldsymbol{F} = \boldsymbol{I} + \frac{\partial \vec{u}}{\partial \vec{X}} \tag{208}$$

$$\boldsymbol{E}_\mathrm{el} = \frac{1}{2}\left[\boldsymbol{F}_\mathrm{el}^\mathrm{T}\boldsymbol{F}_\mathrm{el} - 1\right] \tag{209}$$

$$\boldsymbol{F}_\mathrm{el} = \boldsymbol{F}\boldsymbol{F}_\mathrm{th}^{-1} \tag{210}$$

$$\boldsymbol{F}_{\mathrm{th}} = \left(\Lambda_{\parallel}\big(T(Z)\big) - \Lambda_{\perp}\big(T(Z)\big)\right)\vec{n}\vec{n}^{\mathrm{T}} + \Lambda_{\perp}\big(T(Z)\big)\boldsymbol{I} \tag{211}$$

$$\widetilde{\boldsymbol{S}} = \det(\boldsymbol{F}_{\mathrm{th}})\,\boldsymbol{F}_{\mathrm{th}}^{-1}(\boldsymbol{C}:\boldsymbol{E}_{\mathrm{el}})\boldsymbol{F}_{\mathrm{th}}^{-\mathrm{T}} \tag{212}$$

$$C_{IJKL} = \frac{Y\nu}{(1+\nu)(1-2\nu)}\delta_{IJ}\delta_{KL} + \frac{Y}{2(1+\nu)}\left(\delta_{IK}\delta_{JL} + \delta_{IL}\delta_{JK}\right) \tag{213}$$

More details on the finite-element calculations are given in the following two sections that discuss the two 3D optomechanical metamaterial examples presented in this chapter.

4.4 Auxetic Metamaterial

In this section, I present a 3D optomechanical metamaterial that changes its Poisson's ratio according to the light intensity of a blue LED irradiating it. The geometry of the unit cell is depicted in Figure 34*a* together with the intended director field. The depicted unit cell represents the printed geometry. However, due to an anisotropic shrinkage during development, the unit cell changes its shape during development. Figure 34*b* shows a cut through the developed unit cell at room temperature. Heating the unit cell to 200 °C leads to the deformed geometry depicted in Figure 34*c*.

Pushing on the unit cell at room temperature increases the lateral extent of the unit cell. In contrast, pushing on the unit cell at an elevated temperature of 200 °C leads to a decrease of the lateral extent. According to these results, a metamaterial built from these unit cells would show a positive Poison's ratio at room temperature and a negative Poison's ratio at elevated temperatures.

Figure 34*d* shows an optical microscope image of a printed and developed metamaterial comprising $3 \times 3 \times 5$ unit cells. The liquid-crystal elastomer appears colourless before the dyeing of the metamaterial. After dyeing of the metamaterial, it appears red as depicted in Figure 34e. The red colour nicely illustrates that dye has infiltrated the polymer network. A scanning electron micrograph of the metamaterial is shown in Figure 34f. The shape of the unit cells appears to be close to the expected shape, indicating a correct director distribution.

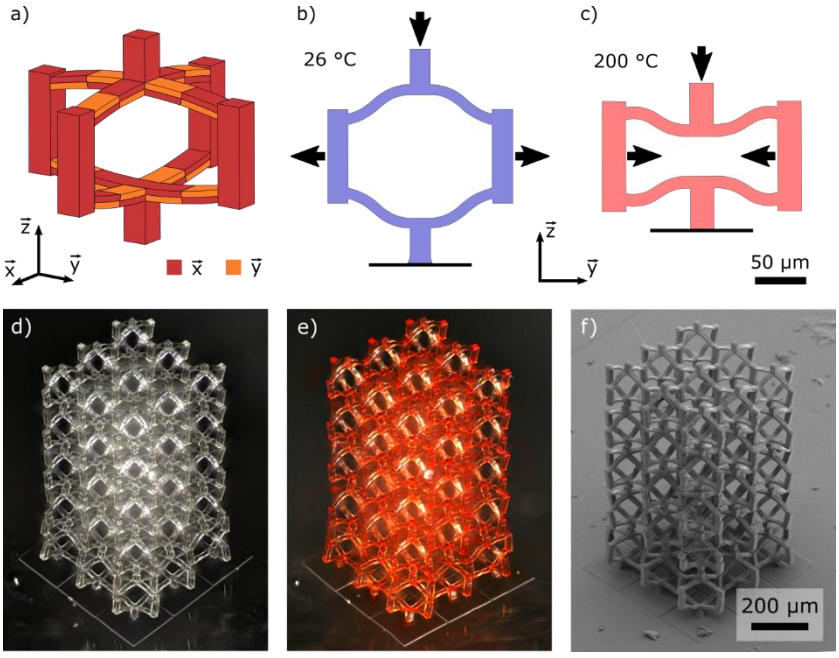

Figure 34. 3D optomechanical metamaterial with variable Poisson's ratio. (a) Design of the unit-cell as printed including two different director orientations. (b) Cut through the developed unit cell at room temperature obtained by a finite element calculation. The shape differs from the printed design due to anisotropic shrinkage during development. The application of an axial strain leads to a horizontal expansion of the unit cell. A metamaterial built from this unit cell shows a positive effective Poisson's ratio at room temperature. (c) Cut through the same unit cell at $200\ °C$*. The application of an axial strain leads to a horizontal contraction. A metamaterial built from the presented unit cell shows a negative effective Poisson's ratio at* $200\ °C$*. (d) Optical microscope image of a printed and developed metamaterial built from* $3 \times 3 \times 5$ *unit cells. The sample appears transparent with a white colour. (e) Optical microscope image of the same sample after dyeing with disperse red 1. The red colour proofs that the dye is fixed to the polymer. (f) Scanning electron micrograph of the same sample. Figure is partially adapted from [93] (CC BY 4.0).*

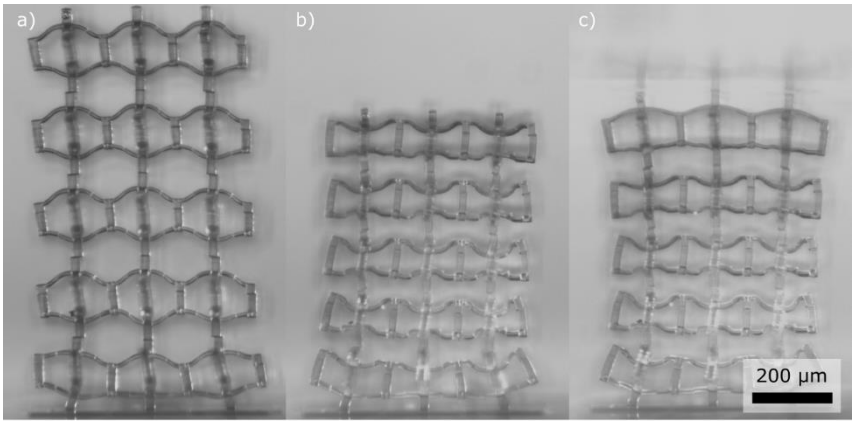

Figure 35. Light microscope images showing the side of the first metamaterial example mounted in the characterisation setup in different configurations. (a) The blue LED is turned off. The cells of the metamaterial show the expected shape at room temperature. (b) The blue LED is biased with a current of $1.5\ A$*. The unit cells show the expected shape at elevated temperatures for the top four rows. (c) The blue LED is biased with a current of* $1.5\ A$*. However, a glass sheet is in contact with the top of the sample. The top row of unit cells is much less deformed than without the glass sheet, indicating a much lower temperature there.*

To study the deformation of the printed metamaterial upon optical irradiation with the blue LED, I mounted the sample in the characterisation setup described in section 4.2. Figure 35 shows optical microscope images in different configurations. In Figure 35*a,* the LED is turned off while in Figure 35*b* the LED current is $1.5\ \mathrm{A}$. In both configurations there is no glass sheet in contact with the top of the sample. The unit cells behave as described in Figure 34*b* and Figure 34*c*. This is another strong indicator that the director profile within the printed sample is close to the design. In Figure 35*c* the LED current is also set to $1.5\ \mathrm{A}$, but a glass sheet is in contact with the top of the metamaterial sample. This leads to a reduced actuation at the top of the sample compared to Figure 35*b*, indicating that the temperature is near room temperature there.

Overall, the printed metamaterial looks as expected after development and deforms as expected. Both points are strong indicators that the director profile of the constituent liquid-crystal elastomer is close to the design.

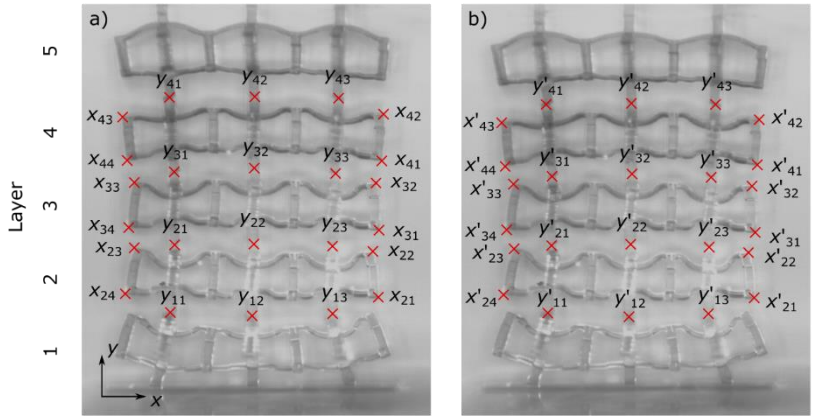

Figure 36. Light microscope images of the first metamaterial example recorded in the characterisation setup. The blue LED is biased with an electrical current of $1.5\ A$*. A glass sheet is in contact with the top of the sample. (a) No strain is applied to the sample. The red crosses mark the positions that are tracked by image cross-correlation. The crosses are labelled* x_{ij} *and* y_{ij}*. Thereby, the index* $i = 1 \dots 4$ *labels the row of unit cells, while* j *enumerates the labels within one row. (b) A strain of* $3\ \%$ *is applied to the metamaterial. The crosses labelled with a primed label mark the positions that correspond to the unprimed markers. The position of the primed markers is obtained via image cross-correlation. Figure taken from [93] (CC BY 4.0).*

In a further step, I studied how the Poisson's ratio of the metamaterial sample depends on the LED current. Therefore, I mounted the sample in the characterisation setup described in section 4.2 and performed the following steps to measure the Poisson's ratio for a given value of the LED current. First, I applied the desired electrical current to the blue LED leading to a deformation of the sample. After the deformation, I manually moved the sample with a linear stage towards the glass sheet (see section 4.2) until the top of the sample touched the glass sheet. In this unstrained configuration, I recorded an optical microscope image of the sample in side view. An example is depicted in Figure 36*a*. Next, I applied a strain of about $3\ \%$ via the computer-controlled stage and took an optical microscope image in side view. This image represents the strained configuration. An example is depicted in Figure 36*b*. To quantify the deformation caused by the applied strain, I manually placed markers in the microscope image in the unstrained case as depicted in Figure 36*a*. Via image cross-correlation, I searched for the corresponding positions in the microscope image of the strained configuration as depicted in Figure 36*b* . With this information, I calculated the width b_i and the height h_i of the

individual layers $i = 2,3,4$ of the metamaterial sample in the strained and unstrained configuration according to

$$h_i = \frac{1}{3}\sum_{j=1}^{3}\left(y_{ij} - y_{i-1,j}\right) \tag{214}$$

and

$$b_i = \frac{1}{2}[(x_{i1} + x_{i2}) - (x_{i3} + x_{i4})]. \tag{215}$$

From the width b_i and height h_i, I assigned a Poissons's ratio ν_i to the individual layers as defined by

$$\nu_i = -\frac{b_i - b_i'}{b_i} \cdot \frac{h_i}{h_i - h_i'} \tag{216}$$

(see section 2.4.3). The Poisson's ratio of the individual layers differs mainly due to an inhomogeneous temperature profile within the sample caused be the LED. Furthermore, I calculated a mean Poisson's ratio of the full sample using

$$\nu_{\mathrm{mean}} = -\frac{\frac{1}{3}\sum_{i=2}^{4}(b_i - b_i')}{\frac{1}{3}\sum_{i=2}^{4} b_i} \cdot \frac{\sum_{i=2}^{4} h_i}{\sum_{i=2}^{4}\left(h_i - h_i'\right)} \tag{217}$$

In the experiment, I swept the LED current four times from zero to $1.5\ \mathrm{A}$ in steps of $0.15\ \mathrm{A}$. The resulting Poisson's ratios for the individual layers $i = 2,3,4$ and the mean Poisson's ratio are depicted in Figure 37*a* versus the LED current for every run. Additionally, the average over the individual results of the four runs for every LED current is given. The mean Poisson's ratio averaged over the four runs is 0.47 for no LED current and decreases monotonically to -0.27 at an LED current of $1.5\ \mathrm{A}$. This especially means that the Poisson's ratio flips its sign on illumination for an LED current of above roughly $1\ \mathrm{A}$. Furthermore, a good repeatability and reversibility are observed in the four individual runs.

To further deepen my understanding, I performed finite element calculations with the aim to reproduce the measured Poisson's ratio. Therein, I modelled the constituent material and the temperature profile within the sample for a given LED current as described in section 4.3. To reproduce the experimental Poisson's ratios, I had to slightly modify the director distribution within the unit cell compared to the designed distribution. The updated director distribution is depicted in Figure 37*d*, where a layer is now slightly bended upwards. This bending of a layer within the bottom bar is also visible in

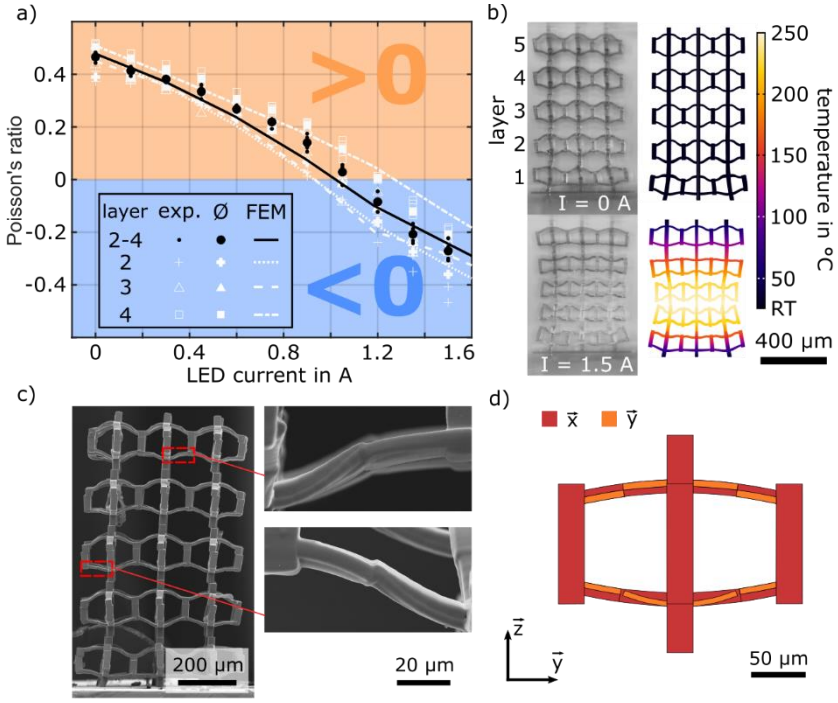

Figure 37. (a) The Poisson's ratio averaged over the three central layers is depicted by small black dots versus the LED current. The average over the four individual measurements for every current is depicted by large black dots. The results from finite element calculations (FEM) are represented by a black solid curve. The respective results for the individual layers of the metamaterial are indicated by white symbols (see legend). The Poisson's ratio flips its sign from positive to negative with increasing LED current. (b) Compares light microscope images of the metamaterial to calculated geometries for LED currents of zero and 1.5 A. The calculated temperature profile is plotted in false colours. (c) Scanning electron micrograph of the metamaterial. The insets show two different bars with printing artefacts. The two layers building a bar are not perfectly stacked. (d) Shows the design of the unit cell used for the finite element calculations. The design models the observed printing artefacts. Figure is partially adapted from [93] (CC BY 4.0).

the scanning electron micrograph in Figure 37*c*. The reason for this bending is a shrinkage that occurs during polymerization of the layer printed on top.

My strategy to obtain the Poisson's ratio in the finite element calculations was similar to the experiment. In a first step, I calculated the deformed geometry for a certain LED current while the bottom plate of the metamaterial sample was fixed. The result represents the unstrained configuration. In the unstrained configuration, I probed for the height of the geometry. With this information, I performed a second calculation with an additional strain of $3\ \%$ applied to the top of the sample. The result of this calculation represents the strained configuration. In both configurations, I probed for the same points as in the experiment (see Figure 36) and calculated the Poisson's ratio for the individual layers and the mean Poisson's ratio according to equations (216) and (217).

The resulting Poisson's ratios versus the LED current are plotted in Figure 37*a* in addition to the experimental data. The resulting curves agree well with the measured data. Furthermore, Figure 37*b* shows the calculated unstrained configurations for no LED current and an LED current of $1.5\ \mathrm{A}$. The calculated temperature profile is depicted in false colours. The calculated geometries are compared to light microscope images recorded at the respective LED currents. The shape of the metamaterial sample in the experiment matches well to the calculated geometry for both currents.

In conclusion, the Poisson's ratios in the finite element calculations agree well with the measured Poisson's ratio as well as the observed deformations match with the calculated geometries. From that, I conclude that the finite element model describes the printed samples well.

To further study the reversibility and repeatability of the light induced deformation, I performed another experiment. I mounted a new but nominally identical sample to the characterisation setup. Next, I performed 100 illumination cycles. In each cycle, the LED is turned on with an electrical current of $1\ \mathrm{A}$ for 1 second and turned off for 3 seconds. To observe the deformation of the sample, I recorded a video with 70 frames per second with the optical microscope observing the side of the sample. In every frame of the resulting video, I extracted the height of the sample via image cross-correlation. From the recovered height information, I calculated the strain of the sample in each frame with respect to the height in the first frame, where the LED is turned off and the sample is unstrained. The resulting strain over the 100 illumination cycles is plotted versus time in Figure 38*d*.

In each cycle, the strain repeatably reaches $21\ \%$, however, the sample does not recover to the same height. After the first cycle, the sample recovers to a height that is $0.4\ \%$ smaller than before. After every following cycle, the sample recovers to a height that is $0.01\ \%$ smaller than the height at the beginning of the cycle. This might be due to plastic or viscoelastic deformations due to high local strains. A finite element

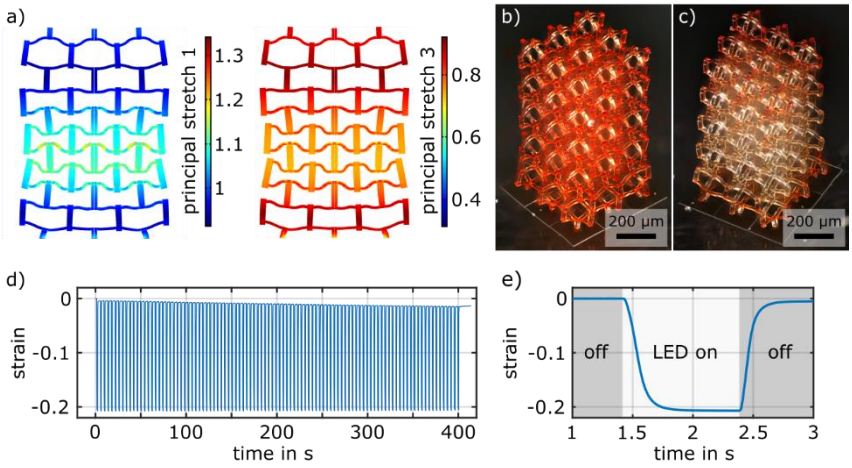

Figure 38. (a) A cut through the metamaterial at an LED current of 1.5 *A. The first and third principal stretch is plotted in false colours. (b) Optical microscope image of the dyed metamaterial before any illumination with the blue LED. (c) Optical microscope image of the same sample after the measurement of the Poisson's ratio. In total the sample was illuminated for about* 25 *minutes. (d) Measured strain of the metamaterial versus time during 100 cycles of illumination. In every cycle the LED is biased by* 1 *A for one second and turned off for three seconds afterwards. (f) A zoom into the first cycle of illumination. Figure is adapted from [93] (CC BY 4.0).*

calculation shows that the local strains reach values up to 60 %. Figure 38*a* shows the first and third principal stretch in a cut through the metamaterial sample and illustrate the positions where the large strains occur. These high strains might be mitigated with a more careful design. However, even after 100 cycles, the irreversible effects are small compared to the overall actuation of the metamaterial.

Figure 38*e* shows a zoom into the first cycle of illumination and allows to extract the actuation times and recovery times. For this cycle, I extracted an actuation time of 75 ± 1 ms and a recovery time of 63 ± 2 ms. These times can in principle be different because they rely on different mechanisms. During the actuation, the light is converted to heat in the volume and therefore the actuation time depends on the efficiency of the conversion from light to heat and the intensity of the incident light. For the recovery the heat must be conducted through the volume of the sample to the surrounding and therefore depends only on the heat conductivity of the sample.

To verify the role of the dye during the actuation of the sample with light, I tried to actuate a sample without dye. For an LED current of $1\ \mathrm{A}$, I obtain a 400 times reduced strain with respect to the samples that contain the absorber dye. This proofs that the dye is the main converter of light to heat in the system.

The importance of the dye for the light absorption also means that bleaching of the dye is another mechanism that limits the repeatability. Figure 38*b* depicts the sample used to measure the poisons ratios before the experiment and Figure 38*c* shows the sample after the measurement. The bleaching of the dye is clearly visible after an illumination time of about 25 minutes during the experiment. The bleaching seems to be strongest at the second and third layer. I also expect these layers to be hottest during the experiments. This indicates that the bleaching of the dye might be due to thermal decomposition. According to the work of Nguyen *et al.* [101] the dye thermally decomposes at a rate of about $5\ \%\ \mathrm{min}^{-1}$ at a temperature of $250\ ^\circ\mathrm{C}$, which would result in a decomposition of about $72\ \%$ of the dye in 25 minutes. To recover the dye, the sample could in principle be re-infiltrated with dye.

In conclusion, I have presented a 3D optomechanical metamaterial with a tunable Poisson's ratio made from liquid-crystal elastomer incorporating two different director orientations. The structures showed to work nearly repeatably and reversible for many cycles.

4.5 Chiral Metamaterial

In this section, I present a second 3D optomechanical metamaterial made from liquid-crystal elastomer that responds with a twist to an axial strain. The twist depends on the intensity of a blue LED and even changes its sign for a large enough intensity.

In the design of the unit cell of the metamaterial, I was supported by Franziska Fürniß. Within the frame of her master thesis, she developed an early version of the unit cell under my guidance. The unit cell developed by Franziska was initially inspired by the work of Frenzel *et al.* [14, 15] and is the basis of the unit cell presented here.

The geometry of the unit cell is depicted in Figure 39*a*. It consists of chiral motifs on the faces of a cube consisting of a central cylindrical plate and four bi-layered arms connected to it. The arms of each motif are connected at the corners of the cube with spheres. In the horizontal direction the unit-cells are connected via bars attached to the cylindrical plates. Vertically, the cylindrical plates of adjacent unit cells are directly connected.

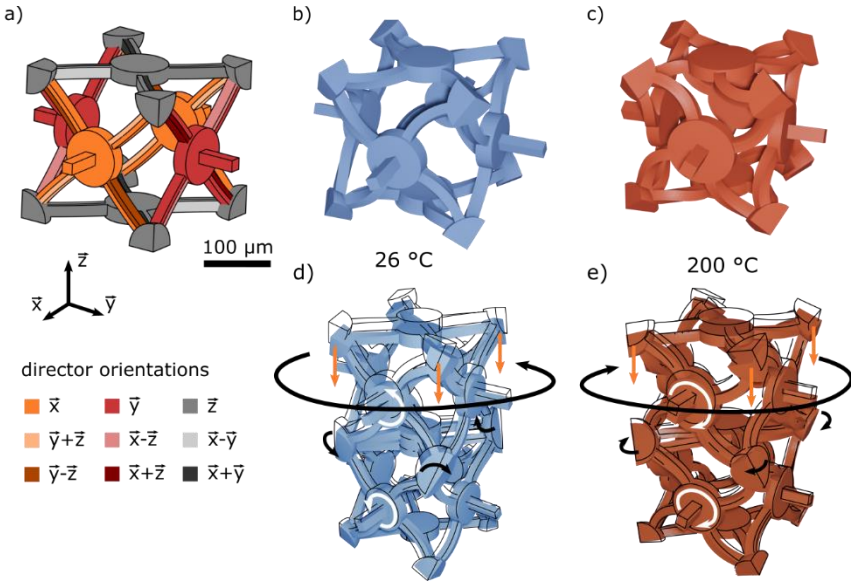

Figure 39. (a) Chiral unit cell design as printed. It comprises nine different director orientations indicated by the different colours. (b) The shape of the unit cell at room temperature differs from the printed structure due anisotropic shrinkage during development. (c) The same unit cell changes its handedness at elevated temperatures. (d) Application of an axial strain (orange arrows) leads to a counter clockwise twist. Due to the chirality, the central plates rotate (white arrows) leading to a tilt of the corners (black arrows). The tilt of the corners rotates the unit cell on top. (e) At elevated temperatures the unit cell twists in the clockwise direction due to the flip of the handedness. Figure partially adapted from [93] (CC BY 4.0).

The different colours in Figure 39*a* indicate the director orientation of the liquid-crystal elastomer. In total, nine different director orientations are included in the design. Each arm in the chiral motifs consists of two layers with a director tangential to the arm in one layer and perpendicular to the respective face of the cube in the other layer. The bi-layered arms perform a geometry transformation of the unit cell upon irradiation. The director orientations are chosen such, that the chiral motifs change their handedness upon irradiation.

Due to the anisotropic shrinkage of the constituent liquid-crystal elastomer during development (see section 3.5), the developed structure is expected to look different than the designed structure that was used for printing. The expected shape of the printed

unit cell after shrinkage is presented in Figure 39*b*. Upon heating, the unit cell changes its handedness as depicted in Figure 39*c*. The images were obtained via finite element calculations as described in section 4.3.

The response of the unit cell upon an axial strain is illustrated in Figure 39*d* at room temperature and in Figure 39*e* at elevated temperatures. The axial strain is indicated via orange arrows in both images. Due to the chirality of the motifs on the sides of the unit cell, the central plates start to rotate as indicated by the white arrows. For a non-chiral design, this would not be the case due to symmetry reasons. Due to the rotation of the central plates, the corners of the unit cell start to tilt counter-clockwise at room temperature and clockwise at elevated temperatures, as illustrated by the black arrows. The result is a rotation of the unit cell that is on top of the observed unit cell. Therefore, a metamaterial consisting of the presented unit cell responds with a twist upon an axial strain.

The twisting motion upon an axial strain is a problem for a real measurement, since pushing on the top and the bottom of a sample usually permits sliding boundary conditions. This would result in a suppression of the twisting motion. A solution to this problem was suggested in [14]. There, two structures are combined with opposite handedness, which cancels the twisting motion at the bottom and the top of the sample. The twist is then measured at the middle of the overall sample. Following this idea, I printed a sample consisting of $2 \times 2 \times 2$ unit cells on the bottom with a certain handedness and $2 \times 2 \times 2$ unit cells with the opposite handedness on top. Both parts of the sample are separated by a central plate. The twist per strain is directly related to the rotation of the central plate. The top and bottom of the sample are also equipped with a plate.

A scanning electron micrograph of the printed and developed sample is depicted in Figure 40*b.* Due to the restrictions induced by the plates, it is not easy to tell what shape is expected after development of the printed sample. For this reason, Figure 40*a* depicts the shape of the designed sample after shrinkage calculated by the finite element approach presented in section 4.3. The calculated geometry agrees well with the printed structure, which indicates that the director profile is as designed within the printed sample.

The optical microscope image of the printed sample in Figure 40*c* shows a red colour. The red colour indicates that the dye has been successfully infiltrated into the polymer.

Figure 40*d, e* and *f* show optical microscope images of the printed sample mounted in the characterisation setup described in section 4.2. In Figure 40*d* the LED current is zero, while in Figure 40*e* the LED current is $1.05\ \mathrm{A}$. In both configurations the glass sheet is

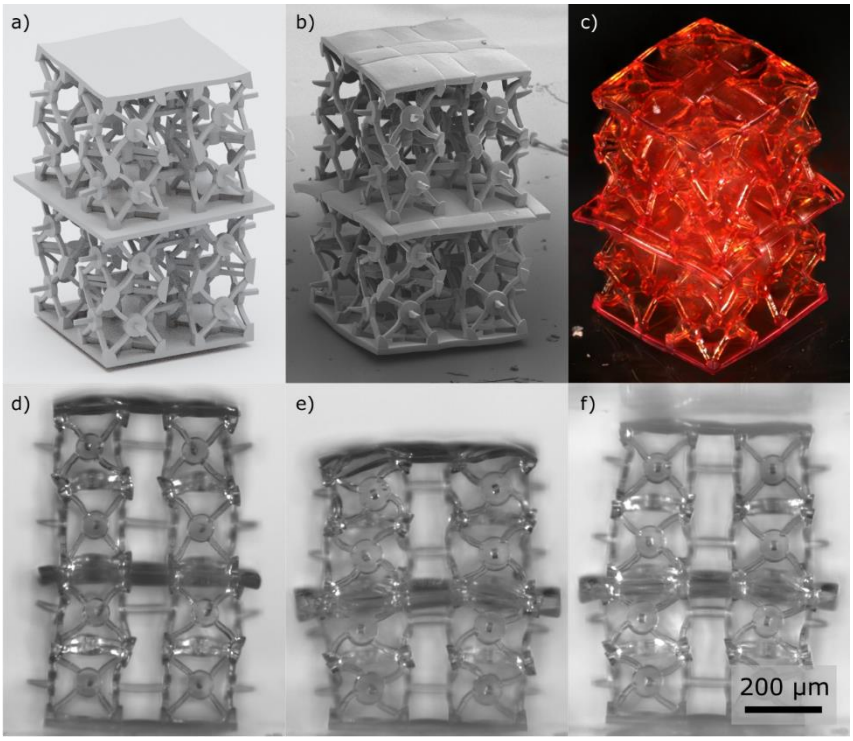

Figure 40. (a) Calculated shape of the metamaterial after anisotropic shrinkage. (b) Scanning electron micrograph of the printed metamaterial. The shape of the metamaterial agrees with the calculation. (c) Optical microscope image of the metamaterial. The red colour is caused by the infiltrated dye. (d) Optical microscope image of the printed metamaterial mounted in the characterisation setup. The LED current is zero. (e) Same as (d) but with an LED current of $1.05\ A$*. The handedness of the unit cells flipped as expected. (f) Same as (e) but with a glass sheet touching the sample at the top. The actuation at the top is reduced indicating a reduced temperature there. Figure partially adapted from [93] (CC BY 4.0).*

not in contact with the sample. It is visible, that the unit cells change their handedness upon irradiation. In Figure 40*f*, the LED current is also set to $1.05\ \mathrm{A}$, however, the glass sheet is in contact with the top of the sample. The lack of deformation at the top of the sample indicates that the temperature of the sample is close to room temperature at the top.

Overall, the printed sample shows the expected shape after development and the unit cells change their handedness upon irradiation. This is a strong indicator that the director field of the constituent liquid-crystal elastomer is as designed.

To characterize the sample with respect to twist per strain versus the intensity of the LED, I mounted the sample in the characterisation setup described in section 4.2. The measurement procedure is equivalent to the procedure described in section 4.4. First, I applied a certain current to the LED. The light of the LED immediately triggers a deformation of the sample. After the deformation of the sample, I manually moved the sample towards the glass sheet until the top of the sample touched the glass sheet. In this unstrained reference configuration, I recorded an image from the top of the central plate and the side of the sample. Afterwards, I applied a strain of about $1.8\,\%$ via the computer-controlled stage and took an image from the top of the central plate and the side of the sample in the strained configuration. In the end, I released the strain and turned off the LED.

To calculate the twist per strain, the rotation of the central plate and the applied strain must be extracted. Both are extracted from the recorded images via image cross-correlation. To measure the rotation, I manually placed markers at the corners of the central plate in the image of the unstrained configuration. Via image cross-correlation, I calculated the corresponding markers in the image of the strained configuration. From the displacement of the corners, I calculated the rotation of the central plate. To extract the applied strain, I manually placed markers at the top and bottom corners of the sample in the side-view image in the unstrained configuration. Again, I calculated the corresponding markers in the side-view of the strained configuration via image cross-correlation. From the displacement of the markers, I calculated the axial strain applied to the sample. In the end, I divided the rotation angle of the central plate by the applied axial strain and divided the result by two, to obtain the twist per strain per unit cell.

To characterize the sample, I performed four runs sweeping the LED current in each run from zero to $1.05\,\mathrm{A}$ in steps of $0.15\,\mathrm{A}$. Figure 41*a* shows the measured twist per strain versus the LED current for the four runs together with a mean over the four runs for every LED current. The measured twist per strain increases up to an LED current of $0.45\,\mathrm{A}$ and then rapidly decreases until it has a negative sign for an LED current of $0.75\,\mathrm{A}$. The variation in between the runs might be partly due to viscoelastic or plastic deformations or even fractures due to large local strains, as discussed below.

To further deepen my understanding, I calculated the twist per strain versus the LED current via finite element calculations (see section 4.3). These finite element calculations were performed similar to the experiment.

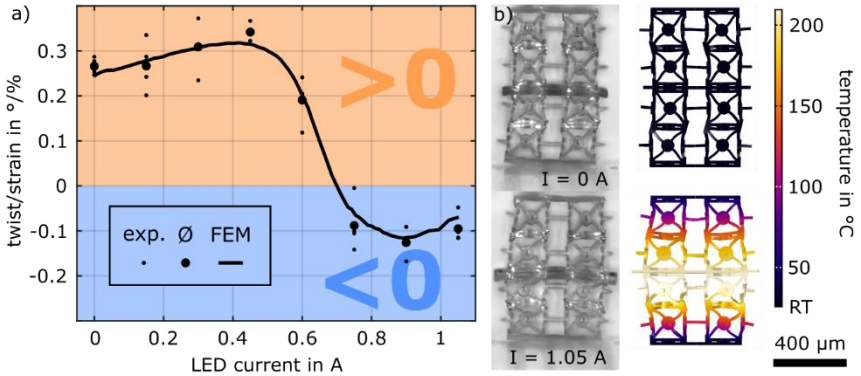

Figure 41. (a) The measured twist per strain is indicated by small dots for different LED currents. The average over the four individual measurement for every LED current is represented by large dots. The calculated twist per strain is plotted as a solid curve. (b) Compares the light microscope images of the printed sample to calculated geometries for LED currents of zero and $1.05\ A$*. Thereby, the calculated temperature is indicated in false colours. Figure adapted from [93] (CC BY 4.0).*

First, I applied a displacement of $20\ \mu m$ perpendicular to the outer boundary of the bottom plate to mimic the partial detachment of the bottom plate observed in the electron micrograph in Figure 40*b*. Then, I calculated the temperature profile according to section 4.3 corresponding to a certain LED current. With that temperature profile, I calculated the deformed geometry and probed for the average height of the deformed geometry. In a second step, I used the obtained height information to additionally apply an axial strain of $1.8\ \%$ to the sample and probed for the resulting rotation of the central plate and calculated the twist per strain similarly to the experiment. The resulting twist per strain is plotted as a solid curve together with the experimental data in Figure 41*a*. The calculated data agrees well with the measured values.

Figure 41*b* compares the measured unstrained configurations to the unstrained configurations obtained by the finite element calculation. The calculated temperature profile is indicated in false colours. The calculated shape of the structures agrees well with the recorded optical microscope images.

From the good agreement of the calculated twist per strain and the measured twist per strain together with the good agreement of the calculated geometry and the experimentally observed geometry for different LED currents, I conclude that the presented finite element model describes the metamaterial well.

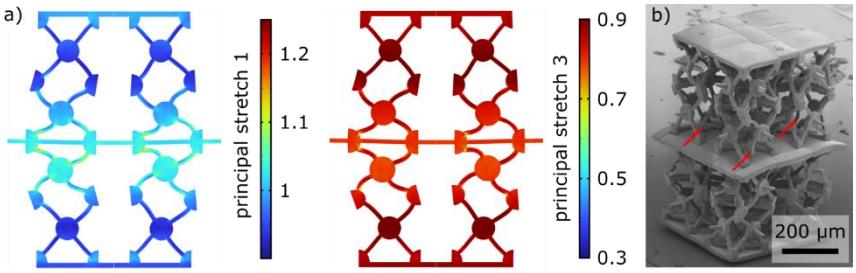

Figure 42. (a) Shows cuts through the metamaterial at an LED current of $1.05\ A$*. The first and third principal stretch are depicted in false colours. High strains are present at the corners of the unit cells close to the central plate. (b) Scanning electron micrograph of the metamaterial sample showing fractured beams at the positions of high strain close to the central plate.*

As mentioned above, the variation between the runs in the measurement of the twist per strain might be due to viscoelastic or plastic deformations or even fractures caused by large local strains. To further investigate this, I calculated the principal stretches via finite element calculations. The calculations show that locally, the material expands up to $40\ \%$ and gets compressed up to $90\ \%$. Figure 42*a* and *b* depict the first and third principal stretch in a slice of the metamaterial in false colours for an LED current of $1.05\ \mathrm{A}$. It is visible that the large strains appear at the corners of the unit cells close to the central plate, since there the temperature is highest. Due to the high strains appearing during illumination, it is plausible that plastic or viscoelastic deformations occur. The scanning electron micrograph depicted in Figure 42*c* even shows three fractured bars located at the positions of high strain as indicated by the red arrows. It is plausible that such irreversible deformations irreversibly change the behaviour of the overall sample. Maybe, this could be avoided with a more careful design of the unit cell.

As already found by other researchers, the twist per strain depends on the number of unit cells in the footprint of the metamaterial. The twist per strain is expected to vanish in the limit of an infinite number of unit cells in the footprint of the metamaterial. [14, 15]. However, studies on similar unit cells have shown, that there is first an increase in the twist per strain versus the number of unit cells until it reaches a maximum and decreases from there to zero. To study the behaviour of the presented metamaterial with respect to the sample size, I performed finite element calculations for zero LED current and a varying sample size with a footprint of $N \times N$ unit cells with

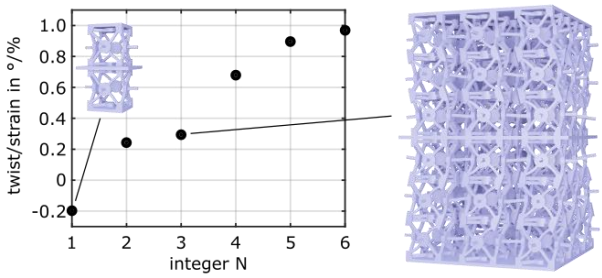

Figure 43. Twist per strain calculated for metamaterials with $N \times N \times 2N$ unit cells. The twist per strain increases up to $N = 6$. The insets show the geometries for $N = 1$ and $N = 3$ including the anisotropic shrinkage. The case $N = 2$ represents the metamaterial sample discussed in this section. Figure taken from [93] (CC BY 4.0).

$N \leq 6$. The resulting twist per strain is plotted in Figure 43 versus the integer N. The twist per strain is increasing monotonously. Therefore, the maximum twist per strain must appear for $N \geq 6$. It is prominent, that the twist per strain is negative for $N = 1$. I assume that this is caused by the top, bottom and central plate that restrict the shrinkage of the unit cells.

In conclusion, I have presented a chiral metamaterial with a tunable twist per strain printed from liquid-crystal elastomer incorporating nine different director orientations. The twist per strain of the measured samples together with the geometries for different LED current agree well with the finite element calculations, suggesting that the presented model describes the reality well. Variations of the measured twist per strain might be due to irreversible deformations caused by large strains. This might be avoided by a more careful sample design.

A discussion of the obtained results is given in the next chapter.

5 Chapter 5
Discussion and Conclusion

Many applications in everyday life already employ materials with tuneable properties. Examples are liquid crystals in displays where the orientation of the optic axis is tuned via electric fields, or piezoelectric crystals that contract or expand in response to electric voltages. However, the palette of tuneable materials offered by nature is limited and does not cover all conceivable applications. Responsive metamaterials promise a route to enhance this palette with all kinds of tuneable effective parameters.

To create such 3D responsive materials, I developed a novel 3D laser microprinting technique. This technique allows to print complex 3D architectures from liquid-crystal elastomer with feature sizes in the range of a few micrometres and an overall sample size that can be in the millimetre range. Almost all liquid-crystal director orientations can be printed, with the freedom to choose the director independently and in situ at every voxel location.

For the alignment of the director, I designed and fabricated a custom electrode that permits high electric fields on the order of $1\ \mathrm{V}\cdot\mu\mathrm{m}^{-1}$ and an arbitrary orientation of the electric field vector in the focal plane of the objective lens during the printing process. With the help of Dominik Beutel, I demonstrated that manipulations of the printing laser polarisation suffice to confine the laser focus for a large range of director orientations, despite the highly birefringent photoresin. I used an azimuthal polarisation when printing vertical director orientations and a linear polarisation for all other director orientations. Changing the director orientation during the printing requires a photoresin that is liquid. This is in contrast to many other 3D laser microprinting approaches presented in the literature [47–57]. The novel resin I developed, polymerizes to a liquid-crystal elastomer that shows a large, fully reversible and repeatable thermal expansion.

As already pointed out in chapter 3, the 3D laser microprinting technique described in this thesis is to my knowledge the only technique published so far that allows to print complex 3D architectures with a free choice of the director orientation at any point in space. This development is an essential prerequisite for printing 3D optomechanical metamaterials.

In chapter 4, I presented two examples of such 3D optomechanical metamaterials that allow tuning an effective parameter on a large range with the light of an LED. In the first example, the Poisson's ratio can be tuned from 0.47 to -0.27 using intensities up to $30\ \mathrm{W \cdot cm^{-2}}$. The measured effective Poisson's ratios agree well with those obtained from finite element calculations. The metamaterial showed a good reversibility and repeatability in 100 cycles. The response time for actuation and recovery was below $100\ \mathrm{ms}$ in this experiment.

The second responsive metamaterial is a chiral metamaterial that shows a tuneable twist angle when strained. The twist per strain can be adjusted between -0.1 and 0.3 using intensities up to $25\ \mathrm{W \cdot cm^{-2}}$. The measured values for the twist per strain agree well with the values obtained from finite element calculations.

Looking into the literature, there are already many examples for stimuli responsive metamaterials [32–46]. However, they were either effectively two-dimensional [37–42, 44, 46], macroscopic models [32–44, 46] or show a narrow parameter tuning range [45]. The responsive metamaterials presented in this thesis are to my knowledge the first that are three-dimensional, with feature sizes on the micrometre scale, and with effective properties that are tuneable on a large range. Beyond that, they represent to my knowledge by far the most complex 3D structures fabricated from liquid-crystal elastomer published in literature until now.

Although this thesis represents a great step forward in the field of responsive metamaterials, further work has to be done to increase the number of unit cells of the printed metamaterials, which is currently limited by the speed of the printer. With further improvement in this regard, I envision that many more 3D optomechanical metamaterials can be designed and fabricated along the routes I have presented. For example, I could imagine a chiral optomechanical metamaterial showing tuneable acoustical activity [16]. There, the linear polarisation of a transverse elastic wave would be rotated by an angle that depends on an external light source.

Further work could also be spent on the composition of the liquid-crystal resin. In the literature, liquid-crystal elastomers are reported that show similar strains as those reported in this thesis, however using temperature swings of $10\ ^\circ\mathrm{C}$ starting at room

temperature [102]. If such materials could be made compatible with the 3D laser microprinting technique I developed in this thesis, the tuning of 3D optomechanical metamaterials with sunlight might become possible.

Another route to follow could be to fabricate responsive metamaterials that simultaneously respond to several stimuli in a controlled fashion. For, example, one could think about structures that respond to humidity [48] and light at the same time.

I want to close this discussion with the thought that the methods developed in this thesis might not only be interesting in the context of responsive metamaterials but also for researchers in other fields. Especially the developed 3D laser microprinting approach for printing liquid-crystal elastomers, the design methods, and the model to predict the behaviour of 3D liquid-crystal elastomer structures might stimulate progress in other fields like for example micro-robotics.

Bibliography

1. M. Kadic, G. W. Milton, M. van Hecke, M. Wegener, 3D metamaterials. *Nat. Rev. Phys.* **1**, 198–210 (2019).

2. C. García-Meca, J. Hurtado, J. Martí, A. Martínez, W. Dickson, A. V. Zayats, Low-Loss Multilayered Metamaterial Exhibiting a Negative Index of Refraction at Visible Wavelengths. *Phys. Rev. Lett.* **106**, 067402 (2011).

3. R. A. Shelby, D. R. Smith, S. Schultz, Experimental Verification of a Negative Index of Refraction. *Science*. **292**, 77–79 (2001).

4. C. M. Soukoulis, S. Linden, M. Wegener, Negative Refractive Index at Optical Wavelengths. *Science*. **315**, 47–49 (2007).

5. S. Zhang, W. Fan, N. C. Panoiu, K. J. Malloy, R. M. Osgood, S. R. J. Brueck, Experimental Demonstration of Near-Infrared Negative-Index Metamaterials. *Phys. Rev. Lett.* **95**, 137404 (2005).

6. K. Bertoldi, V. Vitelli, J. Christensen, M. van Hecke, Flexible mechanical metamaterials. *Nat. Rev. Mater.* **2**, 1–11 (2017).

7. X. Ren, R. Das, P. Tran, T. D. Ngo, Y. M. Xie, Auxetic metamaterials and structures: a review. *Smart Mater. Struct.* **27**, 023001 (2018).

8. L. J. Gibson, M. F. Ashby, G. S. Schajer, C. I. Robertson, The mechanics of two-dimensional cellular materials. *Proc. Math. Phys. Eng. Sci. P ROY SOC A-MATH PHY*. **382**, 25–42 (1982).

9. I. G. Masters, K. E. Evans, Models for the elastic deformation of honeycombs. *Compos. Struct.* **35**, 403–422 (1996).

10. C. W. Smith, J. N. Grima, K. E. Evans, A novel mechanism for generating auxetic behaviour in reticulated foams: missing rib foam model. *Acta Mater*. **48**, 4349–4356 (2000).

11. J. Schwerdtfeger, P. Heinl, R. F. Singer, C. Körner, Auxetic cellular structures through selective electron-beam melting. *Phys. Status Solidi B*. **247**, 269–272 (2010).

12. T. Bückmann, N. Stenger, M. Kadic, J. Kaschke, A. Frölich, T. Kennerknecht, C. Eberl, M. Thiel, M. Wegener, Tailored 3D Mechanical Metamaterials Made by Dip-in Direct-Laser-Writing Optical Lithography. *Adv. Mater*. **24**, 2710–2714 (2012).

13. L. Yang, O. Harrysson, H. West, D. Cormier, Mechanical properties of 3D re-entrant honeycomb auxetic structures realized via additive manufacturing. *Int J Solids Struct.* **69–70**, 475–490 (2015).

14. T. Frenzel, M. Kadic, M. Wegener, Three-dimensional mechanical metamaterials with a twist. *Science*. **358**, 1072–1074 (2017).

15. T. Frenzel, V. Hahn, P. Ziemke, J. L. G. Schneider, Y. Chen, P. Kiefer, P. Gumbsch, M. Wegener, Large characteristic lengths in 3D chiral elastic metamaterials. *Commun. Mater*. **2**, 1–9 (2021).

16. T. Frenzel, J. Köpfler, E. Jung, M. Kadic, M. Wegener, Ultrasound experiments on acoustical activity in chiral mechanical metamaterials. *Nat. Commun*. **10**, 3384 (2019).

17. J. Reinbold, T. Frenzel, A. Münchinger, M. Wegener, The Rise of (Chiral) 3D Mechanical Metamaterials. *Mater*. **12**, 3527 (2019).

18. D. Koller, "Plants in search of sunlight" in *Advances in Botanical Research* [Academic Press, 2000], vol. 33, pp. 35–131.

19. D. R. Sahu, *Multifunctional Ferroelectric Materials* [IntechOpen, 2021].

20. J. Mohd Jani, M. Leary, A. Subic, M. A. Gibson, A review of shape memory alloy research, applications and opportunities. *Mater. Des. (1980-2015)*. **56**, 1078–1113 (2014).

21. H.-W. Chen, J.-H. Lee, B.-Y. Lin, S. Chen, S.-T. Wu, Liquid crystal display and organic light-emitting diode display: present status and future perspectives. *Light Sci. Appl*. **7**, 17168–17168 (2018).

22. T. J. White, D. J. Broer, Programmable and adaptive mechanics with liquid crystal polymer networks and elastomers. *Nat. Mater.* **14**, 1087–1098 (2015).

23. M. O. Saed, A. Gablier, E. M. Terentjev, Exchangeable Liquid Crystalline Elastomers and Their Applications. *Chem. Rev.* **122**, 4927–4945 (2022).

24. M. del Pozo, J. A. H. P. Sol, A. P. H. J. Schenning, M. G. Debije, 4D Printing of Liquid Crystals: What's Right for Me? *Adv. Mater.* **34**, 2104390 (2022).

25. C. A. Spiegel, M. Hippler, A. Münchinger, M. Bastmeyer, C. Barner-Kowollik, M. Wegener, E. Blasco, 4D Printing at the Microscale. *Adv. Funct. Mater.* **30**, 1907615 (2020).

26. S. W. Ula, N. A. Traugutt, R. H. Volpe, R. R. Patel, K. Yu, C. M. Yakacki, Liquid crystal elastomers: an introduction and review of emerging technologies. *Liq. Cryst. Rev*. **6**, 78–107 (2018).

27. C. de las H. Alarcón, S. Pennadam, C. Alexander, Stimuli responsive polymers for biomedical applications. *Chem. Soc. Rev.* **34**, 276–285 (2005).

28. M. A. C. Stuart, W. T. S. Huck, J. Genzer, M. Müller, C. Ober, M. Stamm, G. B. Sukhorukov, I. Szleifer, V. V. Tsukruk, M. Urban, F. Winnik, S. Zauscher, I. Luzinov, S. Minko, Emerging applications of stimuli-responsive polymer materials. *Nature Mater*. **9**, 101–113 (2010).

29. L. Hu, Q. Zhang, X. Li, M. J. Serpe, Stimuli-responsive polymers for sensing and actuation. *Mater. Horiz.* **6**, 1774–1793 (2019).

30. S. M. Montgomery, X. Kuang, C. D. Armstrong, H. J. Qi, Recent advances in additive manufacturing of active mechanical metamaterials. *Curr. Opin. Solid State Mater. Sci.* **24**, 100869 (2020).

31. J. Qi, Z. Chen, P. Jiang, W. Hu, Y. Wang, Z. Zhao, X. Cao, S. Zhang, R. Tao, Y. Li, D. Fang, Recent Progress in Active Mechanical Metamaterials and Construction Principles. *Adv. Sci.* **9**, 2102662 (2022).

32. J. A. Jackson, M. C. Messner, N. A. Dudukovic, W. L. Smith, L. Bekker, B. Moran, A. M. Golobic, A. J. Pascall, E. B. Duoss, K. J. Loh, C. M. Spadaccini, Field responsive mechanical metamaterials. *Sci. Adv*. **4**, eaau6419 (2018).

33. C. Luo, Y. Song, C. Zhao, S. Thirumalai, I. Ladner, M. A. Cullinan, J. B. Hopkins, Design and fabrication of a three-dimensional meso-sized robotic metamaterial with actively controlled properties. *Mater. Horiz*. **7**, 229–235 (2020).

34. Y. Wang, L. Li, D. Hofmann, J. E. Andrade, C. Daraio, Structured fabrics with tunable mechanical properties. *Nature*. **596**, 238–243 (2021).

35. C. Yang, M. Boorugu, A. Dopp, J. Ren, R. Martin, D. Han, W. Choi, H. Lee, 4D printing reconfigurable, deployable and mechanically tunable metamaterials. *Mater. Horiz.* **6**, 1244–1250 (2019).

36. K. Yu, N. X. Fang, G. Huang, Q. Wang, Magnetoactive Acoustic Metamaterials. *Adv. Mater*. **30**, 1706348 (2018).

37. J. N. Grima, R. Caruana-Gauci, M. R. Dudek, K. W. Wojciechowski, R. Gatt, Smart metamaterials with tunable auxetic and other properties. *Smart Mater. Struct.* **22**, 084016 (2013).

38. S. M. Montgomery, S. Wu, X. Kuang, C. D. Armstrong, C. Zemelka, Q. Ze, R. Zhang, R. Zhao, H. J. Qi, Magneto-Mechanical Metamaterials with Widely Tunable Mechanical Properties and Acoustic Bandgaps. *Adv. Funct. Mater*. **31**, 2005319 (2021).

39. J. Mueller, J. A. Lewis, K. Bertoldi, Architected Multimaterial Lattices with Thermally Programmable Mechanical Response. *Adv. Funct. Mater*. **32**, 2105128 (2022).

40. D. Wang, H. Xu, J. Wang, C. Jiang, X. Zhu, Q. Ge, G. Gu, Design of 3D Printed Programmable Horseshoe Lattice Structures Based on a Phase-Evolution Model. *ACS Appl. Mater. Interfaces*. **12**, 22146–22156 (2020).

41. Z. Wang, Z. Wang, Y. Zheng, Q. He, Y. Wang, S. Cai, Three-dimensional printing of functionally graded liquid crystal elastomer. *Sci. Adv*. **6**, eabc0034 (2020).

42. O. R. Bilal, A. Foehr, C. Daraio, Reprogrammable Phononic Metasurfaces. *Adv. Mater*. **29**, 1700628 (2017).

43. A. S. Gliozzi, M. Miniaci, A. Chiappone, A. Bergamini, B. Morin, E. Descrovi, Tunable photo-responsive elastic metamaterials. *Nat. Commun*. **11**, 2576 (2020).

44. Z. Wang, Q. Zhang, K. Zhang, G. Hu, Tunable Digital Metamaterial for Broadband Vibration Isolation at Low Frequency. *Adv. Mater*. **28**, 9857–9861 (2016).

45. Q. Ji, J. Moughames, X. Chen, G. Fang, J. J. Huaroto, V. Laude, J. A. I. Martínez, G. Ulliac, C. Clévy, P. Lutz, K. Rabenorosoa, V. Guelpa, A. Spangenberg, J. Liang, A. Mosset, M. Kadic, 4D Thermomechanical metamaterials for soft microrobotics. *Commun. Mater*. **2**, 1–6 (2021).

46. L. M. Korpas, R. Yin, H. Yasuda, J. R. Raney, Temperature-Responsive Multistable Metamaterials. *ACS Appl. Mater. Interfaces*. **13**, 31163–31170 (2021).

47. L. Chen, Y. Dong, C.-Y. Tang, L. Zhong, W.-C. Law, G. C. P. Tsui, Y. Yang, X. Xie, Development of Direct-Laser-Printable Light-Powered Nanocomposites. *ACS Appl. Mater. Interfaces*. **11**, 19541–19553 (2019).

48. M. del Pozo, C. Delaney, C. W. M. Bastiaansen, D. Diamond, A. P. H. J. Schenning, L. Florea, Direct Laser Writing of Four-Dimensional Structural Color Microactuators Using a Photonic Photoresist. *ACS Nano*. **14**, 9832–9839 (2020).

49. S. Nocentini, F. Riboli, M. Burresi, D. Martella, C. Parmeggiani, D. S. Wiersma, Three-Dimensional Photonic Circuits in Rigid and Soft Polymers Tunable by Light. *ACS Photonics*. **5**, 3222–3230 (2018).

50. E. Sungur, L. Mager, A. Boeglin, M.-H. Li, P. Keller, K. D. Dorkenoo, Temperature tunable optical gratings in nematic elastomer. *Appl. Phys. A*. **98**, 119 (2009).

51. S. Woska, A. Münchinger, D. Beutel, E. Blasco, E. Blasco, J. Hessenauer, O. Karayel, P. Rietz, S. Pfleging, R. Oberle, C. Rockstuhl, C. Rockstuhl, M. Wegener, M. Wegener, H. Kalt, Tunable photonic devices by 3D laser printing of liquid crystal elastomers. *Opt. Mater. Express, OME*. **10**, 2928–2943 (2020).

52. H. Zeng, D. Martella, P. Wasylczyk, G. Cerretti, J.-C. G. Lavocat, C.-H. Ho, C. Parmeggiani, D. S. Wiersma, High-Resolution 3D Direct Laser Writing for Liquid-Crystalline Elastomer Microstructures. *Adv. Mater*. **26**, 2319–2322 (2014).

53. H. Zeng, P. Wasylczyk, C. Parmeggiani, D. Martella, M. Burresi, D. S. Wiersma, Light-Fueled Microscopic Walkers. *Adv. Mater*. **27**, 3883–3887 (2015).

54. Y. Guo, H. Shahsavan, M. Sitti, 3D Microstructures of Liquid Crystal Networks with Programmed Voxelated Director Fields. *Adv. Mater*. **32**, 2002753 (2020).

55. D. Martella, S. Nocentini, D. Nuzhdin, C. Parmeggiani, D. S. Wiersma, Photonic Microhand with Autonomous Action. *Adv. Mater*. **29**, 1704047 (2017).

56. H. Zeng, P. Wasylczyk, G. Cerretti, D. Martella, C. Parmeggiani, D. S. Wiersma, Alignment engineering in liquid crystalline elastomers: Free-form microstructures with multiple functionalities. *Appl. Phys. Lett.* **106**, 111902 (2015).

57. Y. Guo, J. Zhang, W. Hu, M. T. A. Khan, M. Sitti, Shape-programmable liquid crystal elastomer structures with arbitrary three-dimensional director fields and geometries. *Nat. Commun*. **12**, 5936 (2021).

58. C. C. Tartan, P. S. Salter, T. D. Wilkinson, M. J. Booth, S. M. Morris, S. J. Elston, Generation of 3-dimensional polymer structures in liquid crystalline devices using direct laser writing. *RSC Advances*. **7**, 507–511 (2017).

59. J. Sandford O'Neill, P. Salter, Z. Zhao, B. Chen, H. Daginawalla, M. J. Booth, S. J. Elston, S. M. Morris, 3D Switchable Diffractive Optical Elements Fabricated with Two-Photon Polymerization. *Adv. Opt. Mater*. **10**, 2102446 (2022).

60. C. C. Tartan, J. J. Sandford O'Neill, P. S. Salter, J. Aplinc, M. J. Booth, M. Ravnik, S. M. Morris, S. J. Elston, Read on Demand Images in Laser-Written Polymerizable Liquid Crystal Devices. *Adv. Opt. Mater*. **6**, 1800515 (2018).

61. M. Tabrizi, T. H. Ware, M. R. Shankar, Voxelated Molecular Patterning in Three-Dimensional Freeforms. *ACS Appl. Mater. Interfaces*. **11**, 28236–28245 (2019).

62. C. P. Ambulo, J. J. Burroughs, J. M. Boothby, H. Kim, M. R. Shankar, T. H. Ware, Four-dimensional Printing of Liquid Crystal Elastomers. *ACS Appl. Mater. Interfaces*. **9**, 37332–37339 (2017).

63. A. Kotikian, R. L. Truby, J. W. Boley, T. J. White, J. A. Lewis, 3D Printing of Liquid Crystal Elastomeric Actuators with Spatially Programed Nematic Order. *Adv. Mater*. **30**, 1706164 (2018).

64. M. López-Valdeolivas, D. Liu, D. J. Broer, C. Sánchez-Somolinos, 4D Printed Actuators with Soft-Robotic Functions. *Macromol. Rapid Commun*. **39**, 1700710 (2018).

65. D. J. Roach, X. Kuang, C. Yuan, K. Chen, H. J. Qi, Novel ink for ambient condition printing of liquid crystal elastomers for 4D printing. *Smart Mater. Struct.* **27**, 125011 (2018).

66. M. O. Saed, C. P. Ambulo, H. Kim, R. De, V. Raval, K. Searles, D. A. Siddiqui, J. M. O. Cue, M. C. Stefan, M. R. Shankar, T. H. Ware, Molecularly-Engineered, 4D-Printed Liquid Crystal Elastomer Actuators. *Adv. Funct. Mater*. **29**, 1806412 (2019).

67. M. Barnes, S. M. Sajadi, S. Parekh, M. M. Rahman, P. M. Ajayan, R. Verduzco, Reactive 3D Printing of Shape-Programmable Liquid Crystal Elastomer Actuators. *ACS Appl. Mater. Interfaces*. **12**, 28692–28699 (2020).

68. L. Ceamanos, Z. Kahveci, M. López-Valdeolivas, D. Liu, D. J. Broer, C. Sánchez-Somolinos, Four-Dimensional Printed Liquid Crystalline Elastomer Actuators with Fast Photoinduced Mechanical Response toward Light-Driven Robotic Functions. *ACS Appl. Mater. Interfaces*. **12**, 44195–44204 (2020).

69. E. C. Davidson, A. Kotikian, S. Li, J. Aizenberg, J. A. Lewis, 3D Printable and Reconfigurable Liquid Crystal Elastomers with Light-Induced Shape Memory via Dynamic Bond Exchange. *Adv. Mater*. **32**, 1905682 (2020).

70. A. Kotikian, J. M. Morales, A. Lu, J. Mueller, Z. S. Davidson, J. W. Boley, J. A. Lewis, Innervated, Self-Sensing Liquid Crystal Elastomer Actuators with Closed Loop Control. *Adv. Mater*. **33**, 2101814 (2021).

71. X. Lu, C. P. Ambulo, S. Wang, L. K. Rivera-Tarazona, H. Kim, K. Searles, T. H. Ware, 4D-Printing of Photoswitchable Actuators. *Angew. Chem. Int. Ed*. **60**, 5536–5543 (2021).

72. W. Zou, X. Lin, E. M. Terentjev, Amine-Acrylate Liquid Single Crystal Elastomers Reinforced by Hydrogen Bonding. *Adv. Mater*. **33**, 2101955 (2021).

73. X. Peng, S. Wu, X. Sun, L. Yue, S. M. Montgomery, F. Demoly, K. Zhou, R. R. Zhao, H. J. Qi, 4D Printing of Freestanding Liquid Crystal Elastomers via Hybrid Additive Manufacturing. *Adv. Mater*. **34**, 2204890 (2022).

74. P.-G. de Gennes, *The physics of liquid crystals* [Claredon Press, Oxford, 1974].

75. E. B. Priestley, *Introduction to liquid crystals* [Plenum Press, New York and London, 1975].

76. M. Warner, E. M. Terentjev, *Liquid Crystal Elastomers* [Oxford University Press, USA, Revised edition., 2007].

77. B. Van Roie, J. Leys, K. Denolf, C. Glorieux, G. Pitsi, J. Thoen, Weakly first-order character of the nematic-isotropic phase transition in liquid crystals. *Phys. Rev. E*. **72**, 041702 (2005).

78. J. Deschamps, J. P. M. Trusler, G. Jackson, Vapor Pressure and Density of Thermotropic Liquid Crystals: MBBA, 5CB, and Novel Fluorinated Mesogens. *J. Phys. Chem. B*. **112**, 3918–3926 (2008).

79. W. H. de Jeu, Ed., *Liquid Crystal Elastomers: Materials and Applications* [Springer, 2012th edition., 2014].

80. J. D. Bunning, T. E. Faber, P. L. Sherrell, The Frank constants of nematic 5CB at atmospheric pressure. *J. Phys. France*. **42**, 1175–1182 (1981).

81. K. Kittipaisalsilpa, T. Kato, Y. Suzuki, Characterization of fluorinated nematic liquid crystal for high-power electrostatic energy harvester. *J. Phys.: Conf. Ser.* **1052**, 012044 (2018).

82. H. Finkelmann, A. Greve, M. Warner, The elastic anisotropy of nematic elastomers. *Eur. Phys. J. E*. **5**, 281–293 (2001).

83. A. R. Tajbakhsh, E. M. Terentjev, Spontaneous thermal expansion of nematic elastomers. *Eur. Phys. J. E*. **6**, 181–188 (2001).

84. P. Yeh, *Optical Waves in Layered Media* [Wiley-Interscience, Hoboken, NJ, 2nd edition., 2005].

85. L. Novotny, B. Hecht, *Principles of Nano-Optics* [Cambridge University Press, Cambridge, ed. 2, 2012].

86. W. S. Slaughter, *The Linearized Theory of Elasticity* [Birkhäuser, Boston, 2002nd edition., 2001].

87. V. A. Lubarda, Constitutive theories based on the multiplicative decomposition of deformation gradient: Thermoelasticity, elastoplasticity, and biomechanics. *Appl. Mech. Rev*. **57**, 95–108 (2004).

88. A. Münchinger, V. Hahn, D. Beutel, S. Woska, J. Monti, C. Rockstuhl, E. Blasco, M. Wegener, Multi-Photon 4D Printing of Complex Liquid Crystalline Microstructures by In Situ Alignment Using Electric Fields. *Adv. Mater. Technol.* **7**, 2100944 (2022).

89. I. Dierking, Dielectric breakdown in liquid crystals. *J. Phys. D: Appl. Phys.* **34**, 806–813 (2001).

90. V. Hahn, P. Kiefer, T. Frenzel, J. Qu, E. Blasco, C. Barner-Kowollik, M. Wegener, Rapid Assembly of Small Materials Building Blocks (Voxels) into Large Functional 3D Metamaterials. *Adv. Funct. Mater*. **30**, 1907795 (2020).

91. H. Zeng, D. Martella, P. Wasylczyk, G. Cerretti, J.-C. G. Lavocat, C.-H. Ho, C. Parmeggiani, D. S. Wiersma, High-Resolution 3D Direct Laser Writing for Liquid-Crystalline Elastomer Microstructures. *Adv. Mater*. **26**, 2319–2322 (2014).

92. J. M. McCracken, B. R. Donovan, K. M. Lynch, T. J. White, Molecular Engineering of Mesogenic Constituents Within Liquid Crystalline Elastomers to Sharpen Thermotropic Actuation. *Adv. Funct. Mater.* **31**, 2100564 (2021).

93. A. Münchinger, L.-Y. Hsu, F. Fürniß, E. Blasco, M. Wegener, 3D optomechanical metamaterials. *Mater. Today* (2022), doi:10.1016/j.mattod.2022.08.020.

94. T. Frenzel, C. Findeisen, M. Kadic, P. Gumbsch, M. Wegener, Tailored Buckling Microlattices as Reusable Light-Weight Shock Absorbers. *Adv. Mater*. **28**, 5865–5870 (2016).

95. T. Frenzel, J. Köpfler, A. Naber, M. Wegener, Atomic scale displacements detected by optical image cross-correlation analysis and 3D printed marker arrays. *Sci. Rep.* **11**, 2304 (2021).

96. M. P. da Cunha, E. A. J. van Thoor, M. G. Debije, D. J. Broer, A. P. H. J. Schenning, Unravelling the photothermal and photomechanical contributions to actuation of azobenzene-doped liquid crystal polymers in air and water. *J. Mater. Chem. C*. **7**, 13502–13509 (2019).

97. L.-Y. Hsu, P. Mainik, A. Münchinger, S. Lindenthal, T. Spratte, J. Zaumseil, C. Selhuber-Unkel, M. Wegener, E. Blasco, A Facile Approach for 4D Microprinting of Multi-photoresponsive Actuators. *Adv. Mater. Technol.,* 2200801 (2022).

98. Y. Cang, J. Liu, M. Ryu, B. Graczykowski, J. Morikawa, S. Yang, G. Fytas, On the origin of elasticity and heat conduction anisotropy of liquid crystal elastomers at gigahertz frequencies. *Nat. Commun*. **13**, 5248 (2022).

99. W. Ren, P. J. McMullan, A. C. Griffin, Poisson's Ratio of Monodomain Liquid Crystalline Elastomers. *Macromol. Chem. Phys*. **209**, 1896–1899 (2008).

100. D. Martella, D. Antonioli, S. Nocentini, D. S. Wiersma, G. Galli, M. Laus, C. Parmeggiani, Light activated non-reciprocal motion in liquid crystalline networks by designed microactuator architecture. *RSC Adv.* **7**, 19940–19947 (2017).

101. T. L. Nguyen, M. A. Saleh, Thermal degradation of azobenzene dyes. *Results Chem*. **2**, 100085 (2020).

102. R. K. Shaha, A. H. Torbati, C. P. Frick, Body-temperature shape-shifting liquid crystal elastomers. *J. Appl. Polym. Sci*. **138**, 50136 (2021).

Acknowledgments

At this point, I thank all people that contributed to this work.

First of all, I want to thank Prof. Dr. Martin Wegener who gave me the opportunity to work on this versatile project. I appreciate the trust he put in me by giving me the large freedom to develop my own ideas. However, I am also thankful for the guidance he offered whenever he saw that I was heading towards a wrong direction.

Similarly, I thank Jun.-Prof. Dr. Eva Blasco that she supervised the chemistry aspects of this work. We had many discussions about possible liquid-crystal resins and other responsive systems. I highly value her advice on which routes are promising to go and which are rather not. I am grateful that she agreed to co-referee this thesis.

I am highly indebted to Dr. Vincent Hahn. Without the printing setup he built, this work would have stopped at the point where I realized that the polarization of the printing laser has to be manipulated during the printing. He invested several days and weeks to introduce me to his setup and he offered immediate help, whenever I was lost at the setup. Also, I appreciated my visits in his lab and the inspiring discussions there.

I thank Dominik Beutel and Prof. Dr. Carsten Rockstuhl who performed the calculation of the intensity distribution of a focused laser within a birefringent photoresin for different polarisations. At this time, this was an important prerequisite to base further experiments on.

I highly value the constant exchange with Dr. Simon Woska and Li-Yun Hsu about our experiences on 3D laser microprinting of liquid-crystal elastomers. I am also grateful for the recipe that Li-Yun Hsu provided me to dye my liquid-crystal elastomer structures.

I want to thank Dr. Joël Monti for synthesizing a chemical compound for me. It is a great pity, that it did not improve my photoresins.

I wish to thank Franziska Fürniß for setting up the first version of the chiral unit cell in COMSOL during her master thesis.

Without the opportunity to use the cleanroom and the facilities of the nanostructure service laboratory, it would have been impossible to fabricate the electrodes. I want to thank Lucas Radtke for his help in fabrication of the photomasks for the structuring of the electrode and his advices during the fabrication of the electrode. Equally, I want to

thank Aina Quintilla and Patrice Brenner for teaching me how to use the electron beam deposition system and their help, whenever there were issues with this machine.

During my time at the institute of applied physics I was always fascinated of all the masterpieces that Frank Landhäußer and his team realize. I am grateful to Frank Landhäußer for his advice in the design of the electrode mount and that he went through all the iterations until the mount finally achieved the necessary precision for positioning of the electrode.

I want to thank Johann Westhauser for the construction of the housing for the voltage dividers and that he managed all the paperwork necessary to order new equipment.

Thanks also goes to Michael Hippe for his advice in design and assembly of the electronics to drive the electrode. Also, I am impressed of Werner Gilde for repairing all these presumed dead devices in the lab. My thank also goes to Helmut Lay who always helped whenever there was an IT issue.

Whenever I was facing paperwork for administrative tasks, I was relieved that Claudia Alaya, Petra Bauer, Monika Brenkman and Ursula Mösle were there to support me.

I am thankful for the funding I received from the cluster of excellence “3D Matter Made to Order”.

The burden of proof reading this thesis was carried by Vincent Hahn, Sebastian Kalt, Michael Groß, Pascal Kiefer and Jonathan Schneider. Thank you very much!

My sincere thank goes to all the group members that became my friends. They were an important reason for me to stay in the group.

Finally, great thank goes to my parents, who always emphasize the value of education and raised me to a resilient enough person to finish a project that bears the first fruit only after years of work. I want to thank my wife for her love and the great support. The time with her and my son is the best in my life.